

# COSMOGLOBE I. Improved Wilkinson Microwave Anisotropy Probe frequency maps through Bayesian end-to-end analysis

D. J. Watts<sup>1\*</sup>, A. Basyrav<sup>1</sup>, M. Galloway<sup>1</sup>, D. Herman<sup>1</sup>, H. T. Ihle<sup>1</sup>, S. Paradiso<sup>2</sup>, F. Rahman<sup>3</sup>, H. Thommesen<sup>1</sup>, M. Bersanelli<sup>4</sup>, L. A. Bianchi<sup>4</sup>, M. Brilenkov<sup>1</sup>, L. P. L. Colombo<sup>4</sup>, H. K. Eriksen<sup>1</sup>, J. R. Eskilt<sup>1,5</sup>, K. S. F. Fornazier<sup>6</sup>, C. Franceschet<sup>4</sup>, U. Fuskeland<sup>1</sup>, E. Gjerløw<sup>1</sup>, B. Hensley<sup>7</sup>, L. T. Hergt<sup>8</sup>, G. A. Hoerning<sup>6</sup>, K. Lee<sup>1</sup>, J. G. S. Lunde<sup>1</sup>, A. Marins<sup>6,9</sup>, S. K. Nerval<sup>10,11</sup>, S. K. Patel<sup>12</sup>, M. Regnier<sup>13</sup>, M. San<sup>1</sup>, S. Sanyal<sup>12</sup>, N.-O. Stutzer<sup>1</sup>, A. Verma<sup>12</sup>, I. K. Wehus<sup>1</sup>, and Y. Zhou<sup>14</sup>

<sup>1</sup> Institute of Theoretical Astrophysics, University of Oslo, Blindern, Oslo, Norway

<sup>2</sup> Waterloo Centre for Astrophysics, University of Waterloo, Waterloo, ON N2L 3G1, Canada

<sup>3</sup> Indian Institute of Astrophysics, Koramangala II Block, Bangalore, 560034, India

<sup>4</sup> Dipartimento di Fisica, Università degli Studi di Milano, Via Celoria, 16, Milano, Italy

<sup>5</sup> Imperial Centre for Inference and Cosmology, Department of Physics, Imperial College London, Blackett Laboratory, Prince Consort Road, London SW7 2AZ, United Kingdom

<sup>6</sup> Instituto de Física, Universidade de São Paulo - C.P. 66318, CEP: 05315-970, São Paulo, Brazil

<sup>7</sup> Department of Astrophysical Sciences, Princeton University, 4 Ivy Lane, Princeton, NJ 08540

<sup>8</sup> Department of Physics and Astronomy, University of British Columbia, 6224 Agricultural Road, Vancouver BC, V6T1Z1, Canada

<sup>9</sup> Department of Astronomy, University of Science and Technology of China, Hefei, China

<sup>10</sup> David A. Dunlap Department of Astronomy & Astrophysics, University of Toronto, 50 St. George Street, Toronto, ON M5S 3H4, Canada

<sup>11</sup> Dunlap Institute for Astronomy & Astrophysics, University of Toronto, 50 St. George Street, Toronto, ON M5S 3H4, Canada

<sup>12</sup> Department of Physics, Indian Institute of Technology (BHU), Varanasi - 221005, India

<sup>13</sup> Laboratoire Astroparticule et Cosmologie (APC), Université Paris-Cité, Paris, France

<sup>14</sup> Department of Physics, UC Berkeley

March 6, 2023

## ABSTRACT

We present the first joint analysis of *WMAP* and *Planck* LFI time-ordered data, processed within the Bayesian end-to-end COSMOGLOBE framework. This framework builds directly on a similar analysis of the LFI measurements by the BEYONDPLANCK collaboration, and approaches the CMB analysis challenge through Gibbs sampling of a global posterior distribution. The computational cost of producing one complete *WMAP*+LFI Gibbs sample is 581 CPU-hr, including calibration, mapmaking, and component separation, of which 389 CPU-hr is spent on *WMAP* low-level processing; this demonstrates that end-to-end Bayesian analysis of the *WMAP* data is computationally feasible. We find that our *WMAP* posterior mean temperature sky maps are largely consistent with the official maps, and the resulting CMB power spectrum is in excellent agreement with previous results. The most notable difference is a slightly lower CMB quadrupole amplitude of  $\sigma_2 = 120 \pm 65 \mu\text{K}^2$ , as compared to  $\sigma_2 = 229 \pm 97 \mu\text{K}^2$  in the BEYONDPLANCK analysis. In contrast, our *WMAP* polarization maps differ more notably from the official results, and in general they exhibit lower large-scale residuals, most likely to a better constrained gain and transmission imbalance model; it is particularly noteworthy that our *W*-band sky maps appear statistically consistent with the *V*-band maps. For the first time, *WMAP*-minus-LFI frequency map differences appear visually consistent with instrumental noise over most of the sky. Still, we identify three specific issues that require additional work, namely 1) low-level noise modeling, 2) quadrupole residuals in the *V*- and *W*-band temperature maps at the  $2 \mu\text{K}$  level; and 3) a strong degeneracy between the absolute *K*-band calibration and the dipole of the anomalous microwave emission component. Nevertheless, we believe that the reprocessed *WMAP* maps presented here are significantly cleaner in terms of systematic uncertainties than the official *WMAP* maps. Both sky maps and the associated code are made publicly available through the COSMOGLOBE web page.

**Key words.** ISM: general – Cosmology: observations, polarization, cosmic microwave background, diffuse radiation – Galaxy: general

## Contents

<b>1</b> Introduction	<b>2</b>	2.4 Sky model . . . . .	5
<b>2</b> End-to-end Bayesian CMB analysis	<b>3</b>	2.5 Priors . . . . .	5
2.1 LFI and BEYONDPLANCK . . . . .	3	2.6 Posterior distribution and Gibbs sampling . . . . .	6
2.2 Official <i>WMAP</i> instrument characterization and analysis pipeline . . . . .	3	2.7 Sampling algorithms . . . . .	7
2.3 Instrument model . . . . .	4	2.7.1 Review of sampling algorithms . . . . .	7
		2.7.2 Differential mapmaking . . . . .	8
		2.7.3 Transmission imbalance estimation . . . . .	8
		2.7.4 Baseline sampling . . . . .	8
<b>3</b> Data and data processing			9
	3.1 Publicly available <i>WMAP</i> products . . . . .		9

\* Corresponding author: D. J. Watts; [duncanwa@astro.uio.no](mailto:duncanwa@astro.uio.no)

3.2	TOD pre-processing and data selection . . . . .	9
3.3	Computational resources . . . . .	9
<b>4</b>	<b>Instrumental parameters</b>	<b>10</b>
4.1	Trace plots and correlations . . . . .	10
4.2	Gain and baselines . . . . .	10
4.3	Transmission imbalance . . . . .	12
4.4	Instrumental noise and goodness-of-fit . . . . .	13
<b>5</b>	<b>Frequency maps</b>	<b>13</b>
5.1	Map summary statistics . . . . .	14
5.2	Comparison with 9-year <i>WMAP</i> maps . . . . .	21
5.3	Consistency within <i>WMAP</i> channels . . . . .	25
5.4	Consistency between <i>WMAP</i> and LFI . . . . .	26
<b>6</b>	<b>Preliminary astrophysical results</b>	<b>26</b>
6.1	CMB results . . . . .	26
6.1.1	Solar dipole . . . . .	26
6.1.2	Low- $\ell$ anomalies . . . . .	26
6.1.3	Angular temperature power spectrum . . . . .	26
6.2	Galactic foregrounds . . . . .	26
6.3	<i>WMAP</i> -versus-LFI signal-to-noise ratio comparison . . . . .	30
<b>7</b>	<b>Systematic error corrections and uncertainties</b>	<b>30</b>
7.1	Sky map corrections . . . . .	30
7.2	Power spectrum residuals . . . . .	30
<b>8</b>	<b>Outstanding issues</b>	<b>30</b>
8.1	Noise modeling . . . . .	30
8.2	<i>V</i> -band quadrupole residual . . . . .	30
8.3	Degeneracy between <i>K</i> -band calibration and AME dipole . . . . .	30
8.4	Other minor effects . . . . .	30
8.4.1	Time-variable bandpass modeling . . . . .	30
8.4.2	Polarized sidelobe modeling . . . . .	30
<b>9</b>	<b>Conclusions</b>	<b>30</b>
<b>A</b>	<b>Survey of instrumental parameters</b>	<b>38</b>
A.1	Gain, baselines, noise and $\chi^2$ . . . . .	38
A.2	Transmission imbalance . . . . .	38
<b>B</b>	<b><i>WMAP</i> frequency map survey</b>	<b>38</b>
<b>C</b>	<b>Comparison with BEYONDPLANCK LFI results</b>	<b>38</b>

## 1. Introduction

The discovery of the cosmic microwave background (CMB) by Penzias & Wilson (1965) marked a paradigm shift in the field of cosmology, providing direct evidence that the Universe was once much hotter than it is today, effectively ruling out the steady-state theory of the universe (Dicke et al. 1965). This discovery spurred a series of ground-breaking cosmological experiments, including the Nobel Prize-winning measurements by COBE-FIRAS that confirmed the blackbody nature of the CMB (Mather et al. 1994) and COBE-DMR that measured temperature variations from the primordial gravitational field (Smoot et al. 1992).

The NASA-funded *Wilkinson Microwave Anisotropy Probe* (*WMAP*; Bennett et al. 2003a) mission was launched a decade after COBE-DMR, and mapped the microwave sky with 45 times higher sensitivity and 33 times higher angular resolution, and thereby revolutionizing our understanding of early universe

physics (Bennett et al. 2003a). As quantified by Bennett et al. (2013), the permissible parameter space volume for a standard  $\Lambda$ CDM model was decreased by a factor of 68,000 by *WMAP*, and the best pre-*WMAP* determination of the age of the universe was  $t_0 < 14$  Gyr from Boomerang (Lange et al. 2001), with best-fit values of 9–11 Gyr; the latter values in apparent contradiction with direct measurements of the oldest globular clusters (Hu et al. 2001).

The ESA-led *Planck* satellite (Planck Collaboration I 2020) was developed concurrently with *WMAP*, and their operation lifetimes briefly overlapped, with *Planck* observing from 2009–2013 and *WMAP* from 2001–2011. *Planck*'s stated goal was to fully characterize the primary CMB temperature fluctuations from recombination, as well as to characterize the polarized microwave sky on large angular scales. Overall, *Planck*'s raw CMB sensitivity was an order of magnitude higher than *WMAP*'s, and its angular resolution three times higher. Today, *Planck* represents the state-of-the-art in terms of full-sky microwave sky measurements.

*Planck* comprised two independent experiments, namely the Low Frequency Instrument (LFI; Planck Collaboration II 2020) and High Frequency Instrument (HFI; Planck Collaboration III 2020), respectively. The LFI detectors were based on HEMT (high electron mobility transistor) amplifiers, spanning three frequency channels between 30 and 70 GHz, while the HFI detectors were based on TES (transition edge sensitive) bolometers, and spanned six frequency channels between 100 and 857 GHz. For comparison, *WMAP* was also HEMT-based, with comparable sensitivity to LFI alone, and spanned five frequencies between 23 and 94 GHz. At the same time, the two experiments implemented very different scanning strategies, and as a result they are highly complementary and synergistic; together they provide a clearer view of the low-frequency microwave sky than either can alone.

Towards the end of the *Planck* analysis phase it became clear that the interplay between instrument calibration and astrophysical component separation represents a main limiting factor in terms of systematic effects for high signal-to-noise measurements (Planck Collaboration II 2020). Specifically, in order to calibrate the instrument to sufficient precision, it is necessary to know the true sky to a comparably high precision – but to know the sky, it is also necessary to know the instrumental calibration. The data analysis is thus fundamentally circular and global in nature. The final official *Planck* LFI analysis performed four complete iterations between calibration and component separation (Planck Collaboration II 2020), aiming to probe this degeneracy. However, it was clearly recognized that this was not sufficient to reach full convergence, and this sub-optimality led to the BEYONDPLANCK project (BeyondPlanck 2022), which aimed to perform thousands of complete analysis cycles, as opposed to just a handful. This framework was implemented using the Commander3 (Galloway et al. 2022) code, a CMB Gibbs sampler that performs integrated high-level and low-level parameter estimation in a single integrated framework. This analysis demonstrated the feasibility of a full end-to-end Gibbs sampling analysis in the CMB framework, while providing the highest-quality LFI maps to date.

Rather than simply probing the degeneracy between instrument calibration and component separation, a better solution is to actually break it. The optimal approach to do so is by jointly analyzing complementary datasets, each of which provide key information regarding the full system. This insight led

to the COSMOGLOBE<sup>1</sup> initiative, which is an Open Source and community-wide effort that aims to derive a single joint model of the radio, microwave, and sub-millimeter sky by combining all available state-of-the-art experiments. An obvious first extension of the LFI-oriented BEYONDPLANCK project is to analyze the *WMAP* measurements in the same framework. Indeed, already as part of the BEYONDPLANCK suite of papers, Watts et al. (2022) integrated *WMAP* *Q*-band time-ordered data (TOD) into the Commander3 framework, calibrated off of the BEYONDPLANCK sky model.

In this paper, we present the first end-to-end Bayesian analysis of the full *WMAP* TOD, processed within the COSMOGLOBE framework. As such, this paper also presents the first ever joint analysis of two major CMB experiments (LFI and *WMAP*) at the lowest possible level, and it therefore constitutes a major milestone of the COSMOGLOBE project. In the future, many more datasets will be added, gradually providing stronger and stronger constraints on the true astrophysical sky. Each new experiment will then also in turn improve the instrumental calibration of all previous experiments.

The rest of this paper is organized as follows. In Sect. 2, we provide a brief review of the Bayesian end-to-end statistical framework used in this work, before describing the underlying data and computational expenses in Sect. 3. The main results, as defined by the global posterior distribution, are described in Sects. 4–6, summarizing instrumental parameters, frequency sky maps, and astrophysical results, respectively. In Sect. 7 we quantify the systematic error budget for this analysis, while we address a few minor unresolved issues in Sect. 8 that should be addressed in future work. We conclude in Sect. 9, and lay a path forward for the COSMOGLOBE project.

## 2. End-to-end Bayesian CMB analysis

The general computational analysis framework used in this work has been described in detail by BeyondPlanck (2022) and Watts et al. (2022) and references therein. In this section, we give a brief summary of the main points, and emphasize in particular the differences with respect to earlier work.

### 2.1. LFI and BEYONDPLANCK

The BEYONDPLANCK project (BeyondPlanck 2022) was the first true application of end-to-end Gibbs sampling in the framework of CMB data analysis. The *Planck* LFI data had been gradually improved through each *Planck* data release, specifically PR1 (Planck Collaboration II 2016), PR2 (Planck Collaboration II 2016), PR3 (Planck Collaboration II 2020), and PR4 (Planck Collaboration II 2016). Even after PR4, however, the final LFI maps still failed significant polarization null tests (in particular for the 44 GHz frequency channel), in particular due to contained poorly measured realtive gain uncertainty modes. Indeed, already the PR3 analysis noted a strong degeneracy between the LFI gain solution and the astrophysical foreground model, and to break these the *Planck* LFI Data Processing Center (DPC) implemented an iterative scheme in which the various low-level processing and component separation operations were performed sequentially and repeatedly. However, because these iterations were performed manually with significant amounts of human interactions, these scheme was very slow, and only four full cycles were completed before the *Planck* collaboration ended. A main motivation for the BEYONDPLANCK project was to automate this

process, and perform thousands of such iterations, rather than just four.

This work was highly successful, and the BEYONDPLANCK collaboration was able to generate the first LFI maps with true joint estimation of sky components and underlying instrumental parameters through a statistical process called Gibbs sampling (BeyondPlanck 2022; Galloway et al. 2022; Basyrov et al. 2022). The code used for this process was called Commander3 (Galloway et al. 2022). The resulting Gibbs chains allowed for data-driven estimates of the instrumental properties to be determined by exploring the degeneracies between the low-level instrumental parameters themselves and our knowledge of the sky (Andersen et al. 2022; Svalheim et al. 2022), and in doing so resulted in new state-of-the-art and low-systematics LFI maps.

### 2.2. Official *WMAP* instrument characterization and analysis pipeline

The main goal of the current paper is to perform a similar analysis with the *WMAP* time-ordered data, and thereby solve some of the long-standing unresolved issues with the official maps, in particular related to poorly constrained large-scale polarization modes. Before presenting our algorithm, however, it is useful for reference purposes to briefly review the official *WMAP* instrument model and analysis pipeline, which improved gradually over a total of five data releases, often referred to as the 1-, 3-, 5-, 7, and 9-year data releases, respectively. Unless otherwise noted, we will in the following refer to the final 9-year results in the following.

The *WMAP* satellite carried forty differential polarization-sensitive radiometers grouped as differencing assemblies (DAs), where one pair was sensitive to the difference in signal at one polarization orientation and the other pair sensitive to the orthogonal polarization. In total, there were ten DAs, which were distributed as one *K*-band (23 GHz), one *Ka*-band (33 GHz), two *Q*-band (41 GHz), two *V*-band (61 GHz), and four *W*-band (94 GHz) DAs.

The *WMAP* bandpasses were measured pre-launch on ground, sweeping a signal source through 201 frequencies and recording the output (Jarosik et al. 2003b). The bandpass responses have not been updated since the initial data release. However, as noted in Bennett et al. (2013), there has been an observed drift in the center frequency of *K*, *Ka*, *Q*, and *V*-band corresponding to a  $\sim 0.1\%$  decrease over time. In practice, this did not affect the *WMAP* data processing because each year was mapped separately and co-added afterwards. An effective frequency calculator was delivered in the DR5 release as part of the IDL library to mitigate this effect during astrophysical analyses.<sup>2</sup>

The beams were characterized in the form of maps, with separate products for the near-field and far-field. The main beam and near sidelobes were characterized using a combination of physical optics codes and observations of Jupiter for each horn separately. The maps of Jupiter were then combined with the best-fit physical optics codes to create a map of the beam response (Hill et al. 2009; Weiland et al. 2011; Bennett et al. 2013). Far sidelobes were estimated using a combination of laboratory measurements and Moon data taken during the mission (Barnes et al. 2003), as well as a physical optics model described by Hinshaw et al. (2009). To remove the far sidelobe in the TOD, an estimate was calculated by convolving the intensity map and the orbital dipole signal with the measured sidelobe sig-

<sup>1</sup> <https://cosmoglobe.uio.no>

<sup>2</sup> [https://lambda.gsfc.nasa.gov/product/wmap/dr5/m\\_sw.html](https://lambda.gsfc.nasa.gov/product/wmap/dr5/m_sw.html)

nal (Jarosik et al. 2007). Although the sidelobe pickup was modeled by Barnes et al. (2003), it was determined that the results were small enough to be neglected and have not been explicitly reported in any of the subsequent *WMAP* data releases.

The *WMAP* pointing solution was determined using the bore-sight vectors of individual feedhorns in spacecraft coordinates, in combination with on-board star trackers. Thermal flexure of the tracking structure introduced small pointing errors, as discussed by Jarosik et al. (2007). Using the temperature variation measured by housekeeping data, the quaternion pointing solution was corrected using a linear model that depends on arcsecond per kelvin. The residual pointing errors were computed using observations of Jupiter and Saturn, and the reported upper limit was given by 10'' (Bennett et al. 2013; Greason et al. 2012).

The *WMAP* data were calibrated by jointly estimating the time-dependent gains and baselines, as described by Hinshaw et al. (2007), Hinshaw et al. (2009), and Jarosik et al. (2011). The TOD were initially modeled as having constant gain and baseline for a 1–24 hour period, with parameters that were fit to the orbital dipole assuming  $T_0$  from Mather et al. (1999) and a map made from a previous iteration of the mapmaking procedure. Once the gain and baseline solution had converged, the data were fit to a parametric form of the radiometer response as a function of housekeeping data, given in Appendix A of Greason et al. (2012).

As noted above, the *WMAP* radiometers were inherently differential in nature, and measured the signal differences in two directions through two horns, referred to as the A- and B-sides. The responsivity of the two sides was not identical, and this effective gain imbalance is referred to as “transmission imbalance”. The amplitude of this effect is parameterized by  $x_{\text{im}} = (\alpha_A - \alpha_B)/2$ , where  $\alpha_A$  and  $\alpha_B$  are the transmission coefficients of each side, and this parameter is zero in the case of an ideal differential radiometer. In practice, an unpolarized sky map generates a timestream

$$\begin{aligned} d_t^{\text{imbal}} &\propto (1 + x_{\text{im}})T_{p_A} - (1 - x_{\text{im}})T_{p_B} \\ &= (T_{p_A} - T_{p_B}) + x_{\text{im}}(T_{p_A} + T_{p_B}). \end{aligned} \quad (1)$$

This effect is taken into account during mapmaking. However, inaccuracies in the determination of  $x_{\text{im}}$  will yield a spurious polarization component, and create artificial imbalance modes due to coupling with the sky signal, in particular with the bright Solar CMB dipole (Jarosik et al. 2007). The *WMAP* transmission imbalance factors were fit to the Solar dipole in TOD space, accounting for both common and differential modes (Jarosik et al. 2003a, 2007).

Data were flagged and masked before the final mapmaking step. In particular, station-keeping maneuvers, solar flares, and unscheduled events caused certain data to be unusable – the full catalog of these events is listed in Table 1.8 of Greason et al. (2012). In addition, data were masked depending on the channel frequency and the planet itself, with the full list of exclusion radii enumerated in Table 4 of Bennett et al. (2013).

To create the sky maps  $\mathbf{m}$ , the calibrated data were put into the asymmetric mapmaking equation,

$$\mathbf{P}_{\text{am}}^T \mathbf{N}^{-1} \mathbf{P} \mathbf{m} = \mathbf{P}_{\text{am}}^T \mathbf{N}^{-1} \mathbf{d}, \quad (3)$$

where  $\mathbf{P}$  is implicitly defined for detectors  $\mathbf{d}_1$  and  $\mathbf{d}_2$  sensitive to different polarization orientations,

$$\begin{aligned} \mathbf{d}_1 &= \mathbf{P}_1 \mathbf{m} \\ &= (1 + x_{\text{im}})[T_A + Q_A \cos 2\gamma_A + U_A \sin 2\gamma_A + S_A] \\ &+ (1 - x_{\text{im}})[-T_B - Q_B \cos 2\gamma_B - U_B \sin 2\gamma_B - S_B], \end{aligned} \quad (4)$$

and

$$\mathbf{d}_2 = \mathbf{P}_2 \mathbf{m} \quad (5)$$

$$\begin{aligned} &= (1 + x_{\text{im}})[T_A - Q_A \cos 2\gamma_A - U_A \sin 2\gamma_A - S_A] \\ &+ (1 - x_{\text{im}})[-T_B + Q_B \cos 2\gamma_B + U_B \sin 2\gamma_B + S_B]. \end{aligned} \quad (6)$$

In this formalism,  $S$  acts as an extra Stokes parameter that absorbs the effects of differing bandpass responses between radiometers  $\mathbf{d}_1$  and  $\mathbf{d}_2$  (Jarosik et al. 2007). The asymmetric mapmaking matrix,  $\mathbf{P}_{\text{am}}$ , was used because, as noted in Jarosik et al. (2011), large signals observed in one beam could leak into the solution for the pixel observed by the other beam, leading to incorrect signals in the final map. The asymmetric mapmaking solution essentially works by only updating the matrix multiplication for beam A when beam A is in a high emission region and beam B is not, and vice versa. Bennett et al. (2013) also identified that these effects are pronounced when there is a steep gradient in the emission across the  $N_{\text{side}} = 512$  pixels within an  $N_{\text{side}} = 16$  superpixel, leading to excesses 140° away from the Galactic center.

An accurate noise model was necessary to perform the maximum likelihood mapmaking, as it required the evaluation of the dense time-space inverse noise covariance matrix  $\mathbf{N}^{-1}$ . The time-space autocorrelation function was estimated for each year of data, which is then Fourier transformed, inverted, and Fourier transformed again to create an effective inverse noise operator  $\mathbf{N}_{tt'}^{-1}$ . Finally, to create the sky maps themselves, the data are treated one year at a time, and the iterative Bi-conjugate Gradient Stabilized Method (BiCG-STAB van der Vorst 1992; Barrett et al. 1994) is applied to the maps.

### 2.3. Instrument model

As opposed to the *WMAP* pipeline, the COSMOGLOBE uses a generative model for every aspect of the data, including the sky and instrumental effects at once. In the COSMOGLOBE paradigm, it is simplest to characterize the data’s goodness-of-fit to a model,

$$\mathbf{d} = \mathbf{GP}[\mathbf{B}^{\text{symm}} \mathbf{Ma} + \mathbf{B}^{4\pi}(\mathbf{s}^{\text{orb}} + \mathbf{s}^{\text{fsl}})] + \mathbf{s}^{\text{inst}} + \mathbf{n}^{\text{corr}} + \mathbf{n}^{\text{w}}, \quad (7)$$

where  $\mathbf{G}$  is the time-dependent gain in the form of the matrix  $\text{diag}(g_t)$ ,  $\mathbf{P}$  is the  $n_p \times n_t$  pointing matrix, where  $n_p$  is the number of pixels and  $n_t$  the number of TOD datapoints,  $\mathbf{B}^{\text{symm}}$  and  $\mathbf{B}^{4\pi}$  are the symmetrized and full asymmetric beam, respectively,  $\mathbf{M}$  is the mixing matrix between a given component  $c$  with spectral energy distribution  $f_c(v/v_{0,c})$  and a detector  $j$  with bandpass  $\tau_j(v)$ , given by

$$\mathbf{M}_{cj} = \int dv \tau_j(v) f_c(v/v_{c,0}). \quad (8)$$

The maps  $\mathbf{a}$  are the component amplitudes,  $\mathbf{s}^{\text{orb}}$  is the orbital dipole induced by the motion of the telescope with respect to the Sun, and  $\mathbf{s}^{\text{fsl}}$  is the time-dependent far sidelobe signal. In the Commander3 (Galloway et al. 2022) implementation,  $\mathbf{n}^{\text{corr}}$  is a realization of the correlated noise component whose power spectrum is parametrized by  $P(f | \xi_n)$ , where  $\xi_n$  generally includes  $f_{\text{knee}}$ , a slope  $\alpha$ , and an amplitude fixed by the white noise  $\sigma_0$ . Similarly, each experiment has particular signals that are specific to the instrument in question, e.g., the 1 Hz spike in *Planck* LFI or the large baseline in *WMAP*, which can be modeled by  $\mathbf{s}^{\text{inst}}$ .

The bandpass mismatch is explicitly modeled in Commander3. Using the calibrated sky model, the expected

calibrated sky signal is given by

$$m_{p,j} = \mathbf{B}_{p,p'} \sum_c \mathbf{M}_{c,j} a_{p'}^c + n_{j,p}^w. \quad (9)$$

Since  $\mathbf{M}_{c,j}$  encodes the bandpass response of every detector  $j$  to every sky component  $c$ , the maps  $\mathbf{m}_j$  will each be slightly different depending on their bandpass  $\tau_j$ . More importantly, differences in signal between different detectors can be attributed to a spurious polarization signal, giving spurious polarized maps. Therefore, before averaging different detectors together, Commander3 estimates the average over all detectors in a given frequency channel  $\mathbf{m} \equiv \langle \mathbf{m}_j \rangle$ , and subtracts it directly in the timestream;

$$\delta s_{t,j}^{\text{leak}} = \mathbf{P}_{t,p}^j \mathbf{B}_{p,p'}^j (\mathbf{m}_{j,p'} - \mathbf{m}_{p'}). \quad (10)$$

This leakage term uses the expected bandpass response to remove the expected component that deviates from the mean in the timestream, directly reducing polarization contamination.

The most unique feature of the *WMAP* data is that it includes differential pointing. *WMAP* has two primary mirrors approximately reflected along the vertical satellite axis, and are tilted approximately  $19.5^\circ$  downwards – in total, when horn A is pointed at pixel  $p_A$ , horn B is pointed at a pixel  $p_B$  that is approximately  $141^\circ$  away (Page et al. 2003). The incoming radiation is differenced in the electronics before being deposited on the detectors, essentially recording radiation proportional to  $\mathbf{m}_A - \mathbf{m}_B$  and  $\mathbf{m}_B - \mathbf{m}_A$  (Jarosik et al. 2003b). Each pair of radiometers has a partner pair of radiometers that observes the same pixels with sensitivity to the orthogonal polarization direction. Taking these effects all into account, the total data model for a single radiometer is given by

$$d_t = g_t \mathbf{P}_{t,p} s_p + s_t^{\text{inst}} + n_t \quad (11)$$

$$\begin{aligned} &= g_t [\alpha_A (T_{p_A(t)} + Q_{p_A(t)} \cos 2\gamma_A(t) + U_{p_A(t)} \sin 2\gamma_A(t)) \\ &\quad - \alpha_B (T_{p_B(t)} + Q_{p_B(t)} \cos 2\gamma_B(t) + U_{p_B(t)} \sin 2\gamma_B(t))] \\ &\quad + s_t^{\text{inst}} + n_t, \end{aligned} \quad (12)$$

where  $s_p$  is the total sky signal  $\mathbf{B}\mathbf{M}\mathbf{a}$ ,  $\gamma_{A/B}$  are the time-dependent polarization angles, and  $p_{A/B}$  are the A and B pixel locations. In this notation,  $\alpha_{A/B}$  is the total optical power transmission for horn A and B. Defining the transmission imbalance for a given radiometer pair  $x_{\text{im}} \equiv (\alpha_A - \alpha_B)/(\alpha_A + \alpha_B)$  and absorbing  $\alpha_A + \alpha_B$  into the definition of  $g_t$  allows the pointing operation to be written in terms of the deviation from ideality,

$$\begin{aligned} \mathbf{P}_{t,p} s_p &= (1 + x_{\text{im}})(T_{p_A} + Q_{p_A} \cos 2\gamma_A + U_{p_A} \sin 2\gamma_A) \\ &\quad - (1 - x_{\text{im}})(T_{p_B} + Q_{p_B} \cos 2\gamma_B + U_{p_B} \sin 2\gamma_B). \end{aligned} \quad (13)$$

For a specific realization of the components listed in this section, we display the TOD for a ten-minute segment of *WMAP*'s K113 radiometer in Fig. 1. The uncalibrated data,  $\mathbf{d}_{\text{raw}}$ , is displayed in the top panel, with the sky signal  $s_{\text{sky}} = \mathbf{P}\mathbf{B}^{\text{symm}}\mathbf{M}\mathbf{a}$  plotted directly underneath. In addition, we plot the instrumental corrections for this timestream, including the correlated noise realization  $\mathbf{n}_{\text{corr}}$ , the orbital dipole  $s_{\text{orb}}$ , the far sidelobe contribution  $s_{\text{sl}}$ , and the bandpass leakage  $s_{\text{leak}}$ . We also plot the time-ordered residual for this segment of data, in units of the estimated white noise level. We will discuss the goodness-of-fit and sampling of these quantities in the following subsections.

## 2.4. Sky model

Following BeyondPlanck (2022), we assume that the sky ( $\mathbf{a}$  in Eq. 7) can be modeled as a linear combination of CMB fluctuations ( $\mathbf{a}_{\text{CMB}}$  and  $\mathbf{a}_{\text{quad}}$ ), synchrotron ( $\mathbf{a}_s$ ), free-free emission ( $\mathbf{a}_{\text{ff}}$ ), anomalous microwave emission ( $\mathbf{a}_{\text{ame}}$ ), thermal dust ( $\mathbf{a}_d$ ), and radio point sources ( $\mathbf{a}_{j,\text{src}}$ ). The parametric sky model we adopt is given in brightness temperature units as

$$s_{\text{RJ}} = (\mathbf{a}_{\text{CMB}} + \mathbf{a}_{\text{quad}}(\nu)) \frac{x^2 e^x}{(e^x - 1)^2} + \quad (14)$$

$$+ \mathbf{a}_s \left( \frac{\nu}{\nu_{0,s}} \right)^{\beta_s} + \quad (15)$$

$$+ \mathbf{a}_{\text{ff}} \left( \frac{\nu_{0,\text{ff}}}{\nu} \right)^2 \frac{g_{\text{ff}}(\nu; T_e)}{g_{\text{ff}}(\nu_{0,\text{ff}}; T_e)} + \quad (16)$$

$$+ \mathbf{a}_{\text{ame}} e^{\beta(\nu - \nu_{0,\text{ame}})} + \quad (17)$$

$$+ \mathbf{a}_d \left( \frac{\nu}{\nu_{0,d}} \right)^{\beta_d + 1} \frac{e^{h\nu_{0,d}/k_B T_d} - 1}{e^{h\nu/k_B T_d} - 1} + \quad (18)$$

$$+ U_{\text{mJy}} \sum_{j=1}^{N_{\text{src}}} \mathbf{a}_{j,\text{src}} \left( \frac{\nu}{\nu_{0,\text{src}}} \right)^{\alpha_{j,\text{src}} - 2}. \quad (19)$$

Note that the AME model we adopt is a pure exponential, rather than the spectral energy distribution (SED) template  $s_0^{\text{sd}}(\nu)$  computed using SpDust2 (Ali-Haïmoud et al. 2009; Ali-Haïmoud 2010; Silsbee et al. 2011). The SpDust2 model was parameterized in BeyondPlanck (2022) by a peak frequency  $\nu_p$  such that

$$s_{\text{RJ}}^{\text{sd}}(\nu) \propto \nu^{-2} s_0^{\text{sd}} \left( \nu \cdot \frac{30 \text{ GHz}}{\nu_p} \right). \quad (20)$$

In the *WMAP* and LFI frequency range, the exponential model and the SpDust2 are phenomenologically quite similar, despite their very different descriptions. The exponential model is a simple fit with  $\beta$  drawn from a prior value of  $-3.57$ , and is a clear parametric form that is easy to interpret. An alternative model is the two-parameter log-normal AME SED,

$$s_{\text{RJ}}^{\text{ame,log-N}} = \mathbf{a}_{\text{ame}} \left( \frac{\nu}{\nu_{\text{ame}}} \right)^{-2} \exp \left( -\frac{1}{2} \left[ \frac{\ln(\nu/\nu_{\text{ame}})}{W_{\text{ame}}} \right]^2 \right), \quad (21)$$

derived by Stevenson (2014) as an analytical approximation to the spinning dust emission. This has also been employed in the latest QUIJOTE analysis, e.g., Tramonte et al. (2023), as it allows for variation of the peak frequency  $\nu_{\text{ame}}$  and width  $W_{\text{ame}}$ . Although this work is not dependent on the specific parametric form of the AME, we opt for the exponential form described above, as it provides an excellent fit to the diffuse AME with a single parameter.

## 2.5. Priors

The model described in Sects. 2.3 and 2.4 is prone to several degeneracies, allowing for unphysical solutions to be explored in the Gibbs chain. Some degeneracies are expected in the context of calibration – as shown in Gjerløw et al. (2022), there is a perfect degeneracy between the absolute calibration and the sky amplitude. In this case, the orbital dipole's amplitude is set by monopole temperature from Fixsen (2009). At the same time, less obvious degeneracies can become apparent in an end-to-end sampling routine. For absolute calibration, Gjerløw et al.

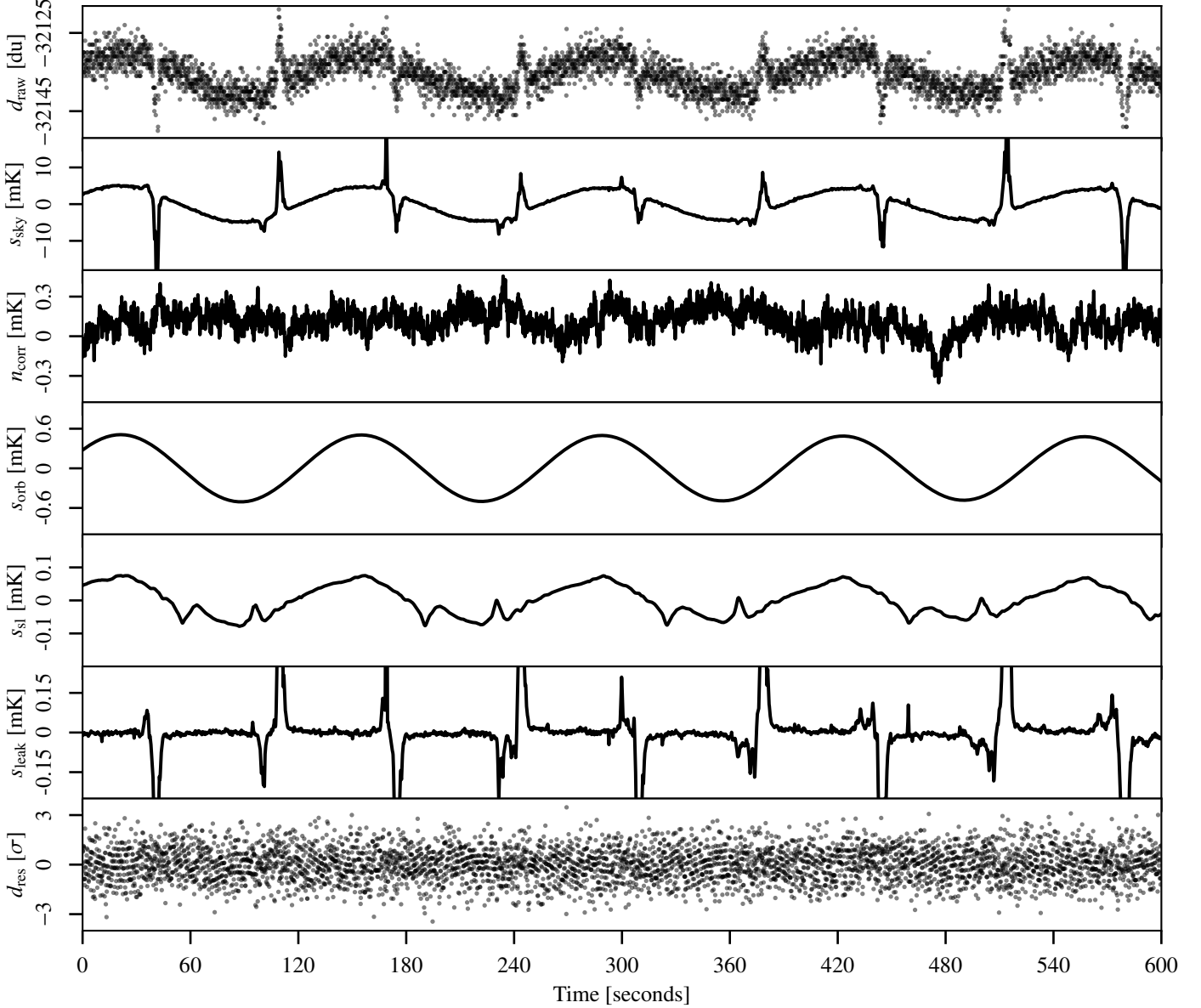


**Fig. 1.** Time-ordered data segment for the K113 radiometer. From top to bottom, the panels show 1) raw uncalibrated TOD  $\mathbf{d}$ ; 2) sky signal  $s_{\text{sky}}$ ; 3) calibrated correlated noise  $n_{\text{corr}}$ ; 4) orbital CMB dipole signal  $s_{\text{orb}}$ ; 5) sidelobe correction  $s_{\text{sl}}$ ; 6) bandpass leakage correction  $s_{\text{leak}}$ ; and 7) residual TOD,  $d_{\text{res}} = (\mathbf{d} - \mathbf{n}_{\text{corr}} - \mathbf{b})/g - s_{\text{sky}} - s_{\text{orb}} - s_{\text{leak}} - s_{\text{sl}}$ , in units of  $\sigma_0[\text{du}]$  for this TOD segment. Note that the vertical range varies significantly from panel to panel.

(2022) showed that the  $C_{\ell=2}^{\text{EE}}$  mode can mimic the orbital dipole in timestreams, necessitating applying a prior specifically on this multipole.

For component separation, the BEYONDPLANCK analysis required spatial priors on the foreground amplitudes and external priors on all spectral indices (Andersen et al. 2022).

*Write more* We added one high S/N band whose absolute calibration is highly degenerate with the sky signal. Therefore, we use the same amplitude priors, and keep the spectral indices as prior-sampled.

## 2.6. Posterior distribution and Gibbs sampling

As shown in BeyondPlanck (2022), this parametric description of the instrumental effects and sky allows us to write down a total model for the data,  $\mathbf{d} = \mathbf{s}^{\text{tot}}(\omega) + \mathbf{n}^w$ , where  $\mathbf{s}^{\text{tot}}$  encompasses all of the terms in Eq. (7) except for the white noise term. Assuming

that all instrumental effects have been modeled, the data should be Gaussian distributed with a mean of  $\mathbf{s}^{\text{tot}}(\omega)$  and variance  $\sigma_0^2$ . Given this model, we can evaluate the likelihood for arbitrary chunks of time-ordered data in the context of the entire model, so that individual chunks of data with poor fits can be more easily identified. In general, the likelihood is written

$$P(\mathbf{d} | \omega) \propto \exp\left(-\frac{1}{2} \sum_t \frac{(d_t - s_t^{\text{tot}}(\omega))^2}{\sigma_0^2}\right). \quad (22)$$

If  $\mathbf{d} \sim \mathcal{N}(\mathbf{s}^{\text{tot}}, \sigma_0^2)$  is the correct model for the data, the argument of the exponent is proportional to a  $\chi^2$ -distribution with  $n_{\text{TOD}}$  degrees of freedom. In the limit of large  $n$ , a  $\chi^2$  distribution is well-approximated by a Gaussian with mean  $n$  and variance  $2n$ . Therefore we define and use the reduced- $\chi^2$  statistic,

$$\chi^2 \equiv \frac{\sum_t ((d_t - s_t^{\text{tot}})^2 / \sigma_0^2) - n_{\text{TOD}}}{\sqrt{2n_{\text{TOD}}}}, \quad (23)$$

which is approximately drawn from the standard normal distribution  $\mathcal{N}(0, 1)$ .

The COSMOGLOBE Gibbs chain is given by

$$\mathbf{g} \leftarrow P(\mathbf{g} \mid \mathbf{d}, \xi_n, \mathbf{s}^{\text{inst}}, \boldsymbol{\beta}, \mathbf{a}, C_\ell, \theta) \quad (24)$$

$$\mathbf{n}_{\text{corr}} \leftarrow P(\mathbf{n}_{\text{corr}} \mid \mathbf{d}, \mathbf{g}, \xi_n, \mathbf{s}^{\text{inst}}, \boldsymbol{\beta}, \mathbf{a}, C_\ell, \theta) \quad (25)$$

$$\xi_n \leftarrow P(\xi_n \mid \mathbf{d}, \mathbf{g}, \mathbf{n}_{\text{corr}}, \mathbf{s}^{\text{inst}}, \boldsymbol{\beta}, \mathbf{a}, C_\ell, \theta) \quad (26)$$

$$\mathbf{s}^{\text{inst}} \leftarrow P(\mathbf{s}^{\text{inst}} \mid \mathbf{d}, \mathbf{g}, \mathbf{n}_{\text{corr}}, \xi_n, \boldsymbol{\beta}, \mathbf{a}, C_\ell, \theta) \quad (27)$$

$$\boldsymbol{\beta} \leftarrow P(\boldsymbol{\beta} \mid \mathbf{d}, \mathbf{g}, \mathbf{n}_{\text{corr}}, \xi_n, \mathbf{s}^{\text{inst}}, C_\ell, \theta) \quad (28)$$

$$\mathbf{a} \leftarrow P(\mathbf{a} \mid \mathbf{d}, \mathbf{g}, \mathbf{n}_{\text{corr}}, \xi_n, \mathbf{s}^{\text{inst}}, \boldsymbol{\beta}, C_\ell, \theta) \quad (29)$$

$$C_\ell \leftarrow P(C_\ell \mid \mathbf{d}, \mathbf{g}, \mathbf{n}_{\text{corr}}, \xi_n, \mathbf{s}^{\text{inst}}, \boldsymbol{\beta}, \mathbf{a}, \theta) \quad (30)$$

$$\theta \leftarrow P(\theta \mid \mathbf{d}, \mathbf{g}, \mathbf{n}_{\text{corr}}, \xi_n, \mathbf{s}^{\text{inst}}, \boldsymbol{\beta}, \mathbf{a}, C_\ell), \quad (31)$$

with each step requiring its own dedicated sampling algorithm. The Commander3 pipeline is designed so that results of each Gibbs sample can be easily passed to each other, and that the internal calculations of each step do not directly depend on the inner workings of each other. Therefore, in order to add another data set to the Gibbs chain, one can either add a map or TODs. To add a TOD, one must implement Eqs. (24)–(27) for each instrument, as was done in BeyondPlanck (2022) and Basyrov et al. (2022) for *Planck* LFI and in Watts et al. (2022) for WMAP. To add a map, one must simply pass processed maps with beam, mask, and noise information to Eqs. (28)–(31), as was done for the Haslam 408 MHz map (Haslam et al. 1982; Remazeilles et al. 2015) and the *Planck* 353 and 857 GHz maps.

Before we discuss the results of this Gibbs chain as applied to the *Planck* LFI and WMAP data, we summarize the TOD processing steps in Sect. 2.7.

## 2.7. Sampling algorithms

Each step of the Gibbs chain requires its own distribution to be sampled from. In Sect. 2.7.1 we review the sampling algorithms implemented in the BEYONDPLANCK suite of papers, while Sects. 2.7.2–2.7.4 provide an overview of the WMAP-specific processing steps.

### 2.7.1. Review of sampling algorithms

Several of the techniques required for WMAP data analysis have already been implemented and described in the BEYONDPLANCK framework and implemented in Commander3. This section includes a summary of the algorithms that were used previously for the analysis of LFI data. In each of these cases, every part of the model not explicitly mentioned is held fixed unless specified otherwise.

Noise estimation and calibration, described in Ihle et al. (2022) and Gjerløw et al. (2022) respectively, are highly degenerate, given that the timestream

$$d_{t,i} = g_{q,i} s_{t,i}^{\text{tot}} + n_{t,i}^{\text{corr}} + n_{t,i}^{\text{wn}} \quad (32)$$

is equally well fit by two solutions if  $g' = gs^{\text{tot}}/(s^{\text{tot}})'$  or  $(n^{\text{corr}})' = n^{\text{corr}} + gs^{\text{tot}} + g'(s^{\text{tot}})'$ . In practice, this is dealt with by marginalizing over the correlated noise realization  $\mathbf{n}^{\text{corr}}$  assuming a fixed PSD  $\xi_n$ , so that Eqs. (24) and (25) are evaluated as

$$\mathbf{g} \leftarrow P(\mathbf{g} \mid \mathbf{d}, \xi_n, \dots) \quad (33)$$

$$\mathbf{n}_{\text{corr}} \leftarrow P(\mathbf{n}_{\text{corr}} \mid \mathbf{d}, \mathbf{g}, \xi_n, \dots). \quad (34)$$

This is allowed by probability theory given that the joint distribution  $P(\mathbf{g}, \mathbf{n}_{\text{corr}} \mid \omega) = P(\mathbf{n}_{\text{corr}} \mid \mathbf{g}, \omega)P(\mathbf{g} \mid \omega)$ , so that Eqs. (33) and (34) evaluated in sequence is equivalent to drawing a joint sample from  $P(\mathbf{g}, \mathbf{n}_{\text{corr}} \mid \omega)$ . In practice, this means that when sampling for  $\mathbf{g}$ , the covariance matrix  $\mathbf{N} = \mathbf{N}_{\text{wn}} + \mathbf{N}_{\text{corr}}$  must be used, rather than just  $\mathbf{N}_{\text{wn}}$ .

Commander3 models the gain at each timestream  $t$  for a detector  $i$  as

$$g_{t,i} = g_0 + \Delta g_i + \delta g_{q,i} \quad (35)$$

where  $q$  labels the time interval for which we assume the gain is constant over, e.g., a single scan. In order to sample the gain, we write down a generative model for the TOD,

$$\mathbf{d}_i = \mathbf{g}_i s_i^{\text{tot}} + \mathbf{n}_i^{\text{tot}} \sim \mathcal{N}(\mathbf{g}_i s_i^{\text{tot}}, \mathbf{N}_i). \quad (36)$$

Since the  $\mathbf{d}_i$  is given as a linear combination of the fixed signal and the gains, a random sample of the gain can be drawn by solving<sup>3</sup>

$$[(s_i^{\text{tot}})^T \mathbf{N}_i^{-1} s_i^{\text{tot}}] \mathbf{g}_i = (s_i^{\text{tot}})^T \mathbf{N}_i^{-1} \mathbf{d}_i + (s_i^{\text{tot}})^T \mathbf{N}_i^{-1/2} \boldsymbol{\eta}. \quad (37)$$

Note that the  $\mathbf{N}_i$  depends implicitly on the noise PSD  $\xi_n$ , while the specific realization of  $\mathbf{n}_{\text{corr}}$  is accounted for in the covariance matrix. In practice, as shown in Gjerløw et al. (2022), Commander3 samples  $g_0$ ,  $\Delta g_i$ , and  $\delta g_{q,i}$  in separate sampling steps. Formally, the Gibbs chain is broken by fitting the absolute gain  $g_0$  to the orbital dipole rather than the full sky signal. However, this makes the sampling much more robust to unmodeled systematic effects, so the trade-off in rigor is justified.

The correlated noise sampling, described in Ihle et al. (2022), follows a similar procedure to gain sampling, except now conditioned upon the gain estimate, sampled just before correlated noise in the code. Similar to the gain case, we can write a generative model for the data

$$\mathbf{d}_i = \mathbf{g}_i s_i^{\text{tot}} + \mathbf{n}_i^{\text{corr}} + \mathbf{n}_i^{\text{wn}} \sim \mathcal{N}(\mathbf{g}_i s_i^{\text{tot}}, \mathbf{N}_{\text{corr},i} + \mathbf{N}_{\text{wn},i}). \quad (38)$$

Given fixed  $\mathbf{r}_i = \mathbf{d}_i - \mathbf{g}_i s_i^{\text{tot}}$ , we can again write a sampling equation,

$$(\mathbf{N}_{\text{corr},i}^{-1} + \mathbf{N}_{\text{wn},i}^{-1}) \mathbf{n}_i^{\text{corr}} = \mathbf{N}_{\text{wn},i}^{-1} \mathbf{r}_i + \mathbf{N}_{\text{wn},i}^{-1/2} \boldsymbol{\eta}_1 + \mathbf{N}_{\text{corr},i}^{-1/2} \boldsymbol{\eta}_2. \quad (39)$$

This gives a sample of the true underlying correlated noise that occurred when the instrument was taking data. In practice, this is equivalent to the destriping mapmaking algorithm Madam, and returns equivalent results to the classical method (Keihänen et al. 2022).

To solve for the correlated noise parameters, we assume that the correlated noise is drawn from a correlated Gaussian and form the posterior distribution

$$P(\xi_n \mid \mathbf{n}^{\text{corr}}) \propto \frac{\exp[-\frac{1}{2}(\mathbf{n}^{\text{corr}})^T \mathbf{N}_{\text{corr}}^{-1} \mathbf{n}^{\text{corr}}]}{\sqrt{|\mathbf{N}_{\text{corr}}|}} P(\xi_n). \quad (40)$$

The simplest parameterization for correlated noise is given by

$$\mathbf{N}_{\text{corr}}(f) = \sigma_0^2 \left( \frac{f}{f_{\text{knee}}} \right)^\alpha. \quad (41)$$

This can in principle be modified, and for *Planck* LFI a Gaussian log-normal bump was added at a late stage in the BEYONDPLANCK analysis. Rather than sampling for  $\sigma_0$ , we effectively fix

<sup>3</sup> See, e.g., Appendix A.2 of BeyondPlanck (2022) for a derivation of this result.

the white noise level to the noise level at the highest frequency, e.g.,

$$\sigma_0^2 \equiv \frac{\text{Var}(r_{t+1} - r_t)}{2}, \quad (42)$$

where  $t$  and  $t + 1$  are consecutive time samples, and  $\mathbf{r} \equiv \mathbf{d} - \mathbf{gs}^{\text{tot}} - \mathbf{n}^{\text{corr}}$ . In practice, this makes  $\sigma_0$  a deterministic function of the sampled sky and gain parameters. The parameters  $\alpha$  and  $f_{\text{knee}}$  are not linear in the data, so must be sampled using the general inversion sampler.<sup>4</sup> In practice, this requires computing the posterior over a linear grid one parameter at a time.

Once the instrumental parameters have been sampled, Commander3 computes the calibrated TOD for each band,

$$r_{t,j} = \frac{d_{t,j} - n_{t,j}^{\text{corr}}}{g_{t,j}} - (s_{t,j}^{\text{orb}} + s_{t,j}^{\text{fsl}} + \delta s_{t,j}^{\text{leak}} + s_{t,j}^{\text{inst}}) \quad (43)$$

where  $s^{\text{orb}}$  is the orbital dipole,  $s^{\text{fsl}}$  is the far sidelobe timestream,  $\delta s^{\text{leak}}$  is the bandpass leakage, and  $s^{\text{inst}}$  is the set of instrumental parameters, e.g., the 1 Hz spike in LFI. With a correlated noise realization removed, one can perform simple binned mapmaking, weighting each pixel by the white noise amplitude.

### 2.7.2. Differential mapmaking

The first additional algorithm that needed to be added to Commander3 when adding WMAP TOD data was differential mapmaking, since the *Planck* LFI data came from a standard single-horn instrument.

After calibration and correction for instrumental effects, the TOD can be modeled as

$$\mathbf{d} = \mathbf{P}\mathbf{m} + \mathbf{n}^{\text{w}}, \quad (44)$$

where

$$\mathbf{m} = \mathbf{B}^{\text{symm}} \mathbf{M} \mathbf{a} \quad (45)$$

is the expected map for each detector after removing the orbital dipole, far sidelobe, baseline, and a realization of correlated noise. The differential pointing strategy can be represented in matrix form as

$$\mathbf{P}_{tp} = (1 + x_{\text{im}})(\delta_{p' p_A'} + \delta_{p' p_A^o} \cos 2\psi_A + \delta_{p' p_A^u} \sin 2\psi_A) \quad (46)$$

$$- (1 - x_{\text{im}})(\delta_{p' p_B'} - \delta_{p' p_B^o} \cos 2\psi_B - \delta_{p' p_B^u} \sin 2\psi_B) \quad (47)$$

where  $p_A$  and  $p_B$  are the time-dependent pointings for each DA. The maximum likelihood map can in principle be solved using the usual mapmaking equation,

$$\mathbf{P}^T \mathbf{N}^{-1} \mathbf{P} \mathbf{m} = \mathbf{P}^T \mathbf{N}^{-1} \mathbf{d}. \quad (48)$$

For a single-horn experiment, i.e., *Planck* LFI, this reduces to a  $3 \times 3$  matrix that can be inverted for each pixel independently. For the pointing matrix in Eq. (46), this is no longer possible, as there is inherently coupling between horns A and B in the timestreams. The  $3N_{\text{pix}} \times 3N_{\text{pix}}$  matrix can be solved using an iterative algorithm, e.g., preconditioned conjugate gradients.

Jarosik et al. (2011) identified an issue where a large difference in the sky temperature values at pixel value at pixel A versus pixel B induced artifacts in the mapmaking procedure.

<sup>4</sup> See, e.g., Appendix A.3 of BeyondPlanck (2022) and Chapter 7.3.2 of Press et al. (2007) for further details.

We adopt the procedure first described in Hinshaw et al. (2003) where only the pixel in a bright region, defined by a small processing mask (Bennett et al. 2013) is accumulated, thus modifying the mapmaking equation to

$$\mathbf{P}_{\text{am}}^T \mathbf{N}^{-1} \mathbf{P} \mathbf{m} = \mathbf{P}_{\text{am}}^T \mathbf{N}^{-1} \mathbf{d}. \quad (49)$$

This equation can be solved using the BiCG-STAB algorithm for a non-symmetric matrix  $\mathbf{A}$  where  $\mathbf{Ax} = \mathbf{b}$ . We apply a preconditioner  $\mathbf{M}$  by numerically inverting the same problem with  $N_{\text{side}} = 16$  maps and applying a diagonal noise matrix. Numerically, we define convergence as when the residual  $\mathbf{r} \equiv \mathbf{b} - \mathbf{Ax}$  satisfies  $\mathbf{r}^T \mathbf{M}^{-1} \mathbf{r} / \mathbf{b}^T \mathbf{M}^{-1} \mathbf{b} < 10^{-10}$ , which typically takes about 20 iterations for producing frequency maps.

### 2.7.3. Transmission imbalance estimation

Transmission imbalance, i.e., the differential power transmission of the optics and waveguide components, can be parameterized as

$$d_{t,j} = g_{t,j}[(1 + x_{\text{im},j})s_{t,j}^{\text{tot,A}} - (1 - x_{\text{im},j})s_{t,j}^{\text{tot,B}}] + n_t. \quad (50)$$

This can be decomposed into a differential (d) and common-mode (c) signal such that

$$d_{t,j} = g_{t,j}[s_{t,j}^{\text{d}} + x_{\text{im},j}s_{t,j}^{\text{c}}] + n_t. \quad (51)$$

In this form, the imbalance parameters can be estimated by drawing Gaussian samples from the standard mean and standard deviation over the entire mission. To draw samples for  $x_{\text{im},j}$ , we construct the sampling routine analogous to Eqs. (37) and (39) with  $\mathbf{r} = \mathbf{d} - \mathbf{gs}^{\text{d}}$ ,

$$[(\mathbf{gs}^{\text{c}})^T \mathbf{N}^{-1} \mathbf{gs}^{\text{c}}]x_{\text{im}} = (\mathbf{gs}^{\text{c}})^T \mathbf{N}^{-1} \mathbf{r} + (\mathbf{gs}^{\text{c}})^T \mathbf{N}^{-1/2} \boldsymbol{\eta}, \quad (52)$$

essentially cross-correlating the common-mode signal with  $\mathbf{r}$  with appropriate weights and adding a Gaussian random variable with the correct weighting. Note that we are marginalizing over the correlated noise here by using  $\mathbf{N} = \mathbf{N}_{\text{wn}} + \mathbf{N}_{\text{corr}}$ . This mitigates any baseline drifts being erroneously attributed to the common-mode signal and biasing the estimate of  $x_{\text{im}}$ .

The WMAP procedure, described in Jarosik et al. (2003a), fit for common-mode and differential coefficients along with a cubic baseline over 10 precession periods at a time, corresponding to 10 hours of observation. The mean and uncertainty were then calculated by averaging and taking the standard deviation of these values. This approach has the benefit of allowing for the tracking of possible transmission imbalance variation throughout the mission. However, none of the WMAP suite of papers have indicated this, and it has not arisen in our analysis, so we model this as an effect whose value is constant throughout the mission.

### 2.7.4. Baseline sampling

The data model adopted in Hinshaw et al. (2003) can be written in raw digital units (du) as

$$\mathbf{d} = \text{GPBM} \mathbf{a} + \mathbf{n} + \mathbf{b}, \quad (53)$$

where  $\mathbf{b}$  is the instrumental baseline and  $\mathbf{n}$  is the total instrumental noise. As detailed in Ihle et al. (2022), Commander3 divides the noise into  $\mathbf{n} = \mathbf{n}^{\text{w}} + \mathbf{n}^{\text{corr}}$ , a white noise term and a correlated noise term. By definition, the white noise does not have any correlations between adjacent pixels, so that any pixel-pixel

covariance should be fully described by realizations of the  $\mathbf{n}^{\text{corr}}$  timestream.

**Commander** estimates the baseline using the full estimate of the current sky model,  $\mathbf{r} = \mathbf{d} - g\mathbf{s}^{\text{tot}} = \mathbf{b} + \mathbf{n}$ . Modeling  $\mathbf{b} = b_0 + b_1\Delta t$ , we solve for  $b_0$  and  $b_1$  using linear regression in each timestream while masking out samples that lie within the processing mask. Strictly speaking, this is breaking the Gibbs chain, as we are not formally sampling  $b_0$  and  $b_1$  for each TOD chunk. In practice, baseline estimation uncertainty propagates to correlated noise realizations and PSD parameters, as discussed below.

The approach detailed in Hinshaw et al. (2003) and the **Commander** implementation differ mainly in the assumed stable timescale – the initial *WMAP* baseline is estimated over one hour timescales, whereas **Commander** assumes constant values throughout the entire timestream, 3–7 days depending on the band in question. As noted in Hinshaw et al. (2003), residual baseline variations manifest as correlated noise stripes in the final maps. *WMAP9* solves this using a time-domain filter, downweighting the data based off of the noise characterization. This approach is equivalent to the **Commander3** procedure of removing a constrained realization of correlated noise from the timestream directly, based on the best-fit to the noise PSD.

### 3. Data and data processing

We describe the delivered *WMAP* data in Sect. 3.1, then describe the treatment we apply it to make them compatible with **Commander3** in Sect. 3.2, then describe the computational requirements in Sect. 3.3.

#### 3.1. Publicly available WMAP products

The full *WMAP* dataset is hosted at the Legacy Archive for Microwave Background Data Analysis (LAMBDA).<sup>5</sup> In addition to the primary scientific products, e.g., cosmological parameters, CMB power spectra and anisotropy maps, and frequency maps, the time-ordered data (TOD) can be downloaded, both in uncalibrated and calibrated form.<sup>6</sup> In principle, thanks to these data and the explanatory supplements (Greason et al. 2012), the entire data analysis pipeline can be reproduced from TOD in digital units (du) to frequency maps.

For this analysis, we keep certain instrumental parameters fixed to the reported values. For example, we have made no attempts to rederive the pointing solutions, re-estimate the main beam response and far sidelobe pickup, or recover data that was flagged in the *WMAP* event log. These and other analyses, such as estimating the bandpass shift over the course of the mission, are certainly possible within the larger Gibbs sampling framework. However, in this work we limit ourselves to recalibrating the TOD, estimating the noise properties, and applying bandpass corrections to the data before mapmaking.

#### 3.2. TOD pre-processing and data selection

The full nine-year *WMAP* archive spans from August 10, 2001 to August 10, 2010, with the raw uncalibrated data spanning 626 GB. A little over 1 % of the data were lost or rejected due to incomplete satellite telemetry, thermal disturbances, spacecraft

**Table 1.** Flagging statistics

Band	Flagged (%)	Discarded (%)	Used (%)
$K$	1.72	0.87	97.4
$Ka$	1.64	0.88	97.5
$Q1$	1.84	0.84	96.5
$Q2$	1.62	0.81	97.6
$V1$	1.62	1.10	97.3
$V2$	1.61	1.01	97.4
$W1$	1.76	1.03	97.2
$W2$	1.60	0.81	97.6
$W3$	1.61	0.87	97.5
$W4$	1.60	0.81	97.6

anomalies, and station-keeping maneuvers, with an extra 0.1 % rejected due to planet flagging (Bennett et al. 2003b; Hinshaw et al. 2007, 2009; Bennett et al. 2013). The final results reported in Bennett et al. (2013) included roughly 98.4 % of the total data volume. A full accounting of all data cuts can be found in Table 1.8 of Greason et al. (2012). In total, we flag the same data indicated in the fiducial *WMAP* analysis, and use the same planet flags.

As shown in Galloway et al. (2022), a large fraction of **Commander3**'s computational time is spent performing FFTs on individual scans. Rather than truncating datastreams to have lengths equal to “magic numbers” for which FFTW (Frigo & Johnson 2005) is fastest, as in Galloway et al. (2022), we redistribute the data into scans of length  $2^N$ , where  $N = 22$  for  $K-Q$ ,  $N = 23$  for  $V-W$ . This yields scans with lengths of 6.21 days for  $K$ - and  $Ka$ -band, 4.97 days for  $Q$ -band, 7.46 days for  $V$ -band, and 4.97 days for  $W$ -band. These datastream lengths are short enough to be processed quickly and distributed efficiently across multiple processors, while being long enough to properly characterize the noise properties of the timestreams, whose  $f_{\text{knee}}$  values are on the order 1 mHz. Most importantly, FFTW performs fastest when the datastream is of length  $2^N$ .

When redistributing the data, timestreams of length  $2^N$  were interrupted by events logged in Table 1.8 of Greason et al. (2012). When we encountered these events, TOD segments that were interrupted by the event were appended to the previous TOD, in most cases creating TODs with lengths  $> 2^N$ . We found that events of length  $< 2^N$  were too short to accurately estimate the noise PSD parameters. This criterion led us to discard these otherwise useful data. In addition, when  $> 10\%$  of the TOD was flagged, the large number of gaps in the data made the constrained realizations unreliable, as well as biasing the noise PSD parameters. Together, these two effects led to  $\simeq 1\%$  of the data to be discarded despite being of acceptable quality. We present the full flagging statistics for our maps in Table 1. In total, the COSMOGLOBE maps use slightly less data than the *WMAP9* official products, which had a total efficiency of  $\simeq 98.4\%$  (Bennett et al. 2013). The total difference in data volume can be entirely accounted for by the cuts described in this paragraph.

#### 3.3. Computational resources

A key motivation of the COSMOGLOBE project is to evaluate whether it is feasible to perform a joint analysis of two datasets simultaneously, each with its own particular processing requirements and algorithmic treatment. One of the results from Watts et al. (2022) was that most of the data processing procedures for *WMAP* and *Planck* LFI overlapped, with the notable exception of mapmaking. While the algorithmic requirements have been

<sup>5</sup> [https://lambda.gsfc.nasa.gov/product/wmap/dr5/m\\_products.html](https://lambda.gsfc.nasa.gov/product/wmap/dr5/m_products.html)

<sup>6</sup> [https://lambda.gsfc.nasa.gov/product/wmap/dr5/tod\\_info.html](https://lambda.gsfc.nasa.gov/product/wmap/dr5/tod_info.html)

**Table 2.** Computational resources required for end-to-end COSMOGLOBE processing. All times correspond to CPU hours, and all data volumes are reported in GB. Reported times are averaged over more than 100 samples, and vary by  $\lesssim 5\%$  from sample to sample.

ITEM	30	44	70	K	$Ka$	$Q1$	$Q2$	$V1$	$V2$	$W1$	$W2$	$W3$	$W4$	SUM
<i>Data volume</i>														
Compressed TOD volume . . . . .	86	178	597	13	12	15	15	19	18	26	26	26	26	1 053
<i>Processing time (cost per run)</i>														
TOD initialization/IO time . . . . .	1.8	2.5	9.3	0.3	0.3	0.4	0.4	0.4	0.4	0.5	0.5	0.5	0.5	17.8
Other initialization . . . . .														13.4
<b>Total initialization</b> . . . . .														<b>31.2</b>
<i>Gibbs sampling steps (cost per sample)</i>														
Huffman decompression . . . . .	1.1	2.1	10.5	0.9	0.8	1.0	1.0	1.3	1.3	1.8	1.8	1.8	1.8	27.2
TOD projection ( $P$ operation) . . . . .	0.4	0.9	4.2	2.6	2.6	3.3	3.4	4.3	4.3	6.4	6.3	6.3	6.4	54.0
Sidelobe evaluation . . . . .	1.0	2.1	7.6	2.9	2.9	3.5	3.5	4.7	4.8	7.0	6.9	6.9	6.9	60.7
Orbital dipole . . . . .	0.9	1.9	7.1	1.3	1.3	1.7	1.7	2.2	2.3	3.4	3.3	3.3	3.3	33.7
Gain sampling . . . . .	0.5	0.8	1.9	0.8	0.8	0.5	0.5	0.9	0.9	0.7	0.7	0.7	0.7	10.4
1 Hz spike sampling . . . . .	0.3	0.4	1.6											2.4
Correlated noise sampling . . . . .	2.0	4.0	21.7	2.8	2.9	3.3	3.6	5.1	5.4	8.0	7.7	7.2	8.5	81.3
Correlated noise PSD sampling . . . . .	4.8	5.9	1.5	0.2	0.2	0.3	0.3	0.5	0.4	0.7	0.6	0.6	0.7	16.7
TOD binning ( $P'$ operation) . . . . .	0.1	0.1	4.0	0.5	0.5	0.7	0.8	0.8	0.8	1.2	1.2	1.2	1.2	13.1
Mapmaking . . . . .						6.4	7.0	8.9	8.1	11.1	9.5	14.4	14.3	119.5
Sum of other TOD processing . . . . .	4.4	8.6	44.4	14.7	4.6	5.1	5.0	9.4	7.7	8.1	6.8	8.6	8.7	136.1
<b>TOD processing cost per sample</b>	<b>15.5</b>	<b>26.8</b>	<b>104.5</b>	<b>23.0</b>	<b>24.1</b>	<b>27.6</b>	<b>27.9</b>	<b>40.3</b>	<b>37.4</b>	<b>51.7</b>	<b>50.6</b>	<b>51.9</b>	<b>54.6</b>	<b>535.9</b>
Amplitude sampling . . . . .														14.0
Spectral index sampling . . . . .														25.5
<b>Total cost per sample</b> . . . . .														<b>581.2</b>

discussed in Sect. 2, we have not yet quantified the requirements in terms of RAM and CPU hours. In Table 2, we enumerate the RAM requirements and CPU time for each sampling step using the local cluster at the Institute of Theoretical Astrophysics at the University of Oslo. The node that these numbers come from used 128 cores of an AMD EPYC 7H12, 2.6 GHz machine with 2 TB of memory. As Commander3 is parallelized and used 128 cores, wall hours in Table 2 can be obtained by dividing by 128.

Despite the relatively small data volume spanned by *WMAP*, the CPU time is comparable to each of the LFI channels. By far the largest reason for this is the mapmaking step, which requires looping over the entire dataset for each matrix multiplication, a process which must be repeated  $\sim 20$  times. This is vastly sped up by the use of a low resolution preconditioner, reducing the number of iterations by an order of magnitude.

Additionally, operations that require creating timestreams for each detector, i.e., TOD projection, sidelobe evaluation, and orbital dipole projection, take much longer than expected from a pure data volume scaling. Part of this is due to each *WMAP* radiometer needing to evaluate the sky in two pixels simultaneously, doubling the expected workload. The operations of gain sampling and correlated noise sampling include multiple FFTs. Typical LFI TODs are of length  $\sim 200\,000$ , an order of magnitude smaller than the *WMAP* TODs of length  $2^{22}-2^{23}$ .

## 4. Instrumental parameters

### 4.1. Trace plots and correlations

To illustrate the dependence of the goodness-of-fit on the noise model, we inspect the 50th TOD segment, corresponding to MJDs 52285.2–52290.6, as a function of Gibbs iteration, in Fig. 3. This is one of the worst-fitting TOD segments of the entire mission, with a reduced relative  $\chi^2$  of  $-7.5$ , equivalent to  $\chi^2/n = 0.993$ . The line plots demonstrate a strong correlation

between the noise parameters and the  $\chi^2$ , while the gain itself is almost completely uncorrelated with the variations in the  $\chi^2$ . As  $\sigma_0$  is not formally sampled in the Gibbs chain, it is weakly dependent on  $f_{\text{knee}}$  and  $\alpha$ , making it more likely that it is the driver of the correlations in this figure.

### 4.2. Gain and baselines

To compare the calibrated TODs from *WMAP* versus COSMOGLOBE, it is important to look at the *WMAP* gain model,

$$g = \alpha \frac{\bar{V} - V_0 - \beta(T_{\text{RXB}} - 290\text{ K})}{T_{\text{FPA}} - T_0} + (m\Delta t + c), \quad (54)$$

where  $\alpha$ ,  $V_0$ ,  $\beta$ ,  $T_0$ ,  $m$ , and  $c$  are fit to a constant value across the mission for each radiometer.  $\bar{V}$  represents the radio frequency bias powers per detector, and  $T_{\text{RXB}}$  and  $T_{\text{FPA}}$  are the receiver box and focal plane assembly temperatures, which are recorded every 23.04 s. Evaluating the model as a function of  $T_{\text{RXB}}$  and  $T_{\text{FPA}}$  requires finding the housekeeping data for the thermistor that was physically closest to the relevant radiometer's focal plane on the satellite. As this requires detailed technical information about the specifications of the satellite's schematics layout that can easily be misunderstood, we do not attempt to reproduce the gain model given in Eq. (54) in this work. Although we are unable to reproduce the exact gain model parametrized in Greason et al. (2012), the 23.04 s time dependence of the gain model on housekeeping data is a plausible explanation for the time-dependent noise variation in the different calibrated data solutions.

As reported in Hinshaw et al. (2007), the calibrated data archive has been calibrated using the procedure listed above, with a baseline subtracted each hour and the sidelobe subtracted. Figure 5 shows the COSMOGLOBE timestream  $d/g - s_{\text{sl}} - b$  with the *WMAP* delivered calibrated signal subtracted. The most promi-

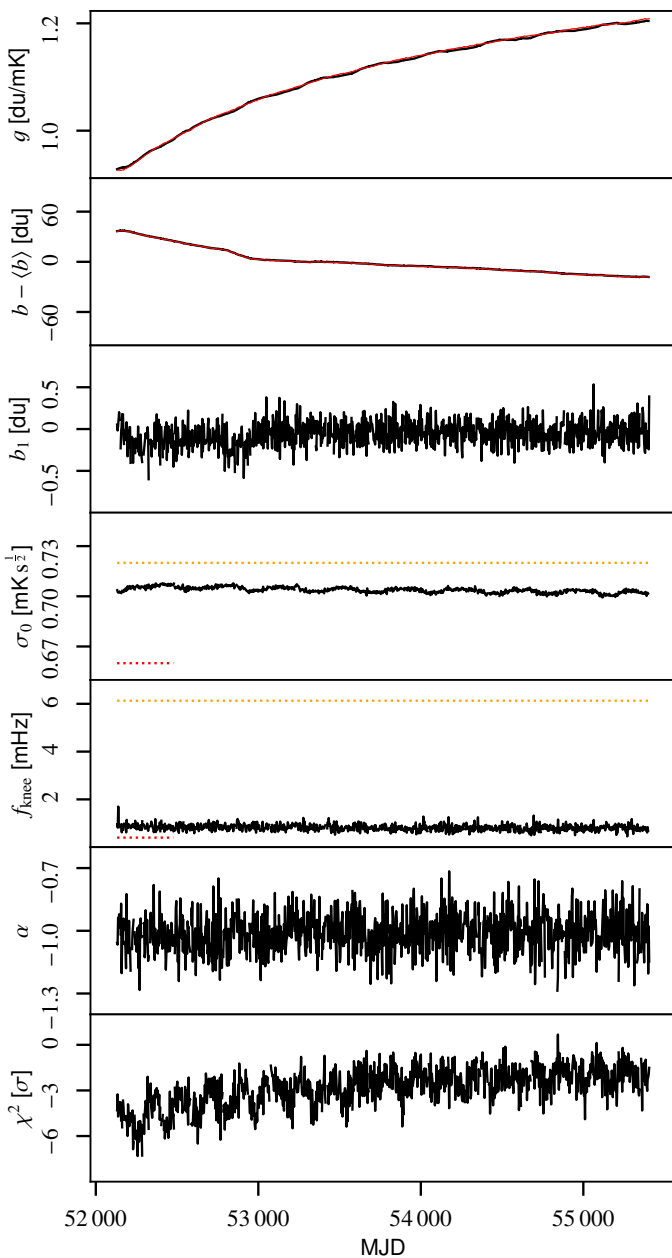


**Fig. 2.** Overview of K113. The red solid lines in first and second panel are the regressed gain and baseline from WMAP9, while the black lines in all panels are samples from the COSMOGLOBE Gibbs chain. The red dashed and yellow dashed lines are reported  $\sigma_0$  and  $f_{\text{knee}}$  values from the first-year WMAP data analysis and GSFC measurements, respectively.

ment feature is a  $\sim 25 \mu\text{K}$  offset, which is unsurprising, given the different treatment of baselines in our two pipelines. The second obvious difference is a series of spikes associated with Galactic plane crossings. The differences of order  $50 \mu\text{K}$  correspond to sky brightness of order  $10 \text{ mK}$ , equivalent to  $\sim 0.5\%$  deviations in the gain solution. This is twice as large as the  $0.2\%$  uncertainty estimated in Bennett et al. (2013) based on end-to-end simulations.

On longer timescales, as displayed in Figure 6, the most prominent feature is a varying signal of amplitude  $0.2 \text{ mK}$ . This likely due to the hourly baseline subtraction mentioned above, which contrasts with the COSMOGLOBE approach of assigning a linear baseline solution for the entire scan. The variations are commensurate with correlated noise, which for K113

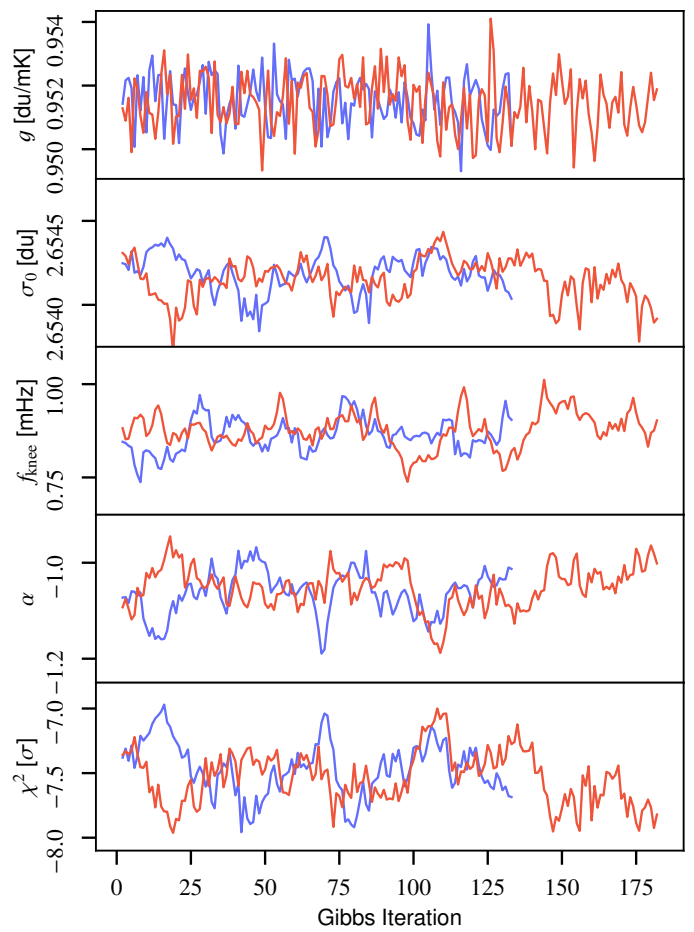


**Fig. 3.** Subset of K113 Gibbs samples for both chains, arbitrarily colored red and blue. The parameters correspond to MJDs 52285.2–52290.6.

has  $f_{\text{knee}} \sim 0.5 \text{ mHz}$ , corresponding to a little over half an hour. Therefore, the hourlong baseline subtraction essentially acts as a destriper, removing an estimate of the correlated noise. To test this hypothesis, we plot a realization of correlated noise generated by Commander, and find that the signals are very similar, both in amplitude and morphology.

We also compare the gain and baseline solutions throughout the course of the mission in Fig. 2. To recover the WMAP9 gain solution, we directly compare the uncalibrated WMAP data with the calibrated WMAP data with a far sidelobe contribution convolved with the delivered WMAP9 DA maps. We find that the calibrated and uncalibrated data can be related by

$$d_t^{\text{raw}} = g(d_t^{\text{cal}} + s_t^{\text{sl}}) + \sum_{i=0}^3 c_i(t - t_0)^i, \quad (55)$$

where the second term is a cubic polynomial with coefficients  $c_i$  referenced to the time at the beginning of the scan  $t_0$ . To calculate  $s_t^{\text{sl}}$ , we convolve the WMAP far sidelobes with WMAP9 frequency maps with the Solar dipole from Hinshaw et al. (2009) added back in. We find that  $d^{\text{raw}}$  is consistent with the expression on the right at the level of  $< 0.1 \text{ du}$  for all radiometers, suggesting that this estimate of  $g$  and the baseline  $c_0$  is a good approximation of the WMAP9 calibration solution. An initial estimate using a linear baseline gave an unacceptably poor fit. Given that Eq. (2) of Jarosik et al. (2003a) employed a cubic baseline fit while fitting for transmission imbalance parameters, it is reason-



**Fig. 4.** Noise parameter correlation matrix. We average over all Gibbs samples of the noise parameters  $\xi^n = \{\alpha, f_{\text{knee}}, \sigma_0\}$  for each PID. We then find the correlation in time between these averages for the different bands and detector. The results here are for the calibrated white noise level,  $\sigma_0$ [mK]. The values for each detector are ordered 13, 14, 23, and 24.

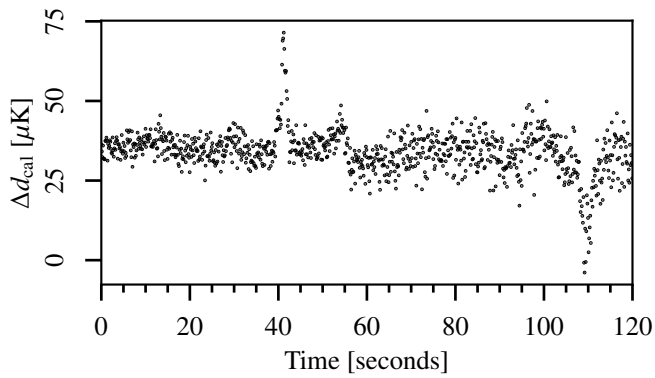


**Fig. 5.** Difference between the CosMOGLOBE  $d_{\text{cal}} = d/g - b - s_{\text{sl}}$  and the delivered calibrated TOD from WMAP.

able to assume that the official calibrated archive was created using a similar procedure.

The morphological characteristics of the *WMAP9* and CosMOGLOBE gain solutions are similar, with a general trend to increase with time. Both solutions also follow a sinusoidal pattern, corresponding to temperature change due to L2's motion around the Sun (Greason et al. 2012). However, we do find the CosMOGLOBE *K*-band gain has slightly more oscillatory features than the *WMAP9* solution. In general, the gains are consistent between CosMOGLOBE and *WMAP9* within 1 %. For completeness, the full gain comparisons can be found in Fig. A.3.

#### 4.3. Transmission imbalance

The transmission imbalance parameters  $x_{\text{im}}$  are crucial to measure correctly because their misestimation can induce a large polarized signal that is coupled to the Solar dipole (Jarosik et al.

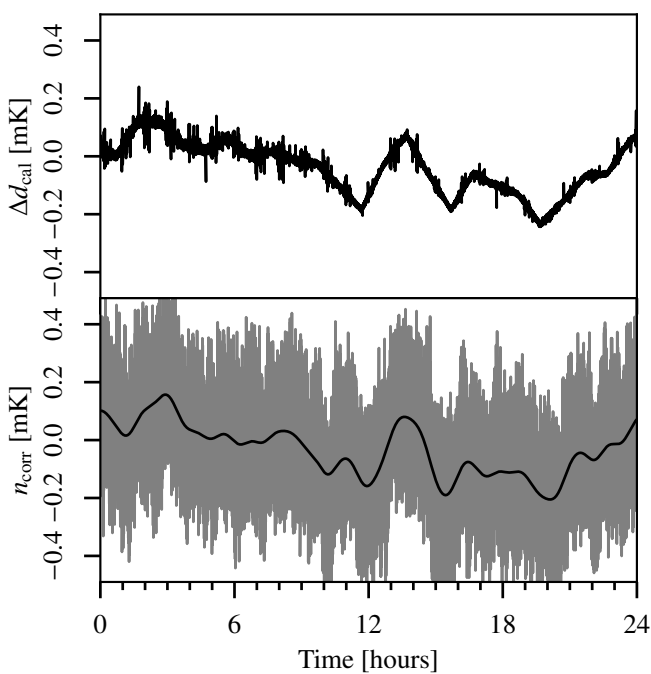


**Fig. 6.** (top): Difference between the COSMOGLOBE  $d_{\text{cal}} = d/g - b - s_{\text{sl}}$  and the delivered calibrated TOD from WMAP. (Bottom): Raw correlated noise (gray) and smoothed data with Gaussian kernel (black). This shows more clearly the hourly baseline subtraction from the WMAP treatment.

2007; Watts et al. 2022). The uncertainty in  $x_{\text{im}}$  was quoted as the source of large-scale polarized features in the WMAP9 maps, and a template of this effect was explicitly projected out in the pixel-space polarized covariance matrix.

We find  $x_{\text{im}}$  values that are largely consistent with the values reported in Bennett et al. (2013), albeit with some outliers. We find in general that the 68 % confidence intervals from COSMOGLOBE are smaller than the fiducial values, although we caution against a direct comparison of these values since such different procedures were used for estimating the uncertainties.

#### 4.4. Instrumental noise and goodness-of-fit

The noise fitting, as outlined in Sect. 2.7, inherently depends on the data being fit well by both the sky model and the instrument model. In practice, correlated noise fitting can model any unmodeled signals, so the power spectrum and TODs must be carefully scrutinized before any conclusions can be made about the corresponding maps.

The white noise level in raw  $du$  is not strictly sampled, but is estimated conditioned on the instrumental parameters and the sky parameters. However, the calibrated white noise level  $\sigma_0[\text{K}] = \sigma_0[du]/g$  does depend on the gain quite directly, which allows us to test the effects of the calibration on the instrument sensitivity itself. The calibrated white noise level follows a biaural trend indicative of a system temperature variation, which is to be expected given the radiometer equation

$$\sigma_0[\text{V}] \propto gT_{\text{sys}}. \quad (56)$$

Aside from an overall amplitude shift due to the absolute calibration variation, the shape of the white noise level is stable throughout the Gibbs chain.

The knee frequencies for each channel lie between the reported values in Jarosik et al. (2003a) for both the Goddard Space Flight Center (GSFC) laboratory measurements and those from the first year of data collection. Nearly all radiometers have constant  $f_{\text{knee}}$  throughout the mission, with a few notable exceptions. First, all  $W$ -band channels display some amount of temporal variation that does not seem to be associated with any sinusoidal features. Second, all  $Q2$  channels, V223, and V224 all display a similar asymptotic drift in time. We have not found any instrumental effects that share this feature. The PSD slope  $\alpha$  is around  $-1$  for each radiometer, albeit with high scatter for the lower frequencies. As expected, the uncertainty in  $\alpha$  decreases as  $f_{\text{knee}}$  increases, since there are more datapoints to fit below  $f_{\text{knee}}$  where the constraining power on  $\alpha$  is the strongest.

The most striking feature of the reduced normalized  $\chi^2$  is its amplitude and its semiannual periodicity. Given the noise model and data residual, we can evaluate the goodness-of-fit in the form of the relative  $\chi^2$ . Here, we find that approximately half of the radiometers have a  $\chi^2$  value at least  $6\sigma$  above or below the expected value. Given perfect Gaussian residuals, we would expect the reduced sum of squares to be  $n_{\text{TOD}} = 2^N$  and be within  $\sqrt{2n_{\text{TOD}}} = 2^{(N+1)/2}$  68 % of the time. For a typical  $W$ -band scan of length  $n_{\text{TOD}} = 2^{22}$ , a  $10\sigma$  model failure corresponds to  $\chi^2/n_{\text{TOD}} = 1.003$ . Therefore, it is exceedingly difficult to look at any given WMAP scan in the time domain and identify a model failure. In power spectrum space, i.e., in Fig. 7, the data are still characterized well at all scales, despite this scan having a  $\chi^2$  that is  $7\sigma$  above the expectation value.

Only with aggressive smoothing, as in Fig. 8, does the model failure become apparent at frequencies 1–10 Hz. Here, it is clear that despite fitting the data well at the highest and lowest frequencies, it is in the intermediate range of 1–5 Hz where the  $1/f$  model is a less accurate fit to the residual power spectrum. Part of the cause of this failure is that the white noise level is essentially fixed by the value of the power spectrum at the Nyquist frequency, as it was computed by differencing adjacent samples. The power spectrum has a downward trend beyond above 1 Hz, indicating that the data would be better fit by one or more terms proportional to  $f^\alpha$ . This is phenomenologically similar to the WMAP collaboration’s approach of describing the time-space autocorrelation as a cubic polynomial in  $\log \Delta t$  (Jarosik et al. 2007).

In practice, the  $1/f$  model has a small effect on the final data products, and was not visible in noise models when we modeled the data in one day scans rather than the longer 3–7 day scans due to the lower  $n_{\text{TOD}}$  giving a higher uncertainty on the relative  $\chi^2$ . Therefore, although this strictly constitutes a deficiency in the model, it is in practice too small to affect the results of the rest of the chain. The downturn of the noise PSD at high frequencies is also present in, e.g., the Planck HFI data (Planck Collaboration Int. XLVI 2016, Fig. 1), so improved modeling of this form will be a necessity in future COSMOGLOBE endeavors, and will be used to improve the WMAP data processing.

## 5. Frequency maps

In this section, we present the reprocessed WMAP frequency maps and their properties. In Sect 5.1 we present the reprocessed WMAP maps themselves, commenting on notable features. Section 5.2 compares the properties of the individual DAs with the published WMAP9 results, while Sect. 5.3 focuses on the internal consistency between the WMAP channels themselves. Finally, we assess the consistency between the LFI channels and WMAP in Sect. 5.4 and compare with legacy results.

**Table 3.** Summary of noise properties.

Radiometer ..	Diode	Sensitivity, $\sigma_0$ (mK $\sqrt{s}$ )			Knee frequency, $f_{\text{knee}}$ (mHz)			Slope, $\alpha$
		GSFC	WMAP	CG / $\sqrt{2}$	GSFC	WMAP	CG / $\sqrt{2}$	
K11 .....	1	0.72	0.66	$0.704 \pm 0.002$	6.13	0.4	$0.82 \pm 0.20$	$-1.01 \pm 0.10$
	2			$0.708 \pm 0.003$			$0.63 \pm 0.14$	$-0.95 \pm 0.10$
K12 .....	1	0.87	0.75	$0.796 \pm 0.004$	5.37	0.51	$0.42 \pm 0.19$	$-0.93 \pm 0.12$
	2			$0.780 \pm 0.005$			$0.71 \pm 0.15$	$-1.02 \pm 0.10$
Ka11 .....	1	0.75	0.71	$0.788 \pm 0.001$	1.66	0.71	$1.20 \pm 0.22$	$-1.02 \pm 0.09$
	2			$0.777 \pm 0.001$			$1.19 \pm 0.22$	$-1.02 \pm 0.09$
Ka12 .....	1	0.77	0.72	$0.788 \pm 0.003$	1.29	0.32	$0.62 \pm 0.16$	$-0.99 \pm 0.11$
	2			$0.784 \pm 0.001$			$0.63 \pm 0.13$	$-1.01 \pm 0.11$
Q11 .....	1	0.99	0.92	$0.998 \pm 0.002$	3.21	1.09	$1.06 \pm 0.16$	$-1.09 \pm 0.09$
	2			$0.992 \pm 0.002$			$1.06 \pm 0.16$	$-1.10 \pm 0.09$
Q12 .....	1	0.95	1.02	$1.159 \pm 0.007$	3.13	0.35	$0.45 \pm 0.47$	$-0.98 \pm 0.11$
	2			$1.146 \pm 0.007$			$0.83 \pm 0.14$	$-1.00 \pm 0.09$
Q21 .....	1	0.89	0.85	$0.908 \pm 0.002$	1.92	5.76	$2.88 \pm 0.37$	$-1.10 \pm 0.07$
	2			$0.906 \pm 0.002$			$3.22 \pm 0.56$	$-1.10 \pm 0.06$
Q22 .....	1	1.04	0.99	$1.074 \pm 0.004$	4.61	8.62	$3.95 \pm 0.54$	$-1.11 \pm 0.06$
	2			$1.064 \pm 0.003$			$4.05 \pm 0.64$	$-1.11 \pm 0.06$
V11 .....	1	1.25	1.22	$1.551 \pm 0.003$	2.56	0.09	$1.27 \pm 0.15$	$-0.90 \pm 0.06$
	2			$1.539 \pm 0.003$			$1.19 \pm 0.14$	$-0.89 \pm 0.06$
V12 .....	1	1.07	1.11	$1.398 \pm 0.002$	4.49	1.41	$2.11 \pm 0.20$	$-0.97 \pm 0.05$
	2			$1.432 \pm 0.002$			$1.88 \pm 0.17$	$-0.96 \pm 0.05$
V21 .....	1	1.01	0.97	$1.241 \pm 0.298$	2.43	0.88	$1.50 \pm 0.24$	$-0.95 \pm 0.07$
	2			$1.217 \pm 0.294$			$1.60 \pm 0.26$	$-0.97 \pm 0.06$
V22 .....	1	1.13	1.1	$1.443 \pm 0.300$	3.06	8.35	$4.01 \pm 0.85$	$-1.00 \pm 0.08$
	2			$1.415 \pm 0.316$			$3.08 \pm 0.65$	$-1.01 \pm 0.08$
W11 .....	1	1.18	1.35	$1.938 \pm 0.005$	16.2	7.88	$5.59 \pm 0.53$	$-0.94 \pm 0.05$
	2			$1.895 \pm 0.005$			$8.99 \pm 0.85$	$-0.95 \pm 0.04$
W12 .....	1	1.41	1.61	$2.301 \pm 0.005$	15.1	0.66	$3.91 \pm 0.42$	$-0.89 \pm 0.05$
	2			$2.345 \pm 0.006$			$4.81 \pm 0.53$	$-0.89 \pm 0.05$
W21 .....	1	1.38	1.61	$2.225 \pm 0.007$	1.76	9.02	$13.57 \pm 1.47$	$-0.89 \pm 0.03$
	2			$2.292 \pm 0.006$			$5.06 \pm 0.95$	$-0.93 \pm 0.05$
W22 .....	1	1.44	1.72	$2.291 \pm 0.006$	0.77	7.47	$3.02 \pm 0.53$	$-0.98 \pm 0.05$
	2			$2.232 \pm 0.007$			$7.26 \pm 1.05$	$-0.95 \pm 0.04$
W31 .....	1	1.47	1.65	$2.328 \pm 0.005$	1.84	0.93	$1.30 \pm 0.46$	$-0.99 \pm 0.07$
	2			$2.322 \pm 0.006$			$1.97 \pm 0.28$	$-0.98 \pm 0.06$
W32 .....	1	1.69	1.86	$2.707 \pm 0.015$	2.39	0.28	$1.59 \pm 0.29$	$-0.98 \pm 0.07$
	2			$2.579 \pm 0.015$			$1.40 \pm 0.39$	$-1.00 \pm 0.07$
W41 .....	1	1.6	1.71	$2.519 \pm 0.010$	8.46	46.5	$26.81 \pm 1.83$	$-0.92 \pm 0.04$
	2			$2.479 \pm 0.009$			$24.75 \pm 1.63$	$-0.92 \pm 0.04$
W42 .....	1	1.43	1.65	$2.221 \pm 0.017$	5.31	26.0	$16.10 \pm 1.09$	$-0.94 \pm 0.04$
	2			$2.202 \pm 0.015$			$17.11 \pm 1.19$	$-0.94 \pm 0.04$

### 5.1. Map summary statistics

For each DA, we present the mean maps, the white noise contribution in the form of RMS maps, and the standard deviation of the maps accounting for the sampling of instrumental parameters. Each mean map retains the Solar dipole, which we will estimate separately in Sect. 6.1.1. Additionally, we present inverse-weighted mean maps of  $Q$ ,  $V$ , and  $W$  rather than displaying each individual DA.

The  $K$ -band,  $Ka$ -band,  $Q$ -band,  $V$ -band, and  $W$ -band mean maps are presented in Figs. 9, 10, 11, 12, and 13, respectively, given in  $\mu\text{K}_{\text{CMB}}$  units. The  $Q$ ,  $V$ , and  $W$ -band maps are generated by inverse-variance weighting the individual DAs. The temperature maps are presented at full resolution, while the polarization maps have been smoothed with a  $2^\circ$  Gaussian beam. The maps in temperature behave as expected, with consistent Solar dipole and Galactic foreground emission decreasing as the frequency increases. Similarly, the polarized maps decrease from  $K$ - $V$ -band following the expected synchrotron behavior, with a slight increase at  $W$ -band due to the contribution of thermal

dust. Most striking, especially when compared with the delivered  $WMAP9$  maps, is the lack of transmission imbalance modes or poorly measured modes in the polarized maps.

The RMS maps are computed during the mapmaking routine, adding  $\sigma_{0,i}^{-2}$  for every timestep that horn is in a given pixel, appropriately scaled by polarization angle and imbalance parameters. The top row of Fig. 14 shows the white noise for the Stokes parameters and the correlation coefficient between Stokes  $Q$  and  $U$ . The white noise pattern for  $T$  follows the usual pattern with highest sensitivity at the North and South ecliptic poles, as well as circles around the poles corresponding to times when the partner horn is observing the opposite ecliptic pole. There are also regions of higher noise level corresponding to planets crossing the ecliptic, and regions of higher emission  $\simeq 140^\circ$  away from the Galactic center, which correspond to the times when the partner horn lies within the processing mask.

The polarized RMS maps share all of these characteristics, but with an overall amplitude shift due to polarization measurements having half the effective number of observations per pixel.

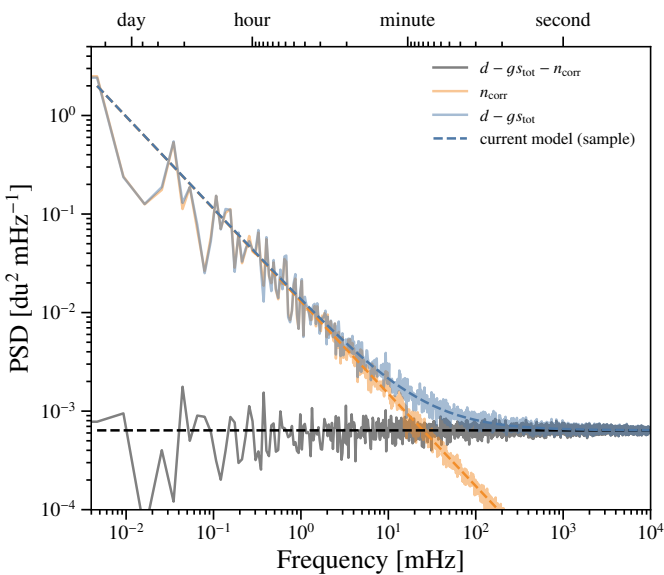


**Fig. 7.** PSD for radiometer W413 that spans MJDs 52252.3–52254.8. The power spectrum of the blue line corresponds to the residual, while the gray line is the residual with a correlated noise realization removed.

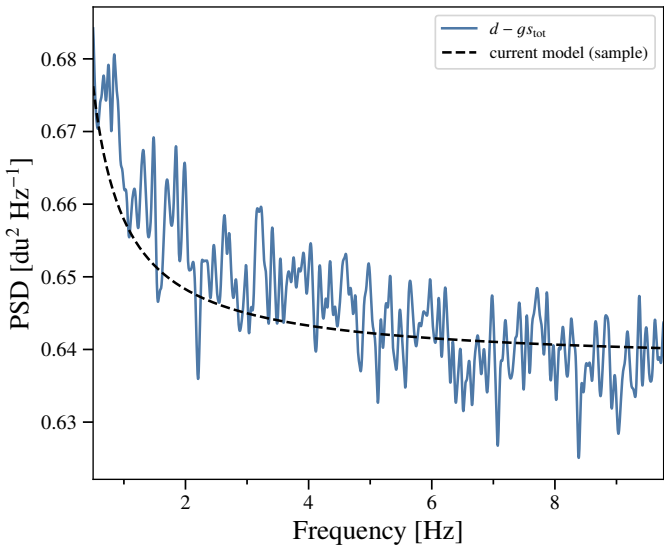


**Fig. 8.** PSD for radiometer W413 that spans MJDs 52252.3–52254.8. The black dashed line is a sample of the theoretical PSD, while the blue line is the smoothed residual power spectrum.

In addition, the poles have a characteristic “X”-like structure that is rotated 45° degrees between  $Q$  and  $U$ , corresponding to different polarization orientations. There are also characteristic large scale structures visible in Galactic coordinates, corresponding to polarization modes poorly constrained by the WMAP scan strategy.

While the maps in the top row of Fig. 14 are directly comparable to the WMAP9 products, the bottom row shows a unique product, the standard deviation and  $QU$  correlation of the output chain maps. These maps can be considered the “systematic” error contributions, as their variation depends on the sampled instrumental parameters, i.e., gain, imbalance parameters, correlated noise, and sidelobe correction. The temperature map contains a clear quadrupole signature. This is due to the variation in the absolute calibration  $g_0$ , which changes the Solar dipole in

the final map. In addition to the quadrupole, the Galactic plane also varies due to the gain solution being varied. As expected, the white noise patterns associated with the scan strategy also appear in the polarization maps, and become more clear in the temperature maps for the higher frequency DAs (Fig. B.3). As these maps only include 490 total samples out of full 500-sample Gibbs chain, they will be superseded by a larger future chain. While the quantitative solution will change, it is unlikely that the final maps will differ qualitatively from those presented here.

An additional useful term to consider is the difference between two arbitrary samples, which we show in Fig. 15. In temperature, the most clear term is a dipole corresponding to the absolute gain difference and the Galactic plane. There are also additional small lines associated with the scanning strategy, which correspond to different correlated noise realizations. In polarization, correlated noise is the dominant difference between two samples, with a small imprint of the Galactic plane due to relative gain variation. The polarization differences are aligned with WMAP’s scans, modulated by the polarization angle.

We also consider the spatial structure of the TOD corrections in pixel space, as shown in Fig. 16. This corresponds to the TOD objects in Fig. 1 binned into Stokes  $I$ ,  $Q$ , and  $U$  maps. Note that the dynamic range of each of these figures varies by two orders of magnitude, indicating that some components must be subtracted more carefully than others. However, the amplitude of the signal is not proportional to the level of scrutiny necessary, as some, such as orbital dipole, are much more precisely known than the others.

The variation of these TOD corrections is more important than the absolute amplitude. As shown in Fig. 17, white noise is the dominant effect for  $\ell \gtrsim 100$  for all frequencies. For temperature, the low-multipole variation in the orbital dipole signal and far sidelobe corrections are the largest source of fluctuations and low multipoles, but remain orders of magnitude below the average signal. These fluctuations are directly related to absolute calibration uncertainty, and provide a practical limit to the magnitude gain effects the temperature signal. For the  $C_\ell^{EE}$  and  $C_\ell^{BB}$  spectra, the relative amplitude of the fluctuations are band-dependent. For example, bandpass leakage and orbital dipole corrections are the dominant effect, while for  $Q$ -band, the correlated noise realizations contribute the most variation. In general, we find that for large angular scale polarization, modelling uncertainties in the form of gain and sidelobe estimation have a comparable effect to white noise and correlated noise estimates.

As a final inspection of the COSMOGLOBE map products, we take the angular power spectra of the maps themselves and compare with the WMAP9 results in Fig. 18. To compute the power spectrum, we mask the data using the extended temperature analysis mask which allows a sky fraction of 68.8 % and obtain the pseudo- $C_\ell$  power spectra using the NaMaster (Alonso et al. 2019)<sup>7</sup> `compute_full_master` routine, returning a set of decoupled bandpowers.

As the temperature power spectra are signal-dominated up to  $\ell \sim 200$  for all DAs, it is more useful to look at the ratio of spectra in the left column of Fig. 18. Here we see that the spectra are consistent with each other at all but the very largest and smallest scales. The largest scale differences are due to mode-coupling effects – the WMAP9 maps were produced by removing the Solar dipole in the timestream before mapmaking, while the COSMOGLOBE maps needed a dipole estimate to be removed as a post-processing step. The small scale differences above  $\ell \sim 200$  can be attributed to the white noise treatment. In particular, the

<sup>7</sup> <https://github.com/LSSTDESC/NaMaster>



**Fig. 9.**  $K$ -band

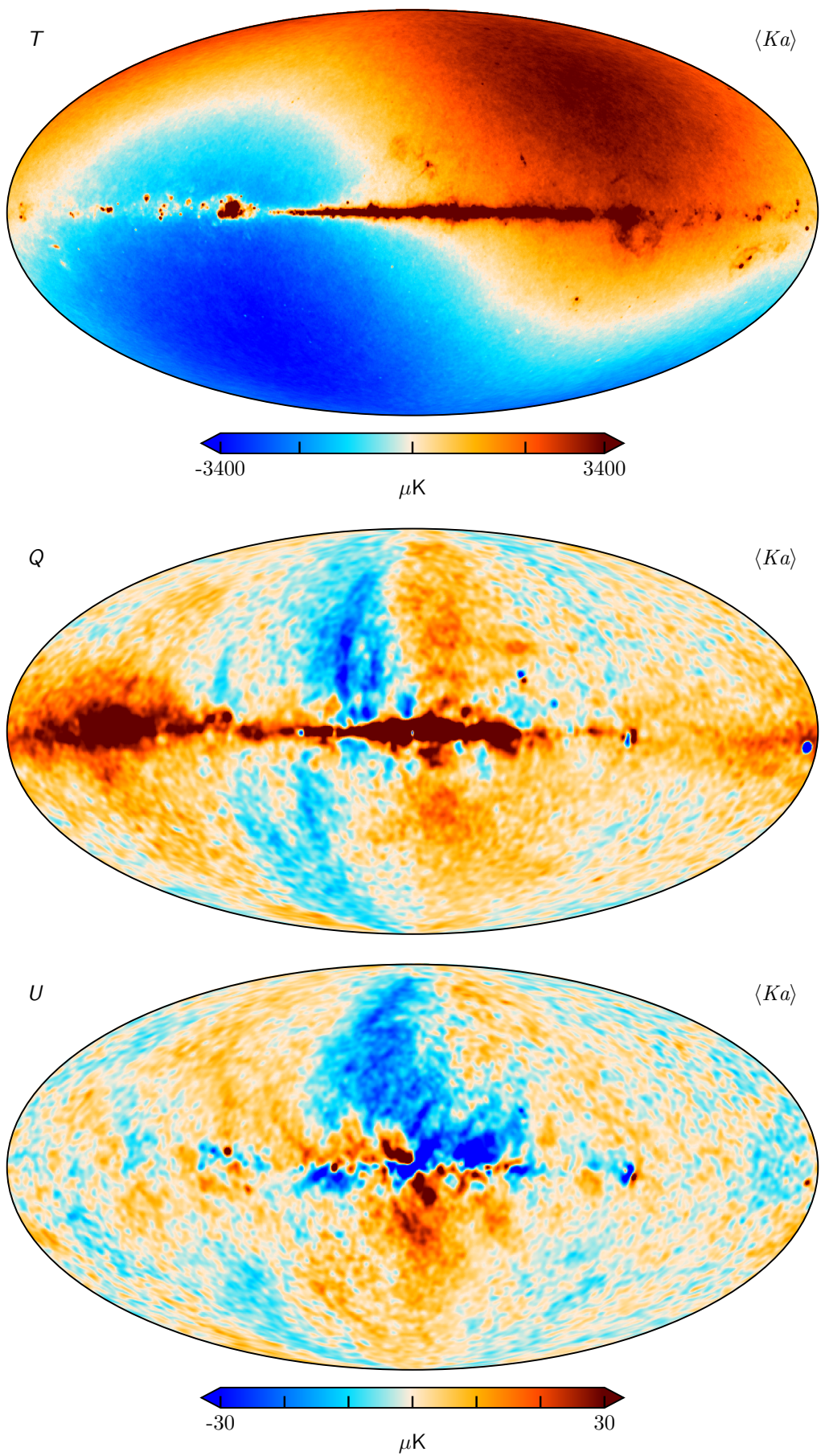


**Fig. 10.**  $Ka$ -band

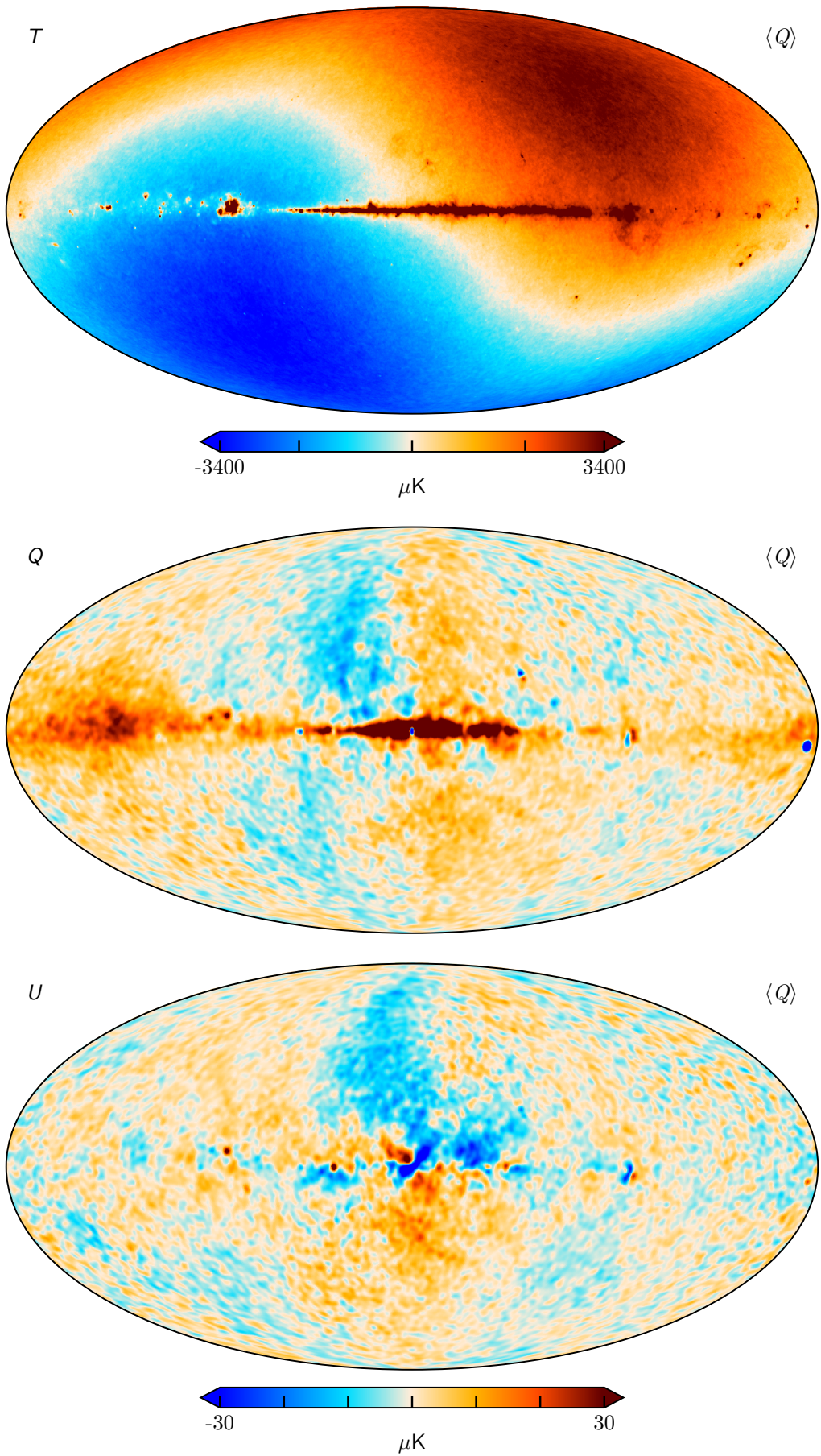


**Fig. 11.**  $Q$ -band



**Fig. 12.**  $V$ -band

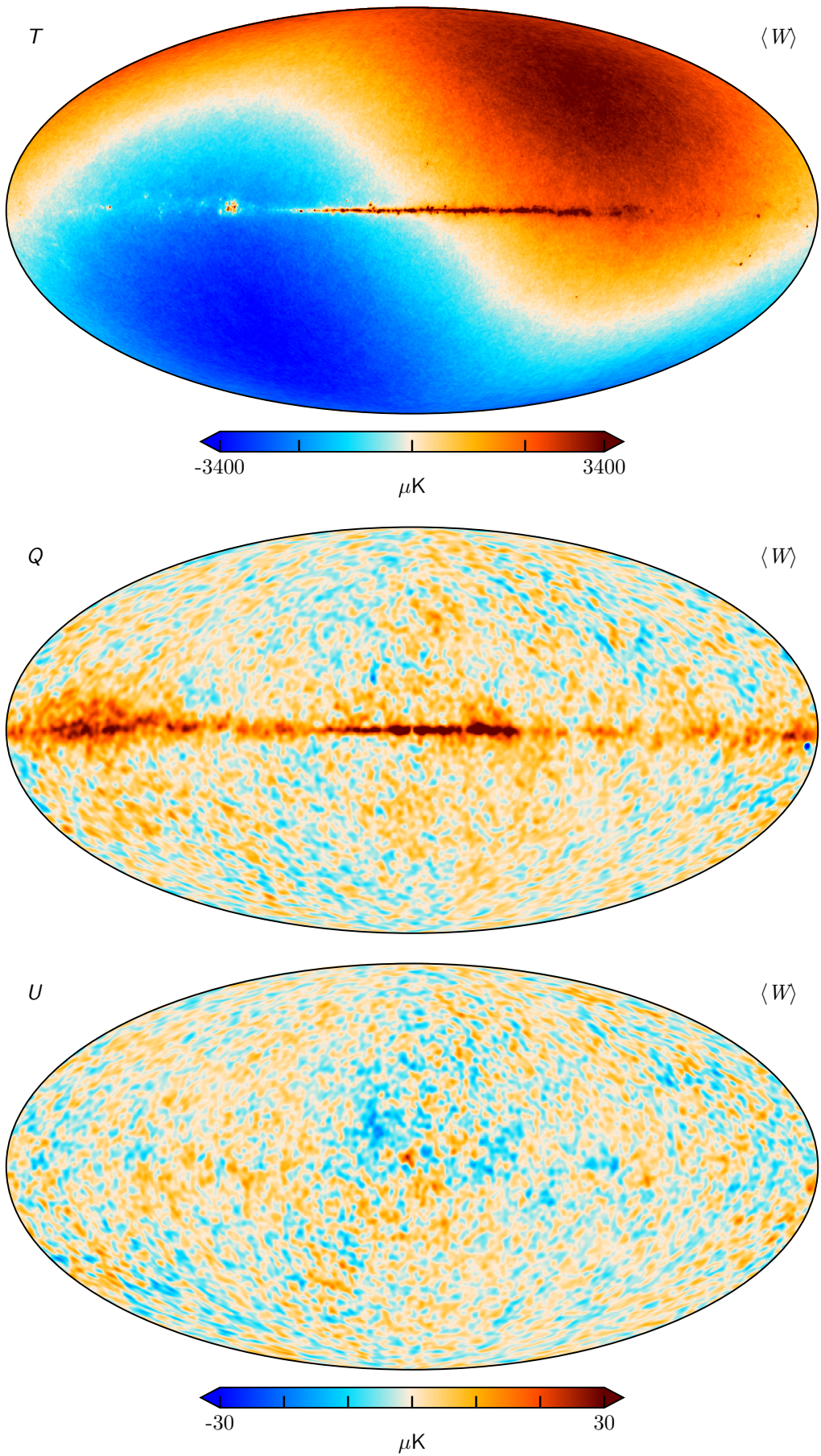


**Fig. 13.** W-band

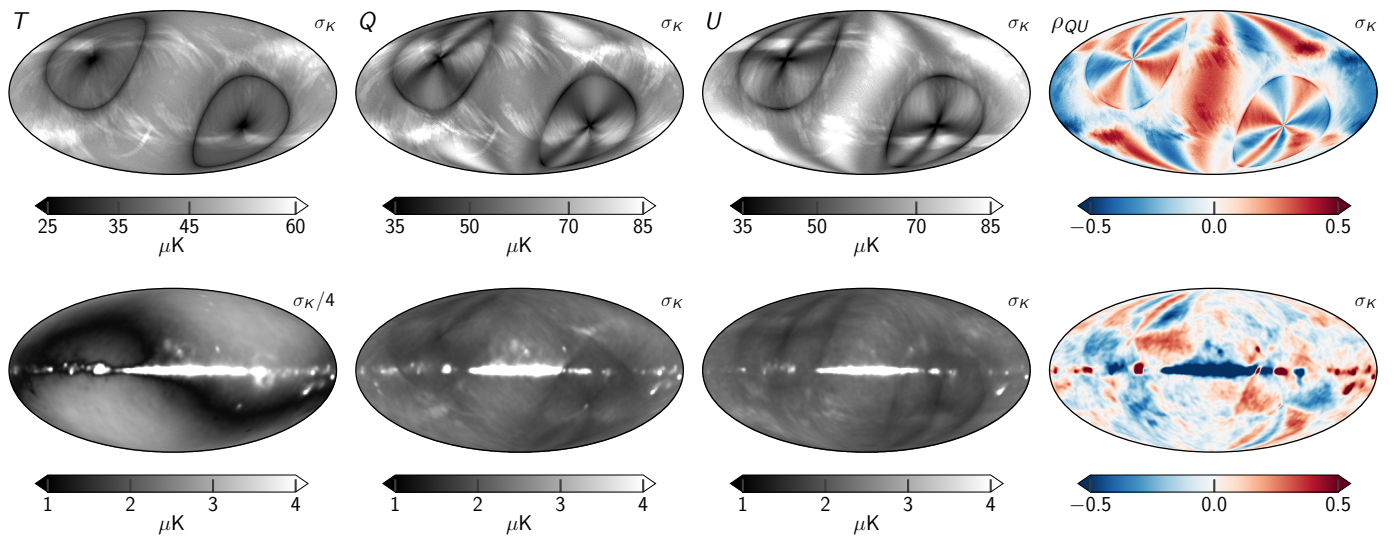


**Fig. 14.** Posterior variation maps for  $K$ -band. Columns show the Stokes parameters and the correlation coefficient between  $Q$  and  $U$ , while the rows show (top) the white noise rms per pixel and (bottom) the posterior standard deviation. The rms maps are unsmoothed, while the standard deviations have been smoothed to  $7^\circ$ .

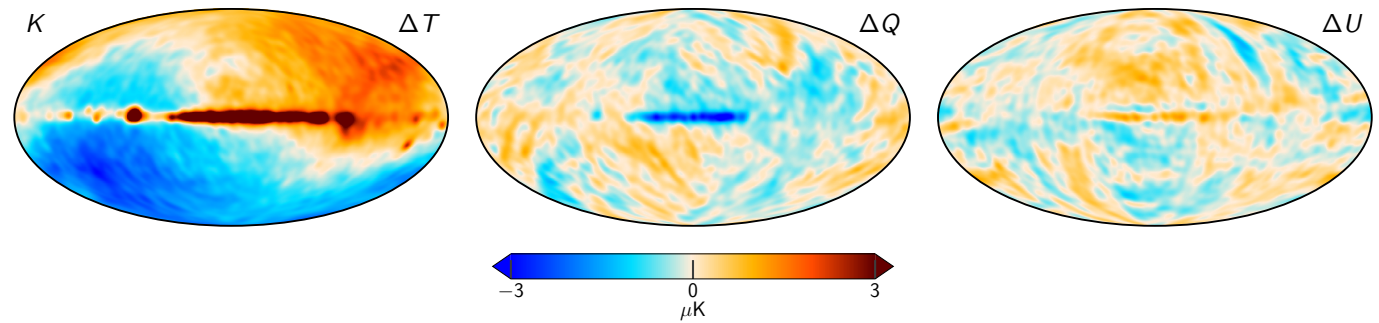


**Fig. 15.** Difference between two  $K$ -band Gibbs samples, smoothed to  $7^\circ$ .

WMAP9 processing gain solution varies every 23 s compared to the COSMOGLOBE solution which uses constant gain per scan. Conversely, the COSMOGLOBE radiometer noise estimate varies per scan, whereas there is no mention of raw instrumental noise variation with time in the WMAP suite of papers.

The  $E$ -mode power spectra, displayed in the second column of Fig. 18, are mainly dominated by noise and polarized synchrotron emission. As expected, the large scale foreground-dominated multipoles decrease in amplitude according to the relative amplitude of the synchrotron spectrum. Aside from the  $\ell = 8$   $W2$  multipole, the COSMOGLOBE power spectra are well-behaved across all bands. The large fluctuations in the WMAP power spectrum, in particular  $W2$  and  $W4$ , are almost completely gone in the COSMOGLOBE analysis.

The  $B$ -mode power spectra, displayed in the third column of Fig. 18, should follow the same pattern as in the  $E$ -modes, but with foregrounds reduced by a factor of  $\approx 2$  (Bennett et al. 2013). Indeed, with the notable exception of the  $Ka$  and  $Q1$   $\ell = 3$  multipoles and the  $W3$   $\ell = 7$  multipole, this pattern is largely borne out, with nearly white noise across all angular scales. The  $C_{\ell=3}^{BB}$  mode has been identified as being poorly measured by, e.g., Jarosik et al. (2011), due to its symmetry aligning with  $\gtrsim 10$  min signals in the TOD induced by the WMAP scan strategy.

In general, we find that the reprocessed WMAP maps produced in the COSMOGLOBE framework have map and power spectrum properties that contain traces of the WMAP observation

strategy than the WMAP9 products. To fully assess the quality of these frequency maps compared to the official WMAP9 products, we compare the maps explicitly in Sect. 5.2.

## 5.2. Comparison with 9-year WMAP maps

We present difference maps between the official 9-year WMAP maps and the maps produced in this work in Fig. 19. This figure shows a total of fifteen difference maps, one for each of the main WMAP bands ( $K$ ,  $Ka$ ,  $Q$ ,  $V$ , and  $W$ ), in the three Stokes parameters.

The differences are overall quite small, as the data processing between COSMOGLOBE and WMAP9 are quite similar, with subtle differences as described in Sec. 3. In total intensity, we see good agreement with the full WMAP9 results, with deviations at the few  $\mu\text{K}$  level. The largest difference between the two analyses is shown in the  $K$ -band difference map, which demonstrates the difference between the band calibration as described in Secs. 4.2 and 8.3. This can be attributed to the absolute calibration differences between the two pipelines. In particular, Bennett et al. (2013) estimates a calibration uncertainty of 0.2 % across all bands, corresponding to a  $\sim 7 \mu\text{K}$  variation in the Solar dipole amplitude. On the other hand, the COSMOGLOBE absolute calibration prior width of 0.002 can induce a  $6 \mu\text{K}$  Solar dipole residual. Therefore, a dipole difference such as this is not unexpected. In bands  $Ka-W$ , the absolute calibration is driven wholly by the

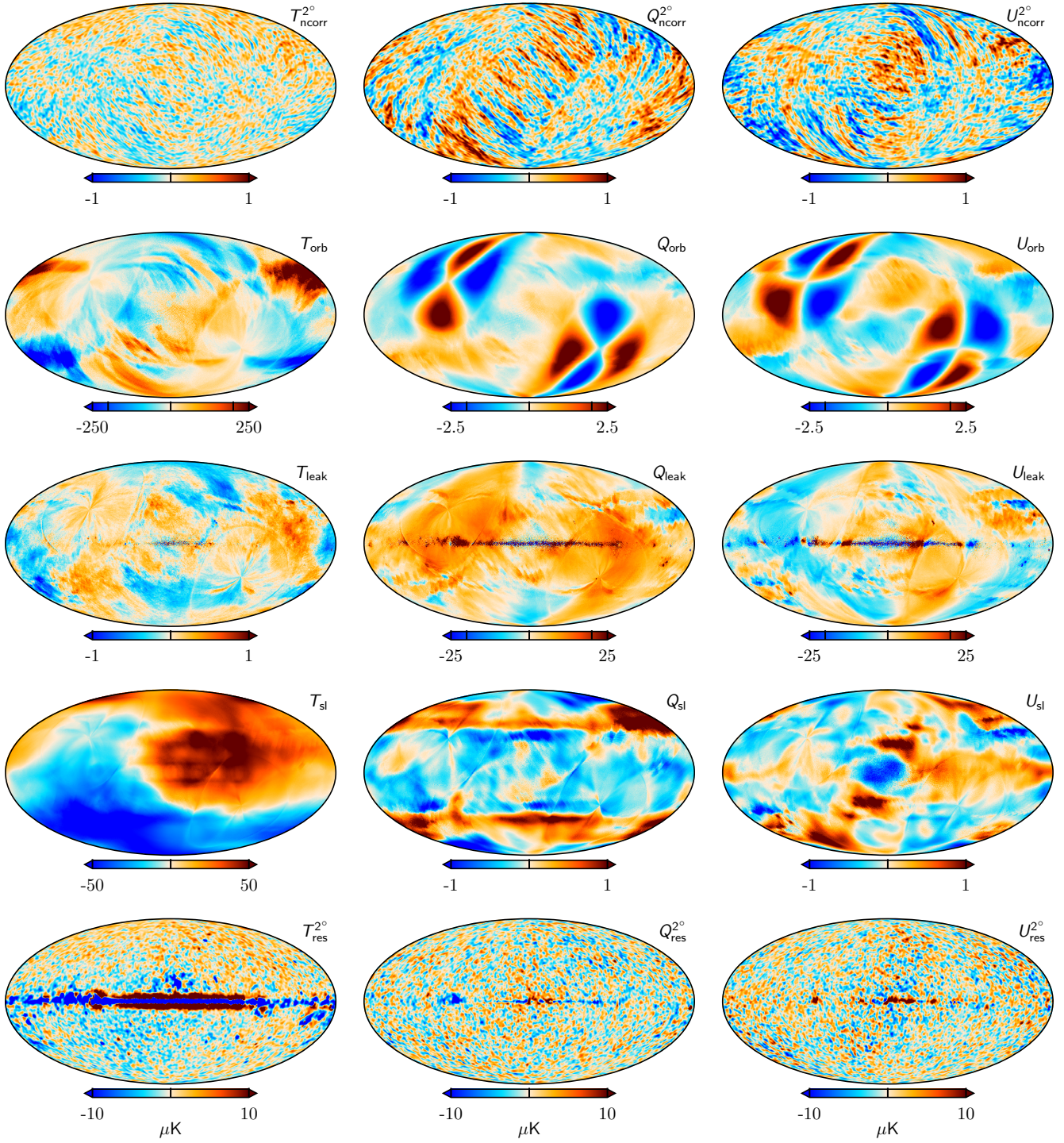
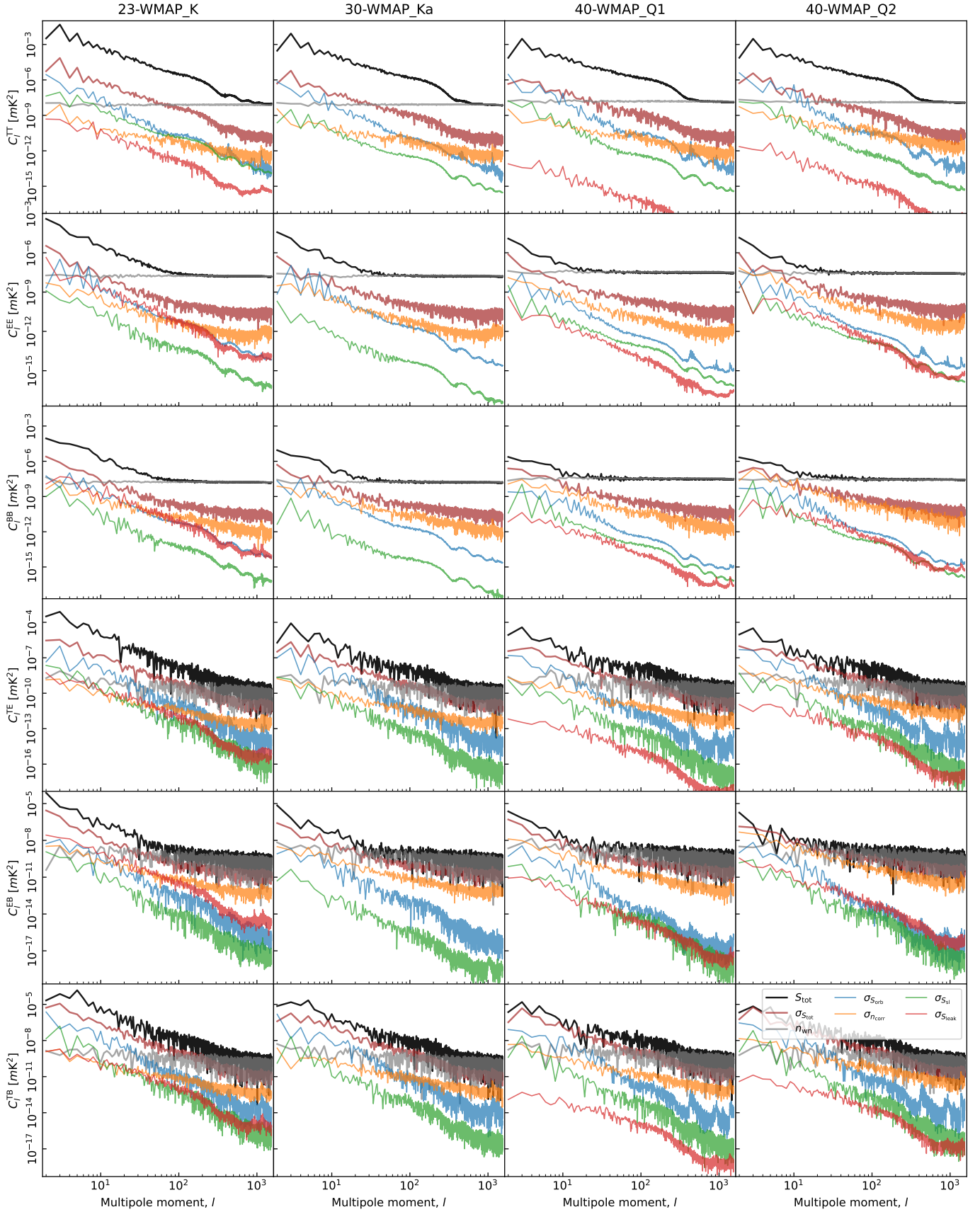


**Fig. 16.** TOD corrections for  $K$ -band for a single Gibbs sample, projected into maps. Columns show Stokes  $T$ ,  $Q$ , and  $U$  parameters. Rows show, from top to bottom, 1) correlated noise; 2) the orbital dipole; 3) bandpass mismatch leakage; and 4) sidelobe corrections. The bottom row shows the residual obtained when binning the sky and systematics-subtracted TOD into a sky map. Note that the correlated noise and residual have been smoothed by a  $2^\circ$  Gaussian beam.

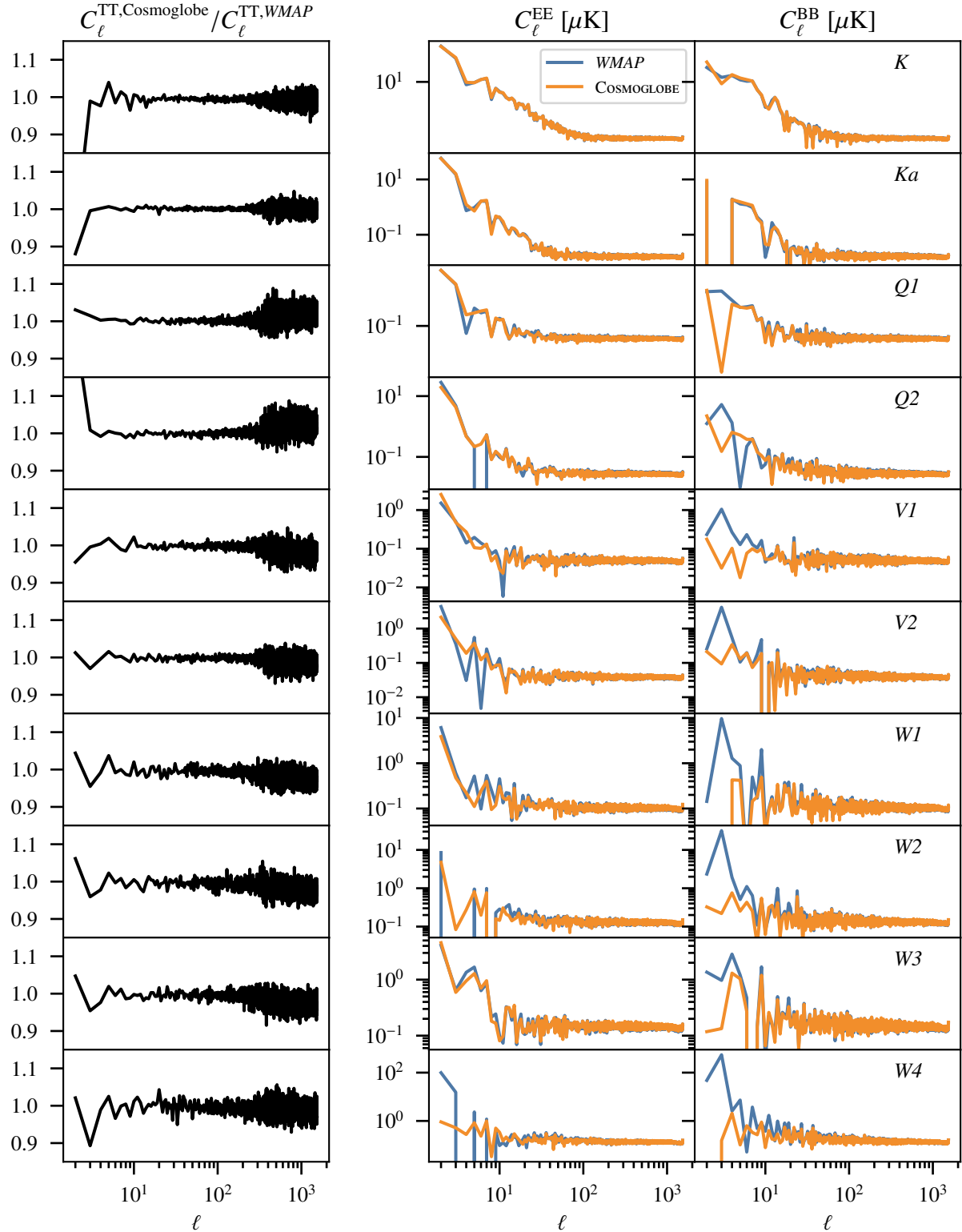
sampling algorithms described in Sect. 2.7.1, and as such is much more susceptible to poor modeling of the data. The fact then that the dipole amplitude in the difference maps is so small is strong evidence that the parametric modeling of the absolute calibration performance is comparable to the  $WMAP9$  approach of modelling the gain using on-board thermistors.

In the  $V$  and  $W$ -band temperature maps, there is an additional quadrupole signal closely aligned with the Solar dipole.

As noted in Larson et al. (2015), the  $WMAP9$  maps retain the kinematic quadrupole, whereas Commander3 removes this component. While kinematic quadrupole has the expected shape, the frequency dependence is not consistent with the expected functional form  $x \coth x$  where  $x = h\nu/(2kT_{CMB})$  (Notari & Quartin 2015). It is therefore likely that the quadrupole difference comes from some second-order effects in the time variation of the gain.



**Fig. 17.** Pseudo-spectrum standard deviation for each instrumental systematic correction shown in Fig. 16 (thin colored lines). For comparison, thick black lines show spectra for the full coadded frequency map; thick red lines show the standard deviation of the same (i.e., the full systematic uncertainty); gray lines show white noise realizations; and black lines show the power spectra of the maps themselves. Columns show results for  $K$ ,  $Ka$ ,  $Q1$ , and  $Q2$ , respectively, while rows show results for each of the six polarization states ( $TT$ ,  $EE$ ,  $BB$ ,  $TE$ ,  $TB$ , and  $EB$ ). All spectra have been derived outside the CMB confidence mask presented by [Andersen et al. \(2022\)](#) using the HEALPix `anafast` utility, correcting only for sky fraction and not for mask mode coupling.

**Fig. 18.** TT, EE, and BB specs

There is indeed an oscillatory structure in the relative difference between the gain solutions, which can be most seen in Fig. A.4.

In polarization, we note large scale differences in both Stokes  $Q$  and  $U$ . These large scale differences do not match known Galactic component morphologies. All of these differences are well-described by linear combinations of the poorly measured modes, though the map-space morphologies are not identical.

These large mode differences are due to three main effects: 1) poor polarization angle coverage for a few large-scale modes; 2) errors in transmission imbalance coupled with the Solar dipole; and 3) interplay between the transmission imbalance, the far sidelobe, and the Solar dipole, as briefly described in Sec. 2.2. The scale of these effect is most pronounced in the  $W$ -band po-

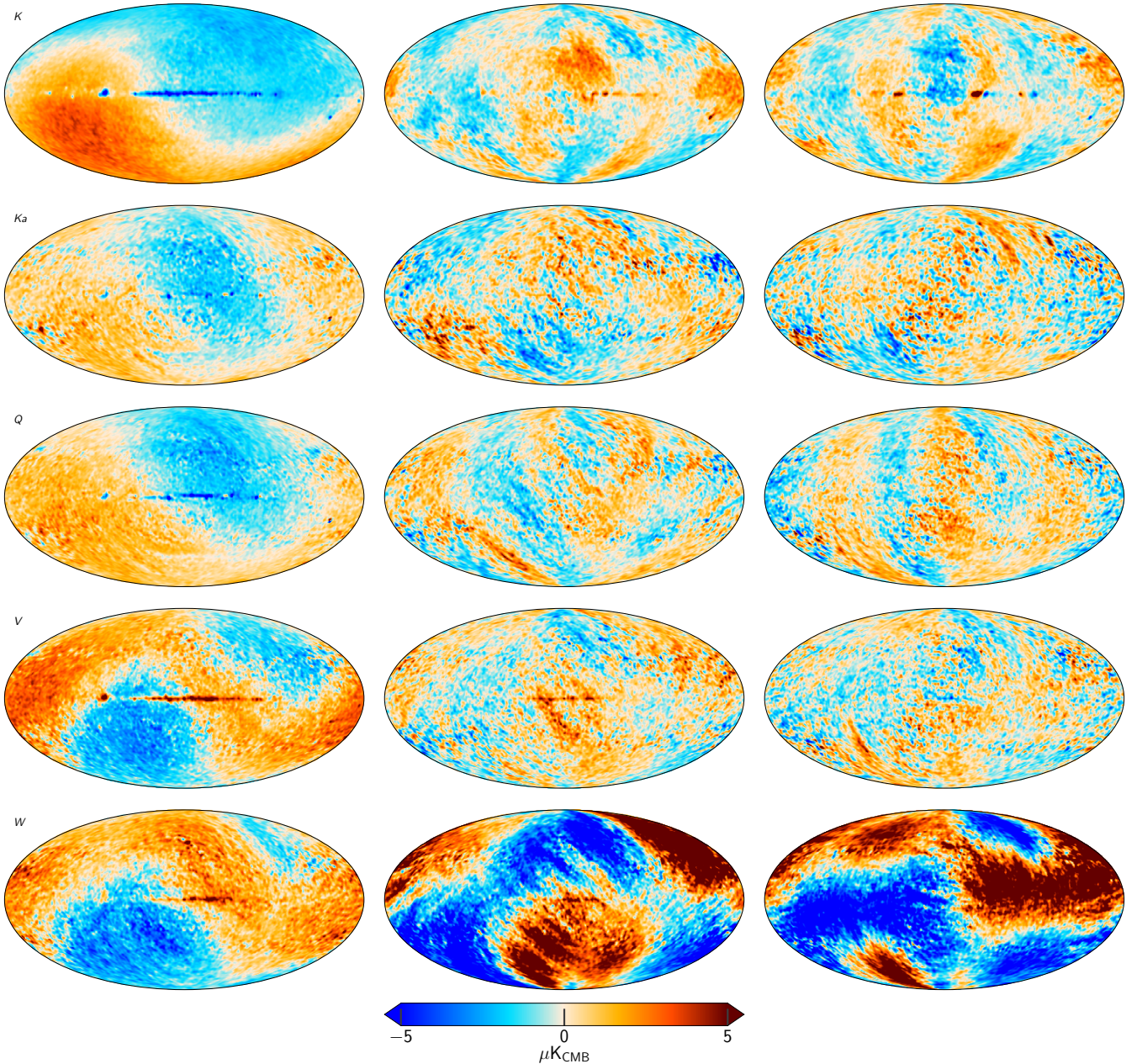


**Fig. 19.** Difference maps between the COSMOGLOBE and 9-year WMAP frequency maps. Columns show Stokes  $T$ ,  $Q$ , and  $U$  parameter maps, while rows show  $K$ -,  $Ka$ -,  $Q$ -,  $V$ -, and  $W$ -band maps. The maps are all smoothed with a  $2^\circ$  FWHM Gaussian beam.

larization results, where we see the largest differences between the two processing pipelines.

**Table 4.** Difference map  $\chi^2$  statistics.

DIFFERENCE	$\chi^2_{\text{uncorr}}$	$\chi^2_{\text{corr}}$	$\Delta\chi^2$
$0.32 \times K1 - Ka1 \dots$	4291	4287	4
$Q1 - Q2 \dots \dots$	4500	4380	120
$V1 - V2 \dots \dots$	4490	4429	61
$W1 - W2 \dots \dots$	4328	4270	68
$W3 - W4 \dots \dots$	4257	4145	112

This truly demonstrates the benefit of jointly processing these two experiments simultaneously in the same framework. The differences shown in Fig. 19, particularly in polarization, are due to unmodeled systematics in the 9-year WMAP maps. If these large scale modes, which are not Galactic in origin, were in the maps produced in this work, these modes would either be clearly present in Galactic component maps, or in the component separation residuals (Sec. 6, Fig. B.6) and they are present in neither.

### 5.3. Consistency within WMAP channels

An important test for how well the instrumental systematics are being modeled is by checking the agreement within each of the WMAP channels. As described in Sec. 2.2, the  $Q$ -,  $V$ -bands each

**Table 5.** Transmission imbalance template amplitudes for each *WMAP* radiometer as estimated by fitting the official templates to low-resolution difference maps between COSMOGLOBE and *WMAP*. The templates are provided in mK, and the template amplitudes are therefore dimensionless. The fourth column lists the relative decrease in standard deviation,  $\sqrt{\sigma_{\text{raw}}^2 - \sigma_{\text{corr}}^2}/\sigma_{\text{raw}}$ , after subtracting the best-fit templates in percent.

DA	$a_1$	$a_2$	$\Delta\sigma[\%]$
K1 .....	-27.5	-50.6	30
Ka1 .....	-1.4	-1.9	25
Q1 .....	-30.0	-71.6	11
Q2 .....	-7.1	-1.5	20
V1 .....	-32.8	-53.4	6
V2 .....	8.8	-4.1	16
W1 .....	-2.8	4.6	8
W2 .....	-6.9	-3.5	11
W3 .....	29.1	53.4	12
W4 .....	15.5	-6.8	52

had two DAs, and the *W*-band had four. Checking for discrepancies between each of the individual DA maps within the same frequency channel can highlight mismodeled systematics.

The difference maps between the *Q*-, *V*-, and *W*-band inter-channel maps for Stokes *T*, *Q*, and *U* are shown in Fig.(TBD). The most notable difference has to do with the Galactic plane, which should not be surprising as each DA within each frequency channel as a slightly different bandpass. Beyond this, we see a bunch of things that we can comment on when the figures are actually present.

Looks like, according to this tex document, that there will also be a paragraph or two about the half-difference maps and their spectra.

#### 5.4. Consistency between *WMAP* and *LFI*

Seeing as *WMAP* and *LFI* cover nearly identical frequency channels, it is vital to assess how well these two experiments agree with each other, as the sky they observe is the same. Inspecting comparisons of the two experiments' sky maps can help elucidate systematic differences between them. Figure 22 shows comparisons between the *WMAP K*- and *Ka*-bands and the *LFI* 30 GHz channel, between the *WMAP Q*-band and *LFI* 44 GHz, and finally between *WMAP V*-band and *LFI* 70 GHz. For demonstration, the sky maps produced in this work are compared against the official *WMAP9* and *BeyondPLANCK* maps.

Starting with the COSMOGLOBE maps, we see in the first and third columns of Fig. 22 that the magnitude of the differences are small in both Stokes *Q* and *U*. Overall, across all four frequency map comparisons we see small levels of variation, with structure contained to the Galactic plane. Notably, however, is a larger sky signal within the *Ka*-band – 30 GHz Stokes *Q* comparison. This will be commented on here by Duncan or HK as I don't know exactly what I should say. Deviations at high Galactic latitudes are low, demonstrating a robust ability to remove poorly measured modes from both experiments thanks to the joint processing.

Columns two and four of Fig. 22 show the differences between the official *WMAP9* and *BeyondPLANCK* LFI frequency maps. Similar to the COSMOGLOBE sky map comparisons, we see differences in the Galactic center, and to a lesser degree along the Galactic plane due to the slight differences in the frequency coverage. When comparing the official *WMAP* maps, particularly for *K*-band, we see structures sweeping across large an-

gular scales across the sky, likely due to some effect Duncan totally knows how to describe here in detail. These structures were noted within the BEYONDPLANCK project, particularly in the polarized component separation and large-scale polarized AME studies (Svalheim et al. 2022; Herman et al. 2022). We see that the magnitude of both the Galactic and non-Galactic differences decrease with frequency as the central frequencies approach the foreground minimum where calibration uncertainties are the lowest. All frequency channels in this comparison do show large-scale modes which are difficult to constrain without joint processing.

## 6. Preliminary astrophysical results

In this section, we present initial results for the astrophysical component separation temperature power spectra. The frequency coverage in this analysis is essentially the same as BEYONDPLANCK, with the notable addition of the high signal-to-noise *K*-band and the reprocessed *W*-band. As such, the results presented here are similar in quality to the results presented in *BeyondPlanck* (2022).

### 6.1. CMB results

Cosmological parameter estimation is left for future work, in large part because the two chains of length 250 are too short to reliably estimate cosmological parameters in this framework. For comparison, Paradiso et al. (2022) demonstrated that at least 2000 Gibbs samples were required before the reionization optical depth  $\tau$  value had converged. Similarly, for BEYONDPLANCK in the temperature case, the Gelman-Rubin statistic is just above  $R = 1.01$  for  $\ell \lesssim 600$  then continues to increase, indicating marginally acceptable convergence across all multipoles. Therefore, the results for the CMB presented here serve mainly as consistency checks. Given these caveats, we present preliminary CMB analysis in Sects. 6.1.1–6.1.3.

#### 6.1.1. Solar dipole

#### 6.1.2. Low- $\ell$ anomalies

Even though the CMB is well described by  $\Lambda$ CDM, there are several anomalies, especially at low multipoles, that seem to be in tension with  $\Lambda$ CDM.

It has been noted since COBE-DMR that the quadrupole amplitude of our CMB is lower than expected from  $\Lambda$ CDM (Bennett et al. 1992). This has later been confirmed in *WMAP* (Hinshaw et al. 2003) and *Planck* (Planck Collaboration Int. XV 2014), but with large discrepancies in mean value and error bars.

#### 6.1.3. Angular temperature power spectrum

### 6.2. Galactic foregrounds

As described in Sec. 2.4, we adopt a similar sky model to that of *BeyondPlanck* (2022). Explicitly, in this work the low frequency component (free-free, anomalous microwave, and synchrotron) emission amplitudes and their spectral parameters are fit in total intensity. The thermal dust amplitude is also fit here, though the addition of *Planck* 857 GHz provides most of the constraining power. The results for each of these foreground components are displayed in Fig. 32. Though the form of the AME model is different in this work, the morphologies of the components match well with those presented in Andersen et al. (2022). This

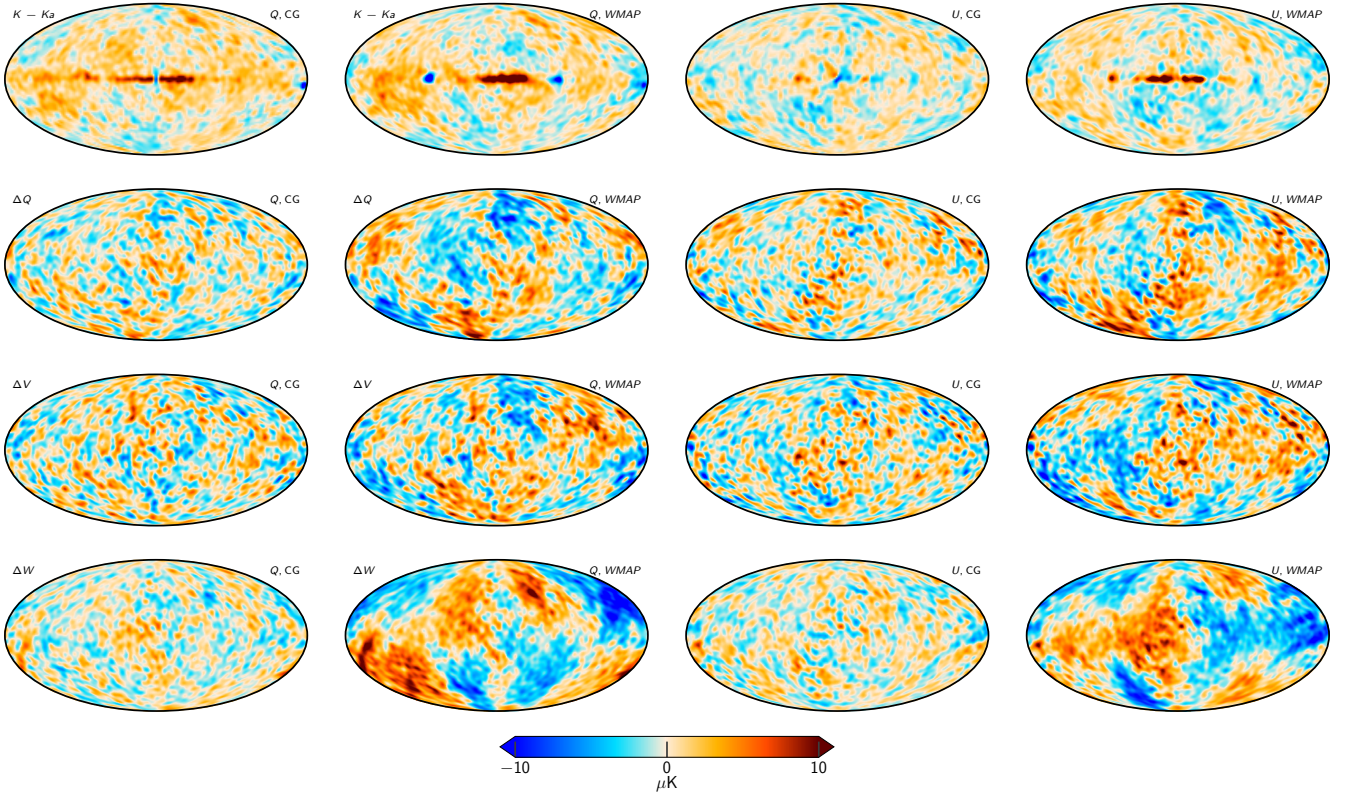


**Fig. 20.** Internal WMAP difference maps, smoothed by  $10^\circ$ .

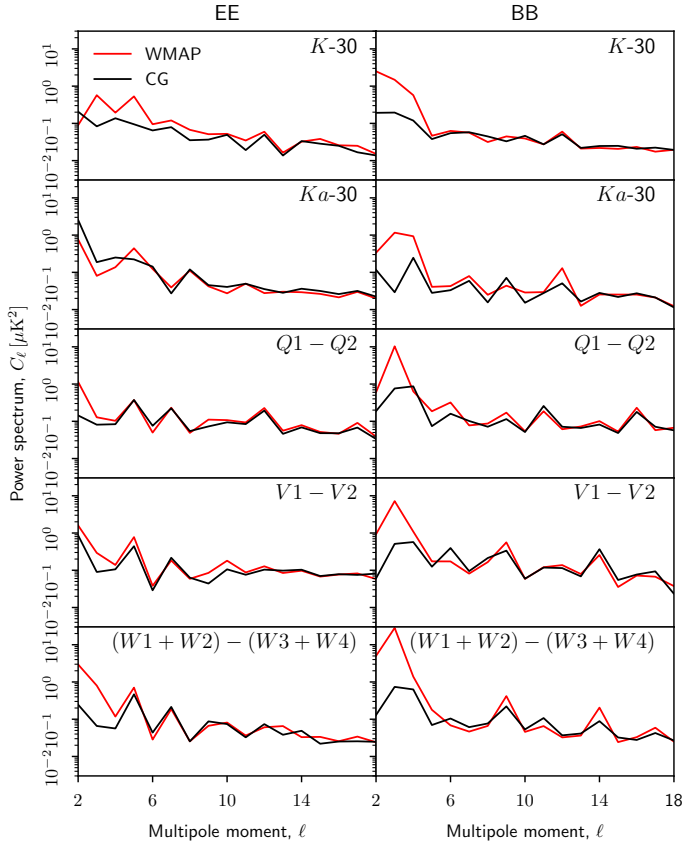
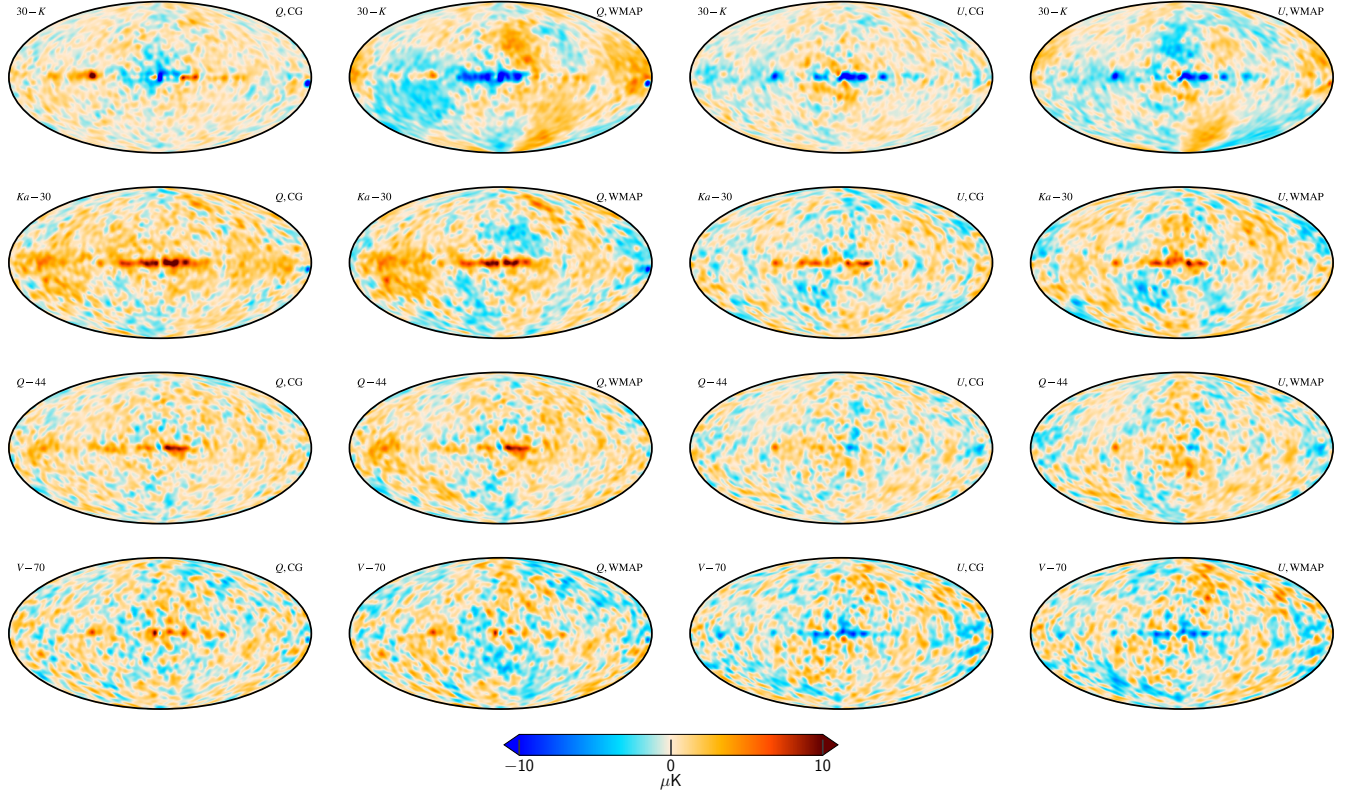


**Fig. 21.** Half-difference spectra.

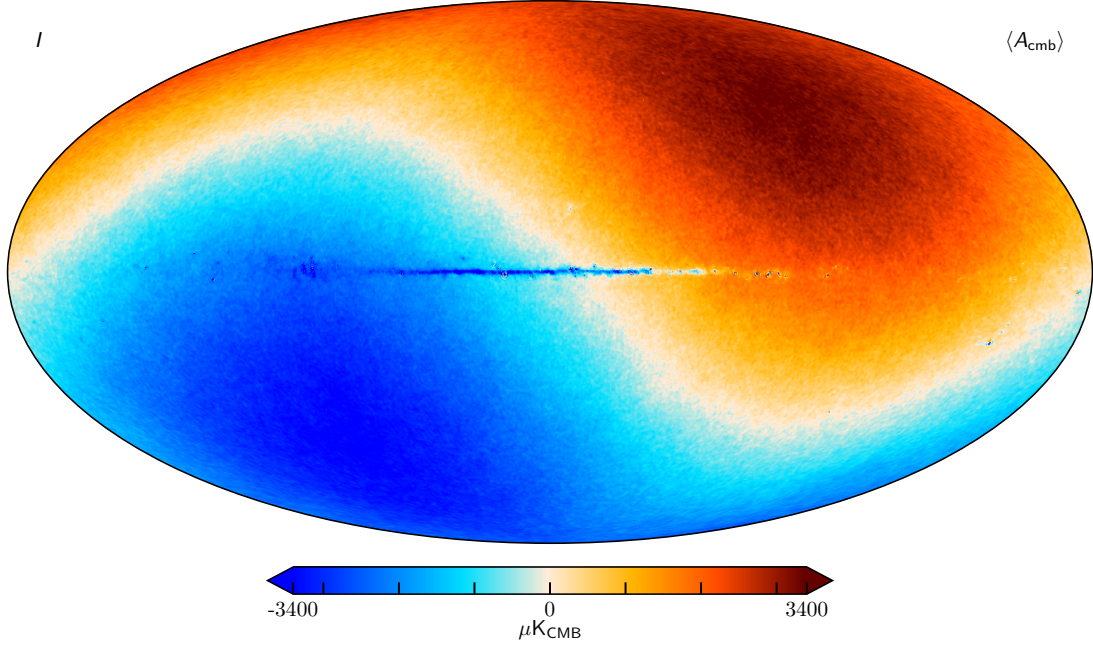
is an unsurprising result as the only true difference other than the AME model is the addition of the WMAP  $K$ -band to this analysis.

In polarization, the addition of *Planck* 353 GHz provides an anchor for the polarized thermal dust emission, and as a result only the polarized synchrotron emission amplitude is explicitly fit in this work. The Stokes  $Q$  and  $U$  synchrotron amplitude mean and standard deviations are shown in Fig. 33. The mean amplitude map is in good agreement with that presented in Svalheim et al. (2022), though the morphology of the standard deviation map matches more closely with that presented in Herman et al. (2022), which shows convolution of the WMAP and *Planck* scanning strategies. However, the uncertainty of the signal along the Galactic plane is more tightly constrained in this work as the AME component is assumed to be unpolarized.

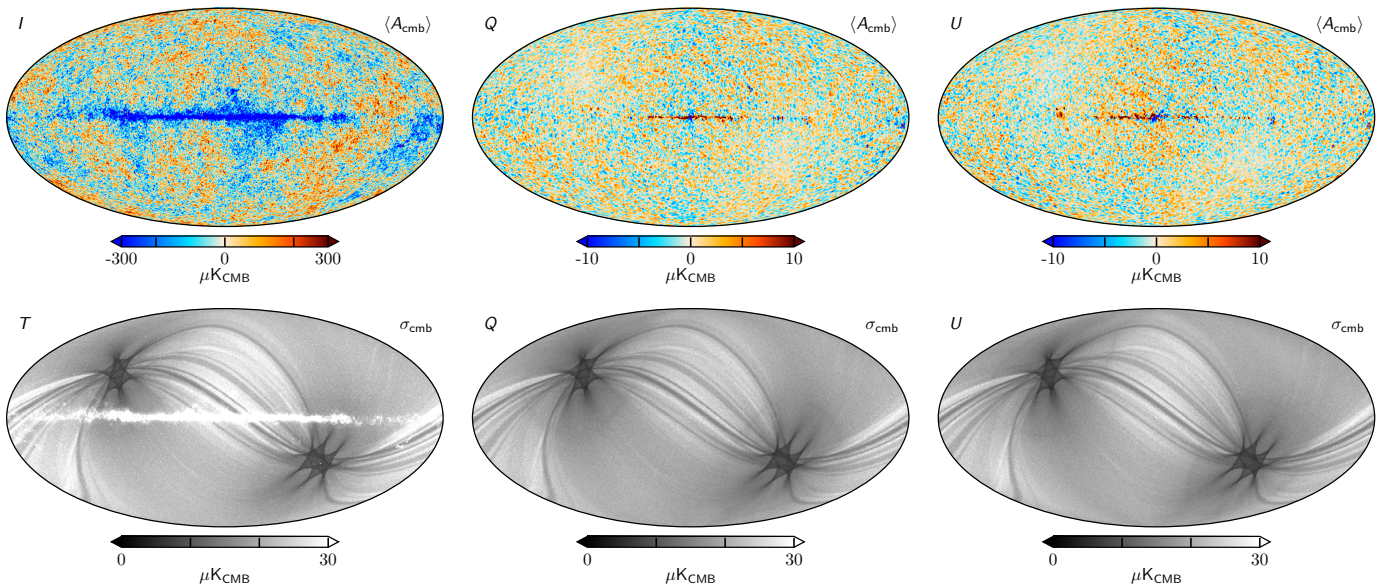
The quality of the component separation procedure is evaluated through a reduced- $\chi^2$  map, shown in Fig. 34, as well as through the map space residuals Fig. B.6.



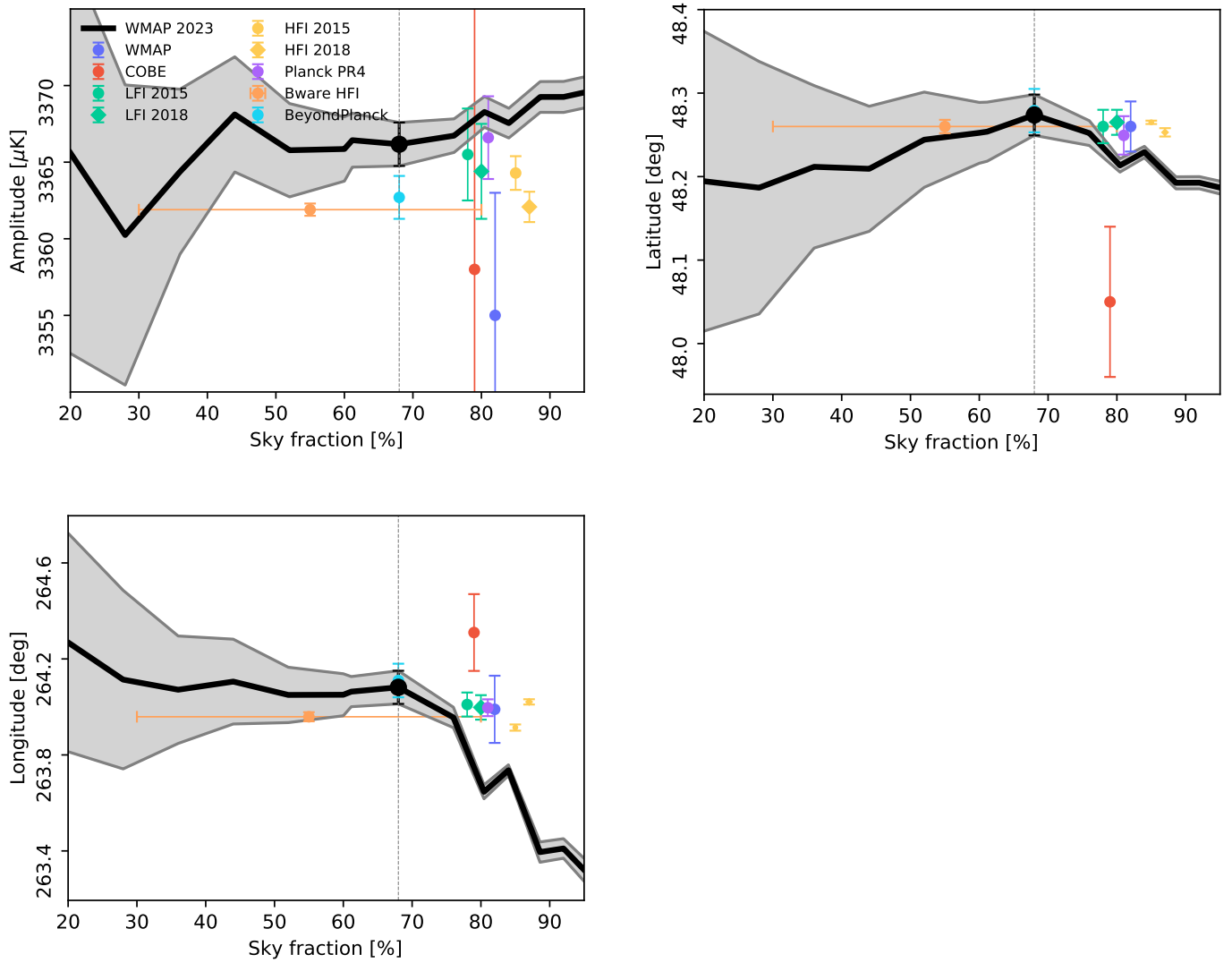
**Fig. 22.** Difference maps between similar *WMAP* and LFI frequency maps. The comparison plots go, by column: Stokes  $Q$  for the COSMOGLOBE sky maps, Stokes  $Q$  for official *WMAP* and BEYONDPLANCK data products, Stokes  $U$  for the COSMOGLOBEsky maps, and Stokes  $U$  for the official data products. (Top row) *WMAP* LFI 30 GHz minus  $K$ -band, scaled by the synchrotron power-law. (Top middle row) *WMAP*  $Ka$ -band minus LFI 30 GHz, also scaled by the synchrotron power-law. (Bottom middle row) *WMAP*  $Q$ -band compared to the LFI 44 GHz sky maps, scaled by the synchrotron power-law. (Bottom row) *WMAP*  $V$ -band minus LFI 70 GHz, with unit scalings for each band.



**Fig. 23.** Posterior mean CMB COSMOGLOBE temperature map, smoothed to an angular resolution of 14' FWHM.



**Fig. 24.** Posterior mean CMB COSMOGLOBE maps and their standard deviation.



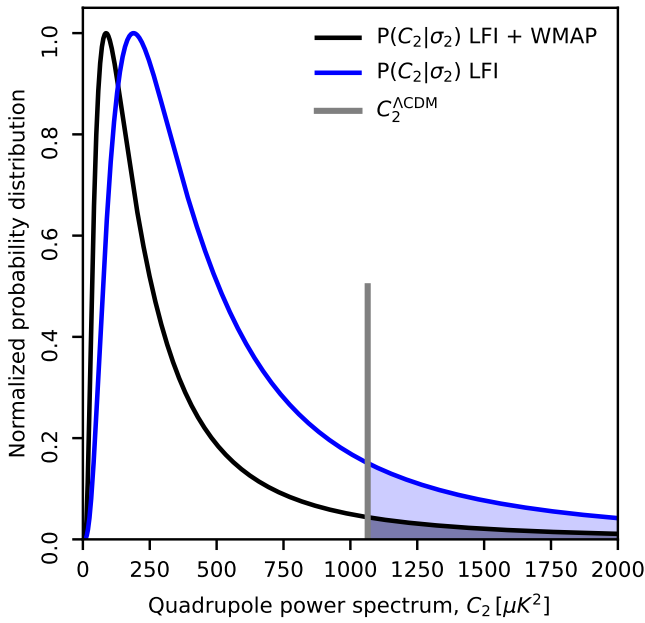


**Fig. 25.** Marginal probability distribution of the ensemble-averaged  $C_2$  given the data,  $P(C_2|d)$ , as measured by COSMOGLOBE (black) and BEYONDPLANCK (blue).

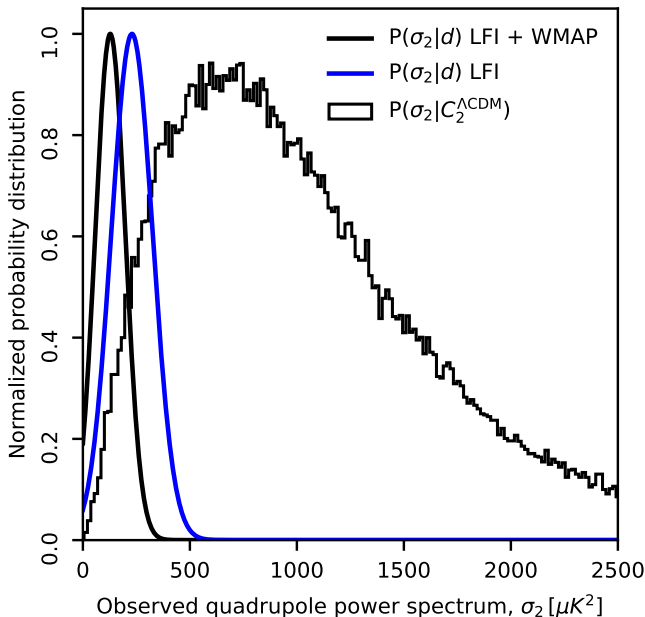


**Fig. 26.** Histogram of 100 000 realizations of  $C_2$  given  $C_2^{\Lambda\text{CDM}} = 1064.7$  compared with the measured power spectrum  $\sigma_2$  of our universe for COSMOGLOBE (black) and BEYONDPLANCK (blue).

### 6.3. WMAP-versus-LFI signal-to-noise ratio comparison

## 7. Systematic error corrections and uncertainties

### 7.1. Sky map corrections

### 7.2. Power spectrum residuals

## 8. Outstanding issues

### 8.1. Noise modeling

### 8.2. V-band quadrupole residual

### 8.3. Degeneracy between K-band calibration and AME dipole

### 8.4. Other minor effects

#### 8.4.1. Time-variable bandpass modeling

#### 8.4.2. Polarized sidelobe modeling

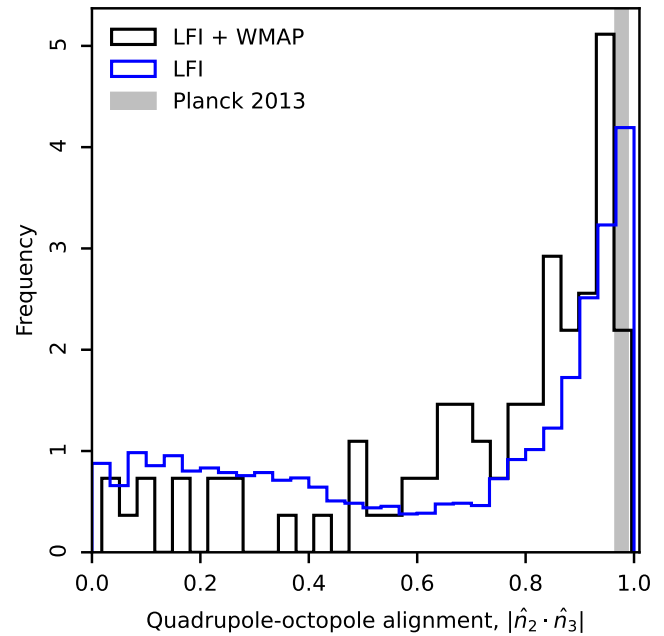


**Fig. 27.** The quadrupole-octopole alignment of COSMOGLOBE compared with BEYONDPLANCK.

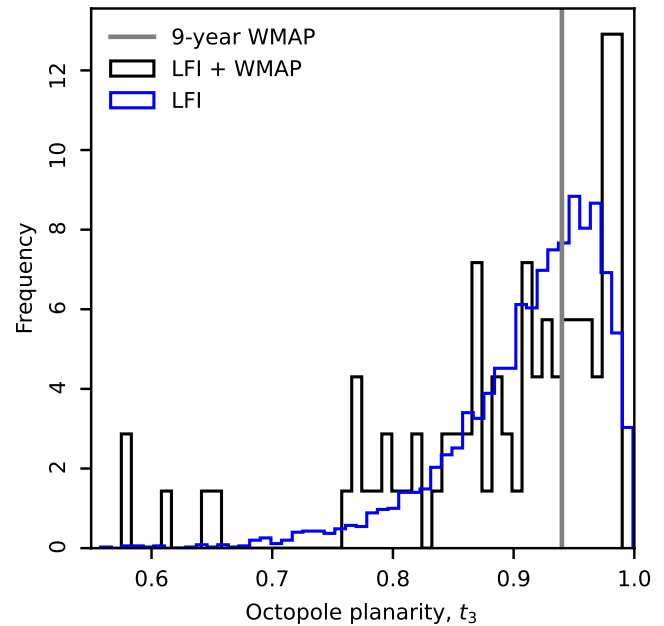


**Fig. 28.** The octopole planarity statistics  $t_3$  compared with the BEYONDPLANCK analysis (blue).

- Ali-Haïmoud, Y., Hirata, C. M., & Dickinson, C. 2009, MNRAS, 395, 1055  
 Alonso, D., Sanchez, J., Slosar, A., & LSST Dark Energy Science Collaboration. 2019, MNRAS, 484, 4127  
 Andersen et al. 2022, A&A, in press [[arXiv:2201.08188](https://arxiv.org/abs/2201.08188)]  
 Barnes, C., Hill, R. S., Hinshaw, G., et al. 2003, ApJS, 148, 51  
 Barrett, R., Berry, M. W., Chan, T. F., et al. 1994, Templates for the Solution of Linear Systems (Society for Industrial and Applied Mathematics)  
 Basyrov et al. 2022, A&A, submitted [[arXiv:2208.14293](https://arxiv.org/abs/2208.14293)]  
 Bennett, C. L., Bay, M., Halpern, M., et al. 2003a, ApJ, 583, 1  
 Bennett, C. L., Halpern, M., Hinshaw, G., et al. 2003b, ApJS, 148, 1  
 Bennett, C. L., Larson, D., Weiland, J. L., et al. 2013, ApJS, 208, 20  
 Bennett, C. L., Smoot, G. F., Hinshaw, G., et al. 1992, ApJ, 396, L7  
 BeyondPlanck. 2022, A&A, submitted [[arXiv:2011.05609](https://arxiv.org/abs/2011.05609)]

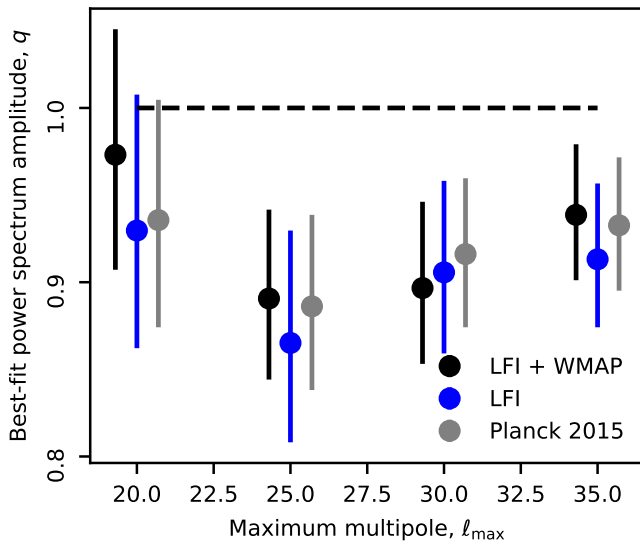


**Fig. 29.** Best-fit amplitude,  $q$ , of the low multipole power spectrum  $C_\ell = qC_\ell^{\Lambda\text{CDM}}$ ,  $2 \leq \ell \leq \ell_{\max}$  compared to *Planck*2015 (grey) and BeyondPlanck (blue).

- Dicke, R. H., Peebles, P. J. E., Roll, P. G., & Wilkinson, D. T. 1965, ApJ, 142, 414  
 Fixsen, D. J. 2009, ApJ, 707, 916  
 Frigo, M. & Johnson, S. G. 2005, Proceedings of the IEEE, 93, 216, special issue on “Program Generation, Optimization, and Platform Adaptation”  
 Galloway et al. 2022, A&A, in press [arXiv:2201.03509]  
 Gjerløw et al. 2022, A&A, submitted [arXiv:2011.08082]  
 Greason, M. R., Limon, M., Wollack, E., et al. 2012, Nine-Year Explanatory Supplement, 5th edn., Greenbelt, MD: NASA/GSFC  
 Haslam, C. G. T., Salter, C. J., Stoffel, H., & Wilson, W. E. 1982, A&AS, 47, 1  
 Herman et al. 2022, A&A, in press [arXiv:2201.03530]  
 Hill, R. S., Weiland, J. L., Odegard, N., et al. 2009, ApJS, 180, 246  
 Hinshaw, G., Barnes, C., Bennett, C. L., et al. 2003, ApJS, 148, 63  
 Hinshaw, G., Nolta, M. R., Bennett, C. L., et al. 2007, ApJS, 170, 288  
 Hinshaw, G., Weiland, J. L., Hill, R. S., et al. 2009, ApJS, 180, 225  
 Hu, W., Fukugita, M., Zaldarriaga, M., & Tegmark, M. 2001, ApJ, 549, 669  
 Ihle et al. 2022, A&A, in press [arXiv:2011.06650]  
 Jarosik, N., Barnes, C., Bennett, C. L., et al. 2003a, ApJS, 148, 29  
 Jarosik, N., Barnes, C., Greason, M. R., et al. 2007, ApJS, 170, 263  
 Jarosik, N., Bennett, C. L., Dunkley, J., et al. 2011, ApJS, 192, 14  
 Jarosik, N., Bennett, C. L., Halpern, M., et al. 2003b, ApJS, 145, 413  
 Keihänen et al. 2022, A&A, in press [arXiv:2011.06024]  
 Lange, A. E., Ade, P. A., Bock, J. J., et al. 2001, Phys. Rev. D, 63, 042001  
 Larson, D., Weiland, J. L., Hinshaw, G., & Bennett, C. L. 2015, ApJ, 801, 9  
 Mather, J. C., Cheng, E. S., Cottingham, D. A., et al. 1994, ApJ, 420, 439  
 Mather, J. C., Fixsen, D. J., Shafer, R. A., Mosier, C., & Wilkinson, D. T. 1999, ApJ, 512, 511  
 Notari, A. & Quartin, M. 2015, Journal of Cosmology and Astroparticle Physics, 2015, 047–047  
 Page, L., Jackson, C., Barnes, C., et al. 2003, ApJ, 585, 566  
 Paradiso et al. 2022, A&A, submitted [arXiv:2205.10104]  
 Penzias, A. A. & Wilson, R. W. 1965, ApJ, 142, 419  
 Planck Collaboration II. 2016, A&A, 594, A2  
 Planck Collaboration I. 2020, A&A, 641, A1  
 Planck Collaboration II. 2020, A&A, 641, A2  
 Planck Collaboration III. 2020, A&A, 641, A3  
 Planck Collaboration Int. XV. 2014, A&A, 565, A103  
 Planck Collaboration Int. XLVI. 2016, A&A, 596, A107  
 Press, W. H., Teukolsky, S. A., Vetterling, W. T., & Flannery, B. P. 2007, Numerical Recipes 3rd Edition: The Art of Scientific Computing, 3rd edn. (USA: Cambridge University Press)  
 Remazeilles, M., Dickinson, C., Banday, A. J., Bigot-Sazy, M.-A., & Ghosh, T. 2015, MNRAS, 451, 4311  
 Silsbee, K., Ali-Haïmoud, Y., & Hirata, C. M. 2011, MNRAS, 411, 2750  
 Smoot, G. F., Bennett, C. L., Kogut, A., et al. 1992, ApJ, 396, L1  
 Stevenson, M. A. 2014, The Astrophysical Journal, 781, 113  
 Svalheim et al. 2022, A&A, in press [arXiv:2011.08503]  
 Tramonte, D., Génova-Santos, R. T., Rubiño-Martín, J. A., et al. 2023, MNRAS, 519, 3432  
 van der Vorst, H. A. 1992, SIAM Journal on Scientific and Statistical Computing, 13, 631  
 Watts et al. 2022, A&A, in press [arXiv:2202.11979]  
 Weiland, J. L., Odegard, N., Hill, R. S., et al. 2011, ApJS, 192, 19

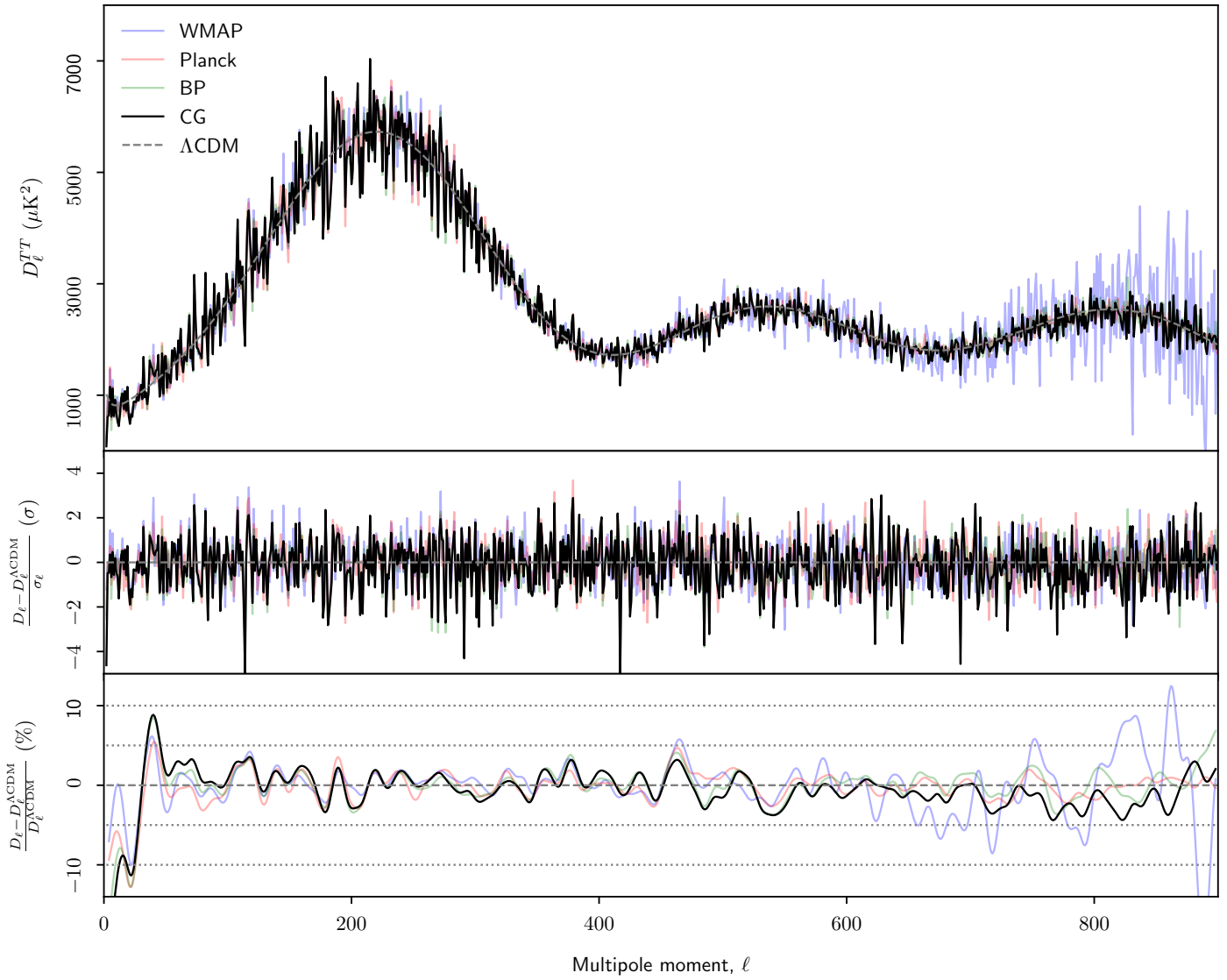


**Fig. 30.** Temperature power spectra from COSMOGLOBE, BEYONDPLANCK, WMAP9, and *Planck* DR4, compared with the *Planck* 2018  $\Lambda$ CDM prediction.

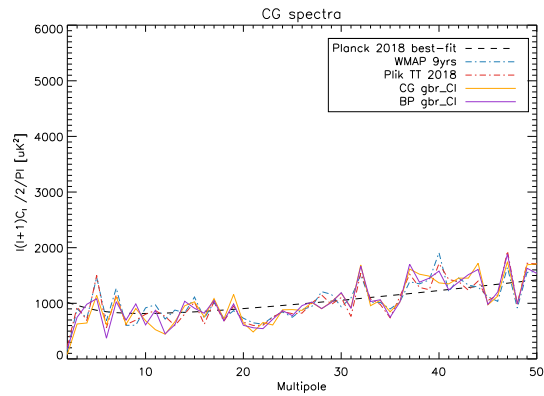


**Fig. 31.** Low-multipole temperature power spectrum

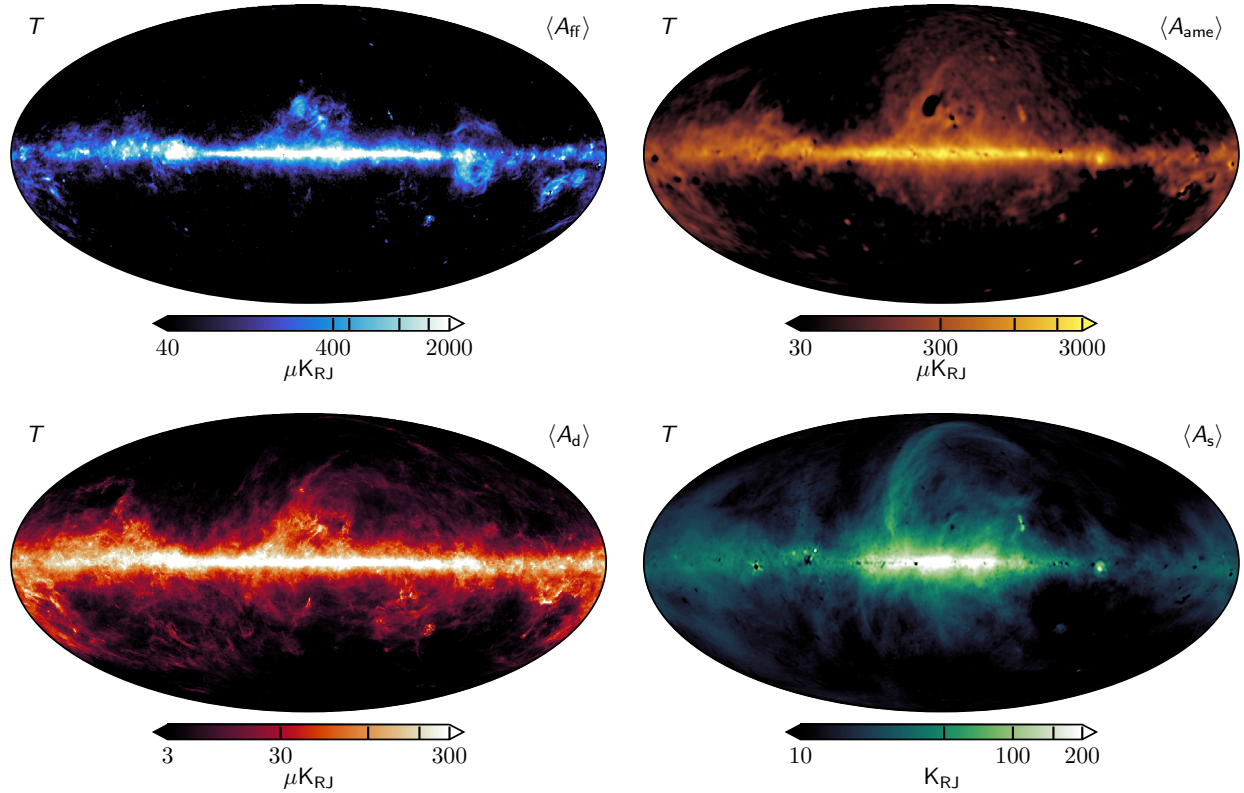


**Fig. 32.** Foreground intensity maps, evaluated at their respective reference frequencies. (Top left) Free-free emission at 40 GHz. (Top right) Anomalous microwave emission evaluated at 22 GHz. (Bottom left) Thermal dust emission at 70 GHz. (Bottom right) Synchrotron emission evaluated at 408 MHz.

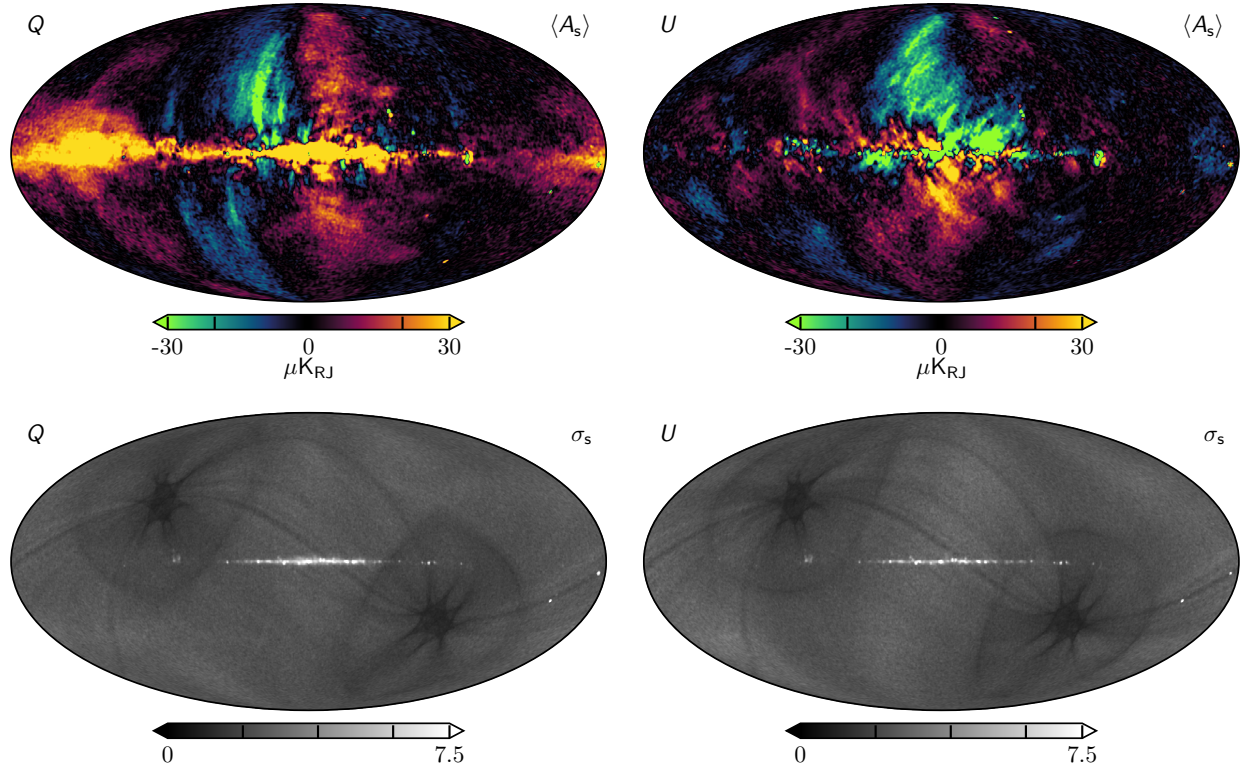


**Fig. 33.** Polarized synchrotron maps and their standard deviations evaluated at 30 GHz.

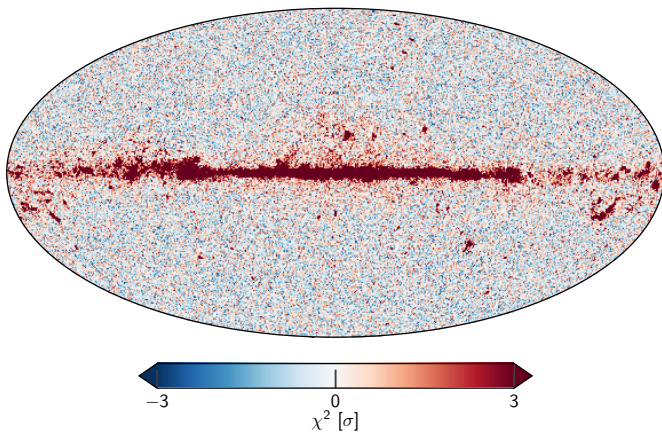


**Fig. 34.** Reduced- $\chi^2$ , using  $n_{\text{dof}} = 300$ , which comes from fitting to the regions outside of the  $K$ -band processing mask.

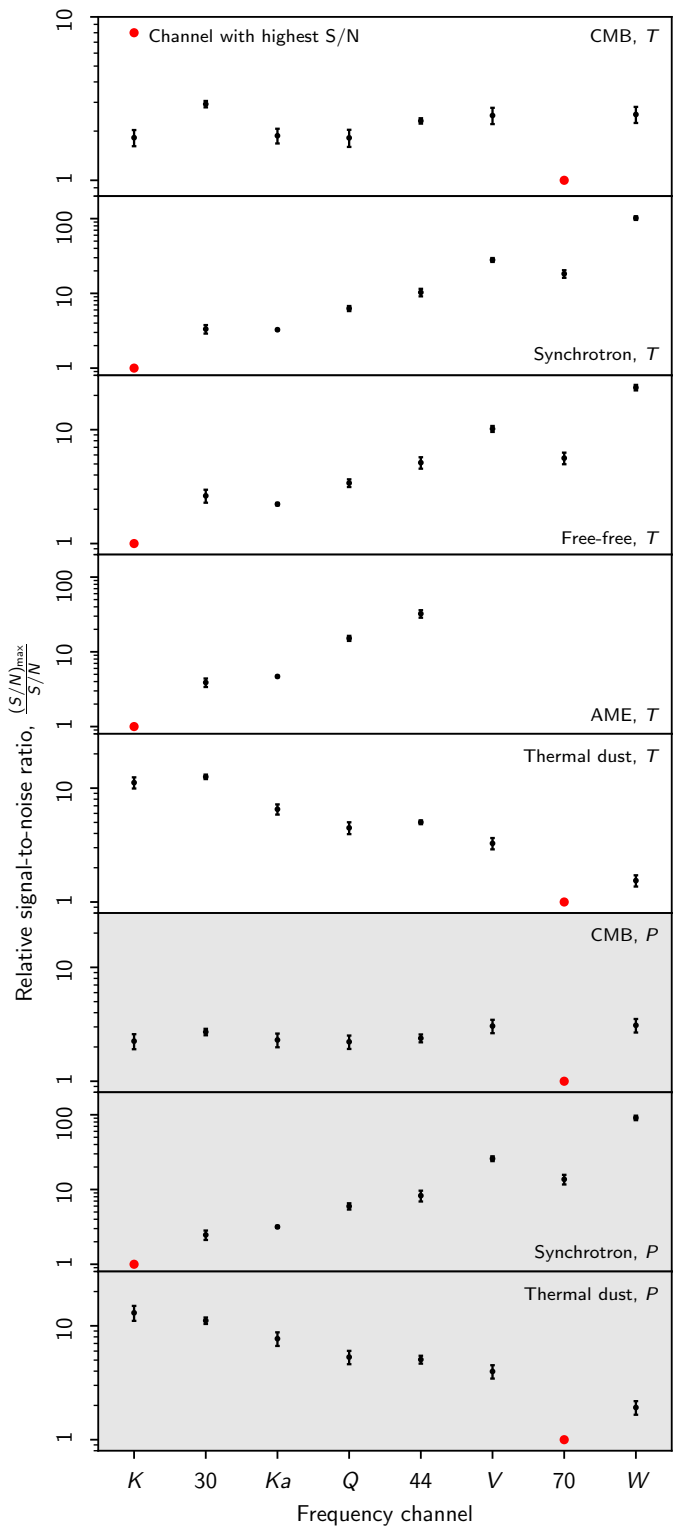


**Fig. 35.** Relative signal-to-noise ratios for WMAP and LFI channels and various components.

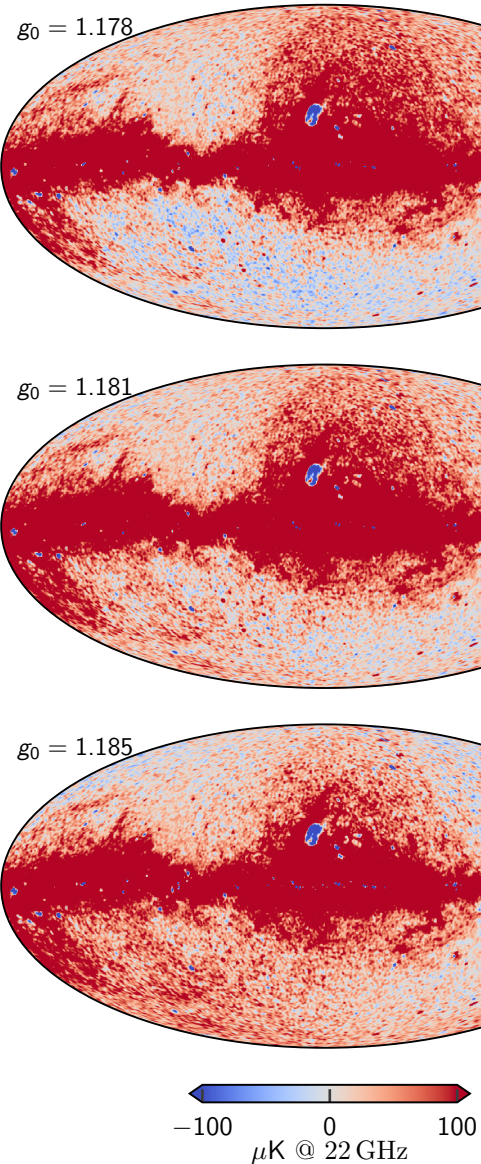


**Fig. 36.** Dependence on AME amplitude evaluated at 22 GHz as a function of absolute calibration. Each map comes from the fifth iteration of a dedicated `Commander` run that fixed  $g_0$  while letting all other TOD parameters be fit. The values of  $g_0 = 1.178$  and  $g_0 = 1.185$  represent  $3.5\sigma$  draws from the prior distribution with mean 1.1815 and standard deviation 0.001. The dipole visible in the top and bottom panels is aligned perfectly with the Solar dipole, and is directly due to variations in the  $K$ -band absolute calibration.

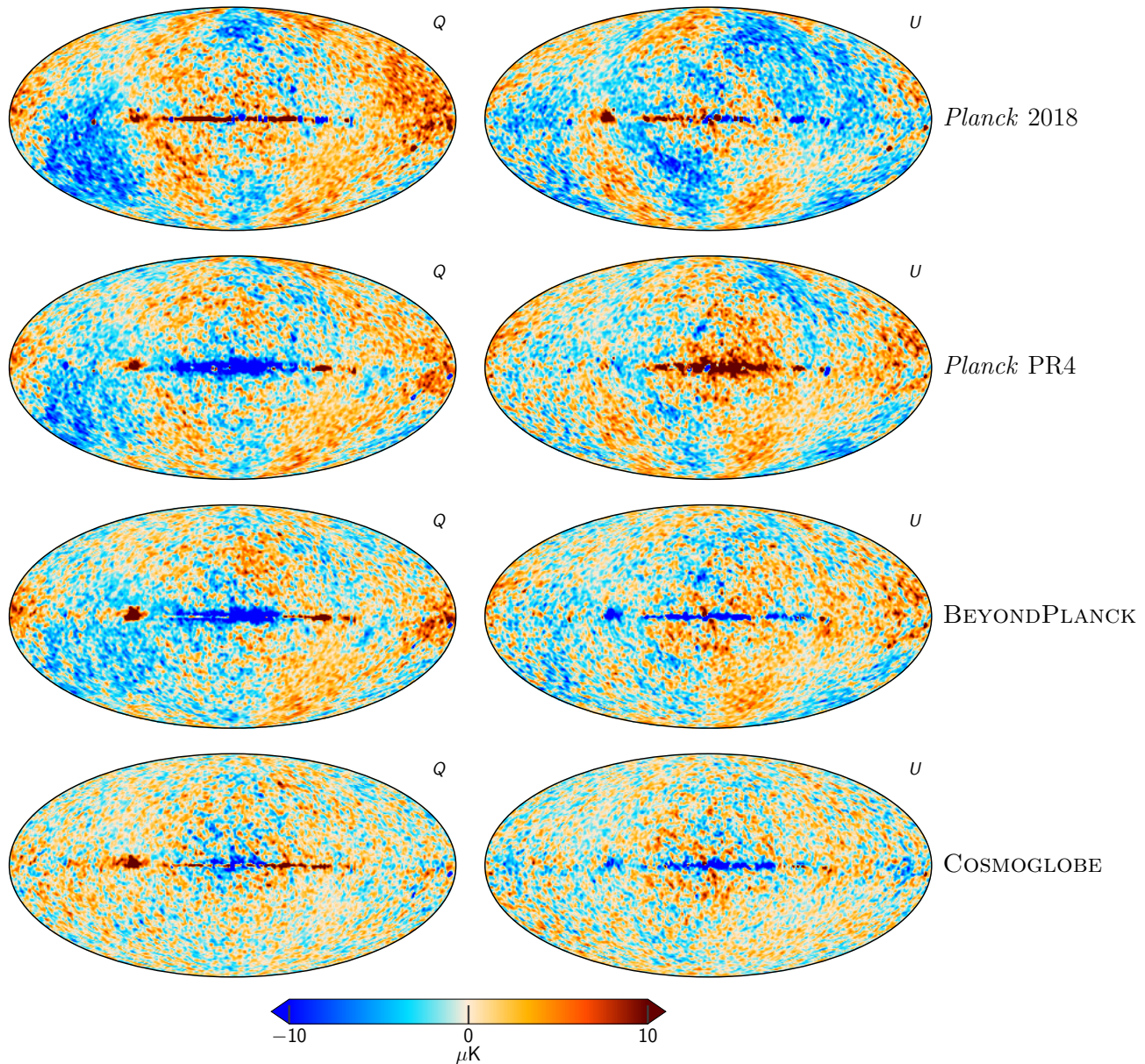


**Fig. 37.** Difference maps between the *Planck* 30 GHz and WMAP *K*-band maps. The columns are (1) *Planck* 2018 v. WMAP9, (2) *Planck* PR4 v. WMAP9, (3) BEYONDPLANCK v. WMAP9, and (4) COSMOGLOBE *Planck* 30 GHz and WMAP *K*-band both produced in this paper. All maps have been smoothed to a common resolution of  $2^\circ$  FWHM, and the *K*-band map has been scaled by 0.495 to account for different central frequencies, assuming a synchrotron spectral index  $\beta_s = -3.1$ .

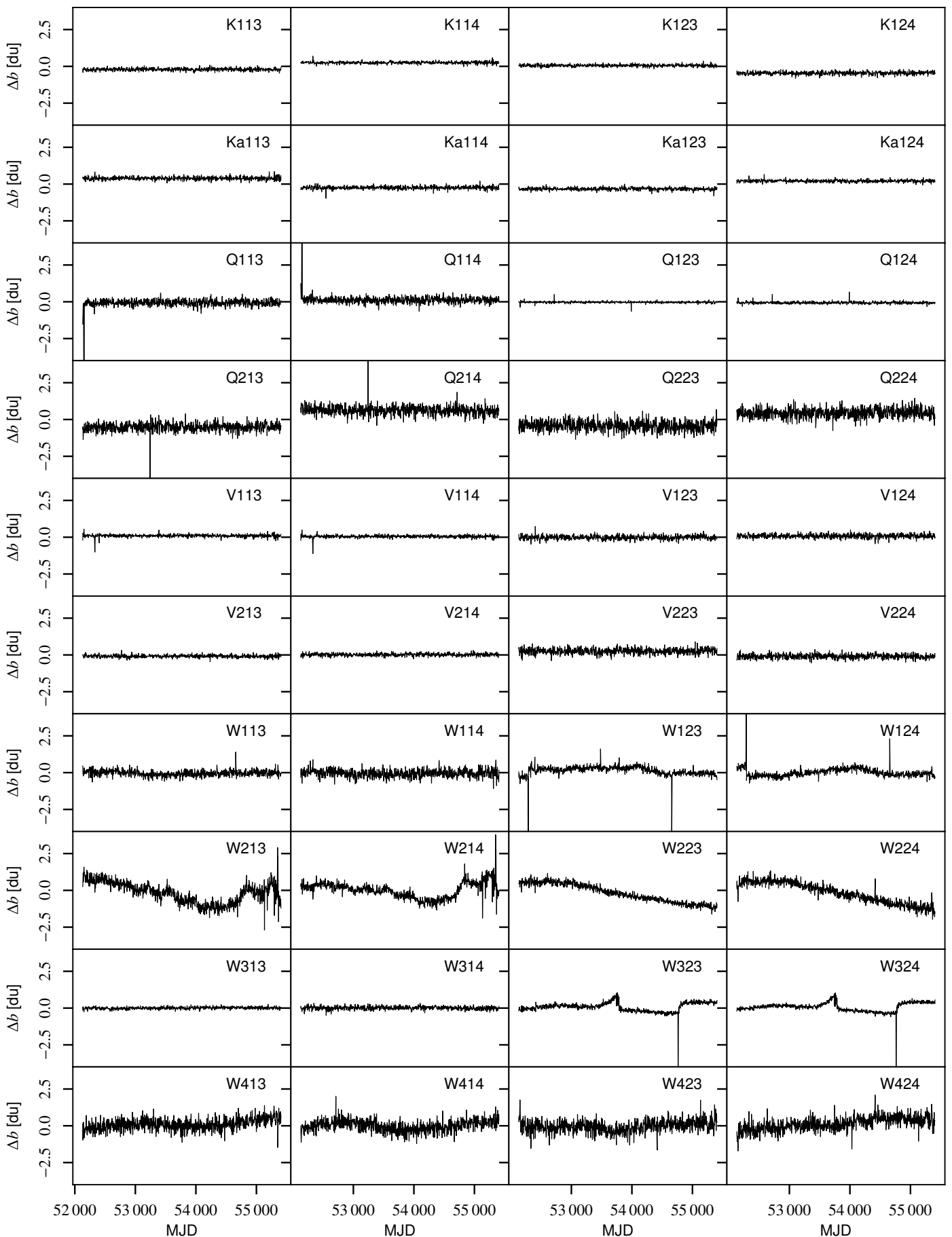
## **Appendix A: Survey of instrumental parameters**

*Appendix A.1: Gain, baselines, noise and  $\chi^2$*

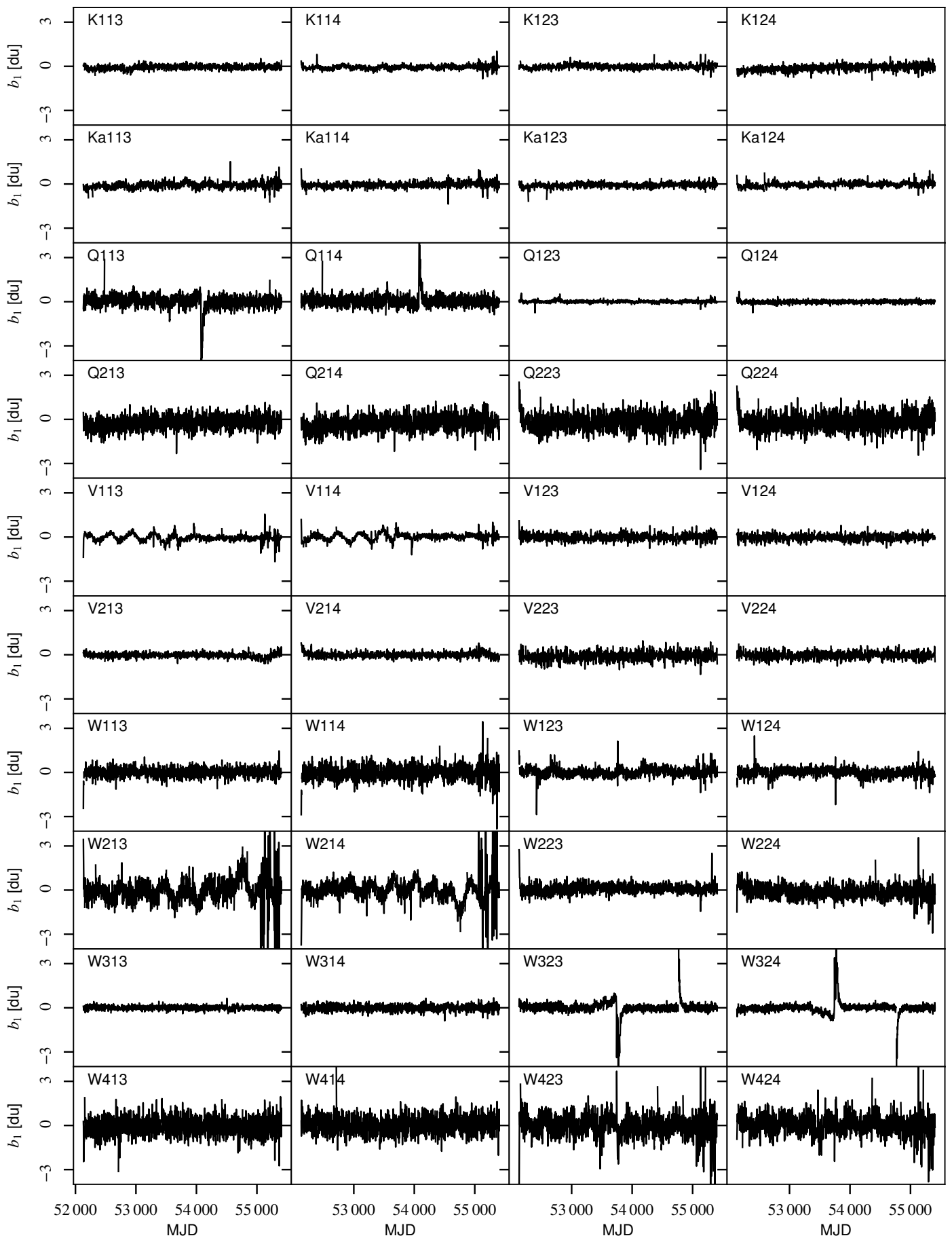
*Appendix A.2: Transmission imbalance*

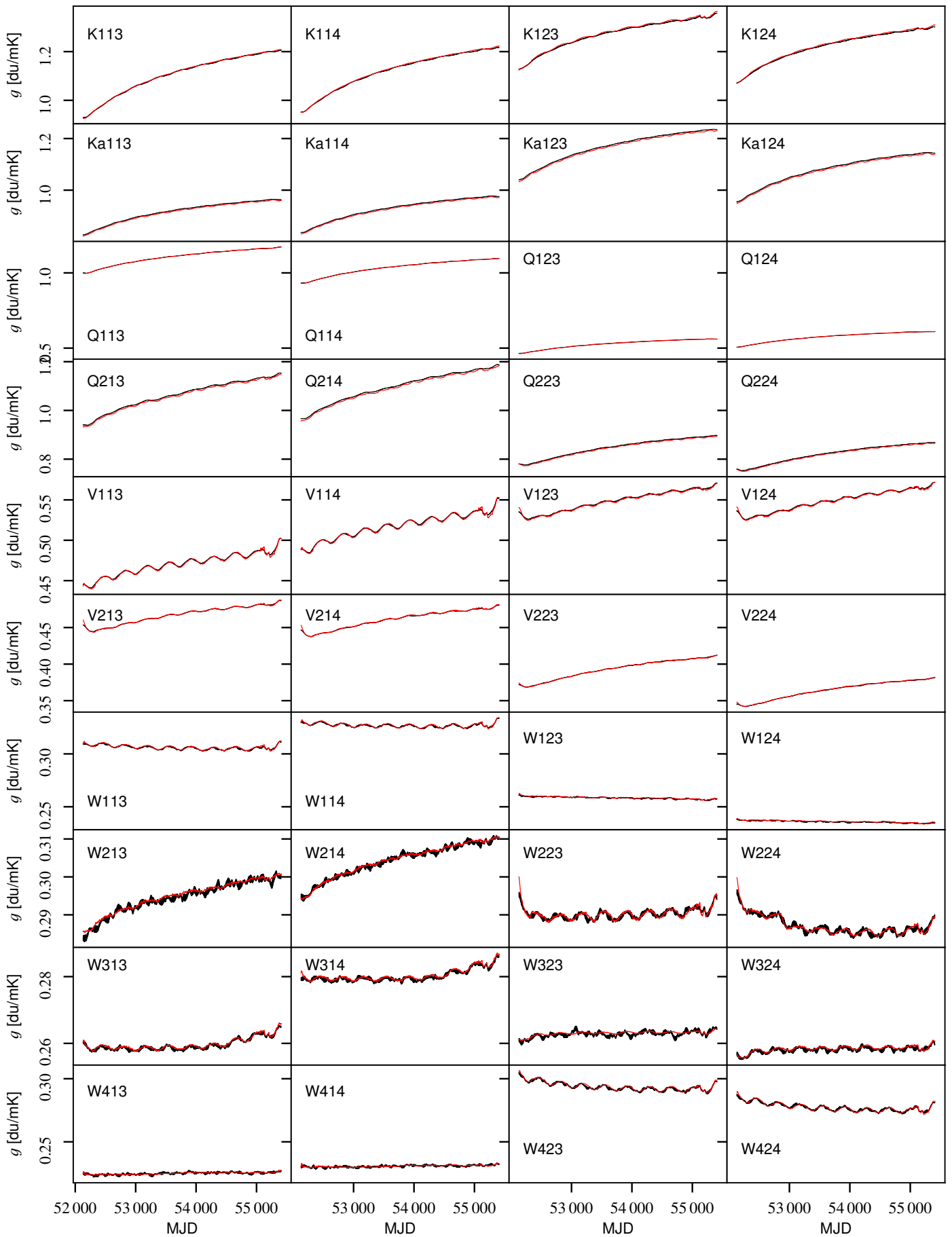
## **Appendix B: WMAP frequency map survey**

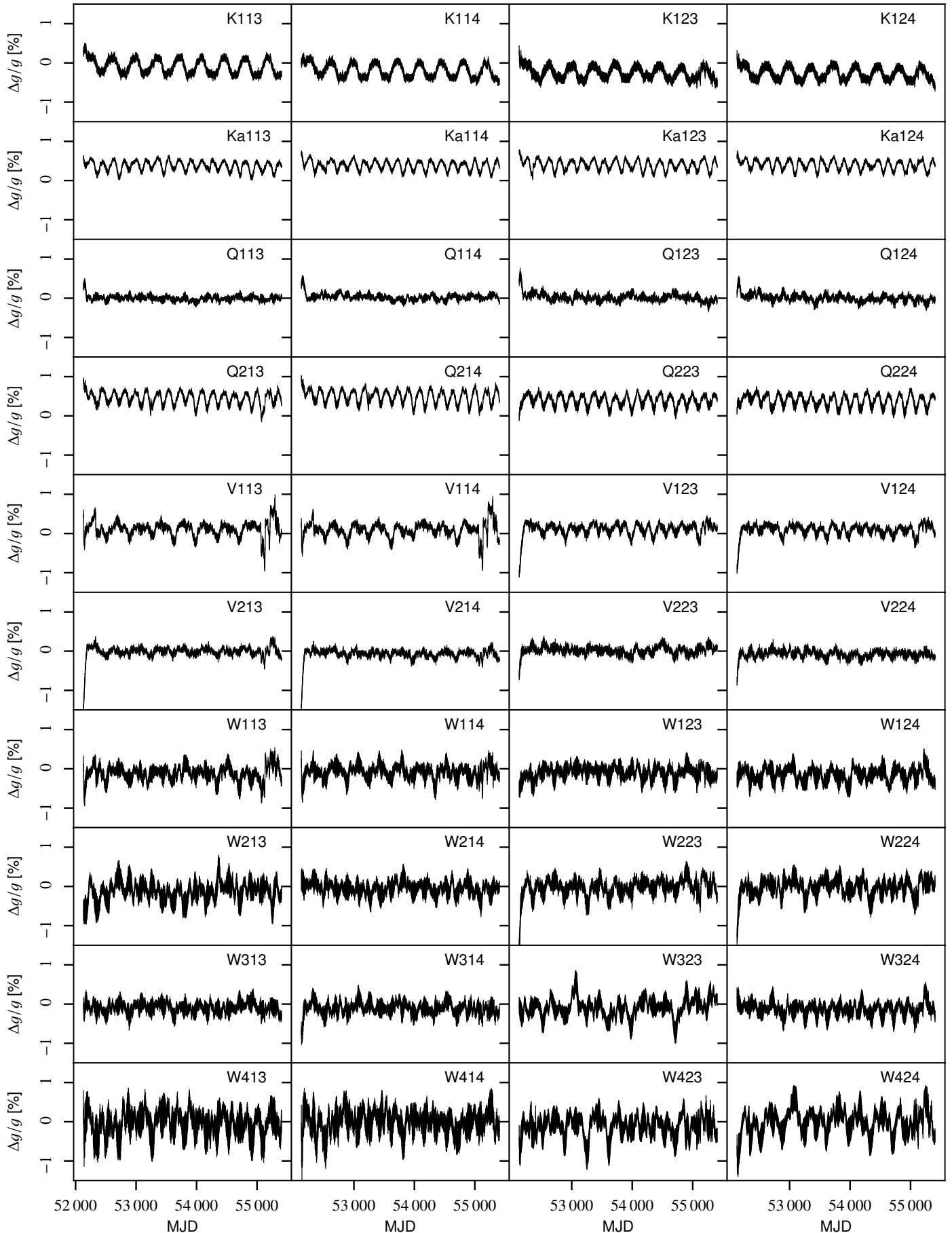
## **Appendix C: Comparison with BEYONDPLANCK LFI results**



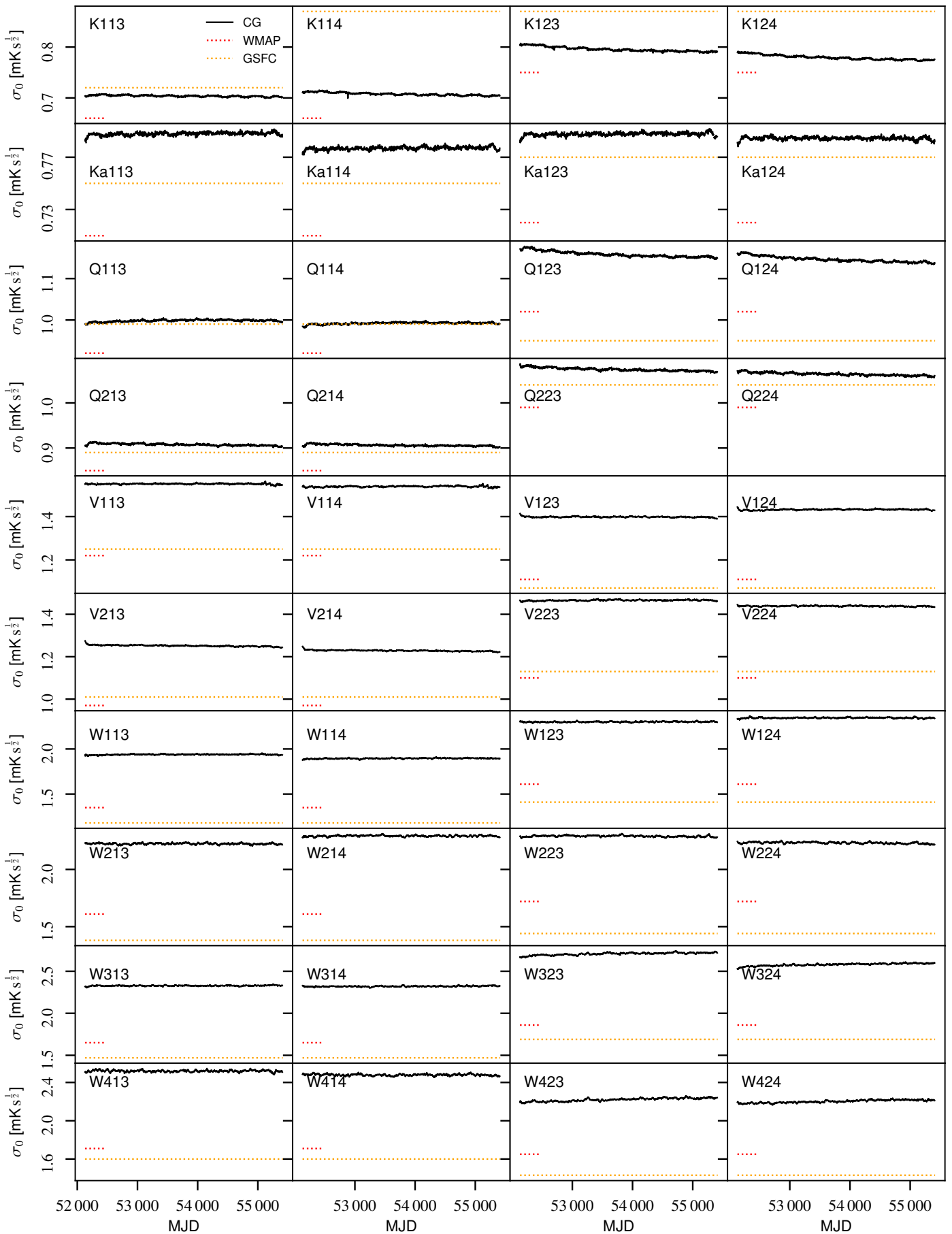
**Fig. A.1.** Difference in baseline solution,  $b_0^{\text{CG}} - b_0^{\text{WMAP}}$ .

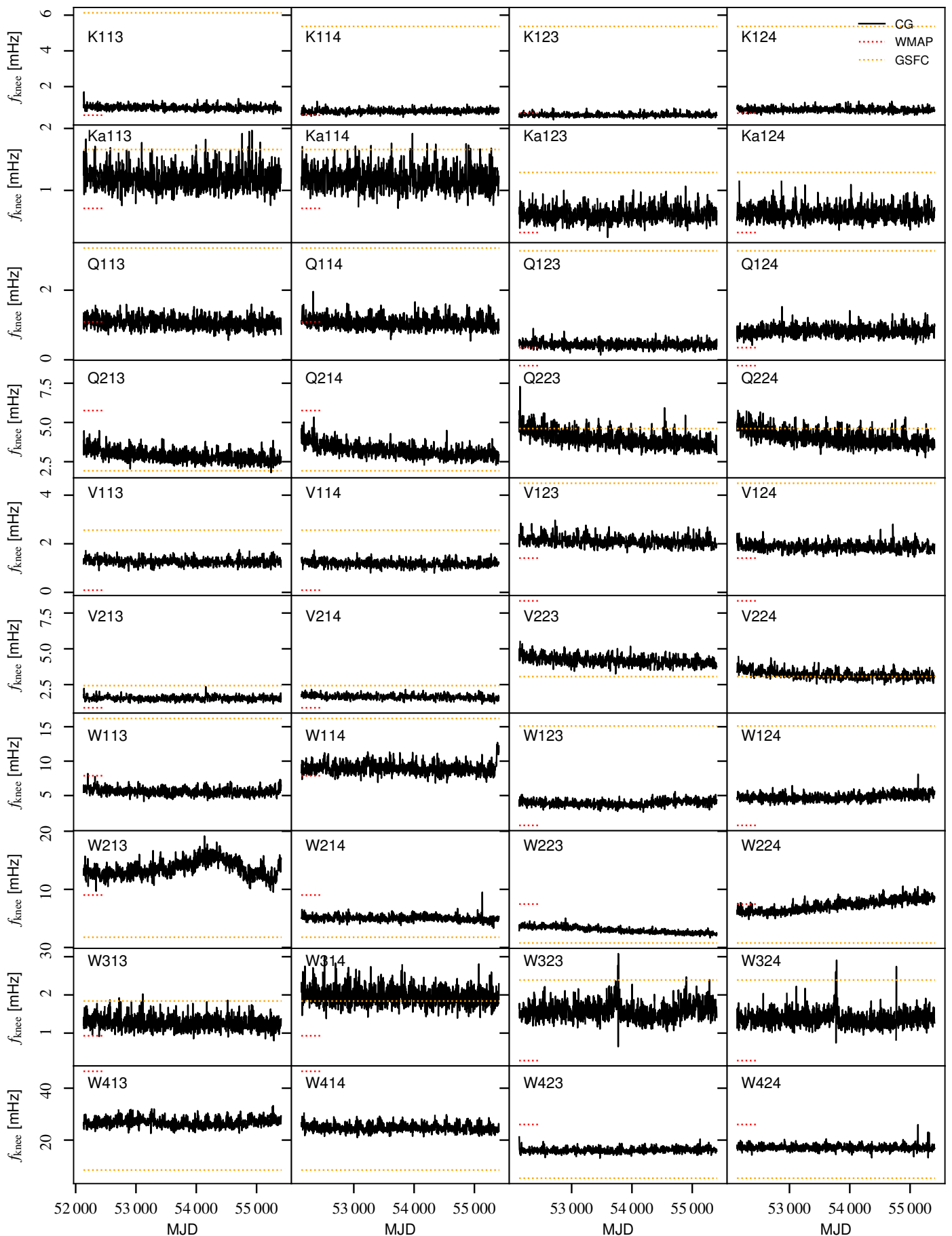
**Fig. A.2.** baseline slopes.

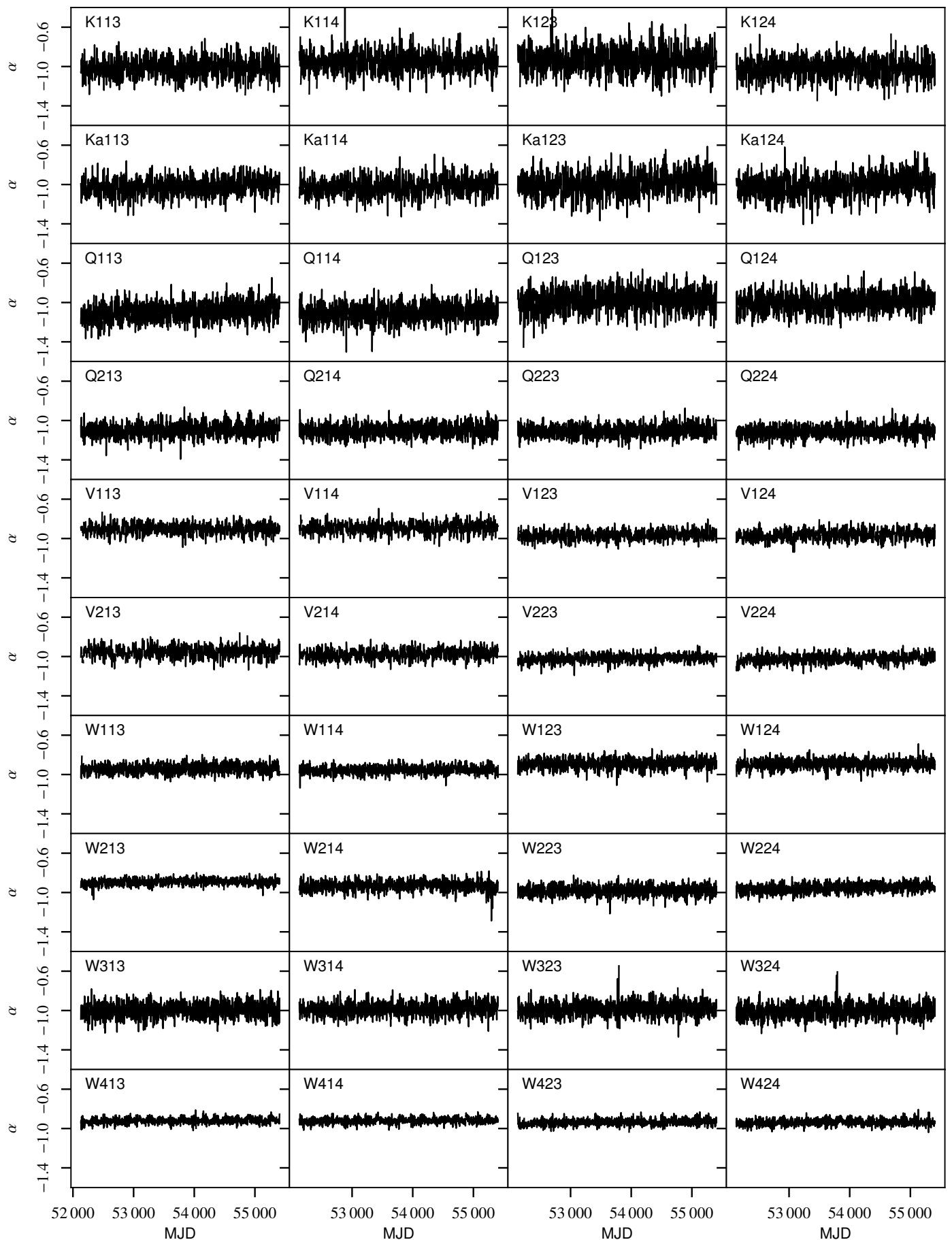
**Fig. A.3.** Gain.

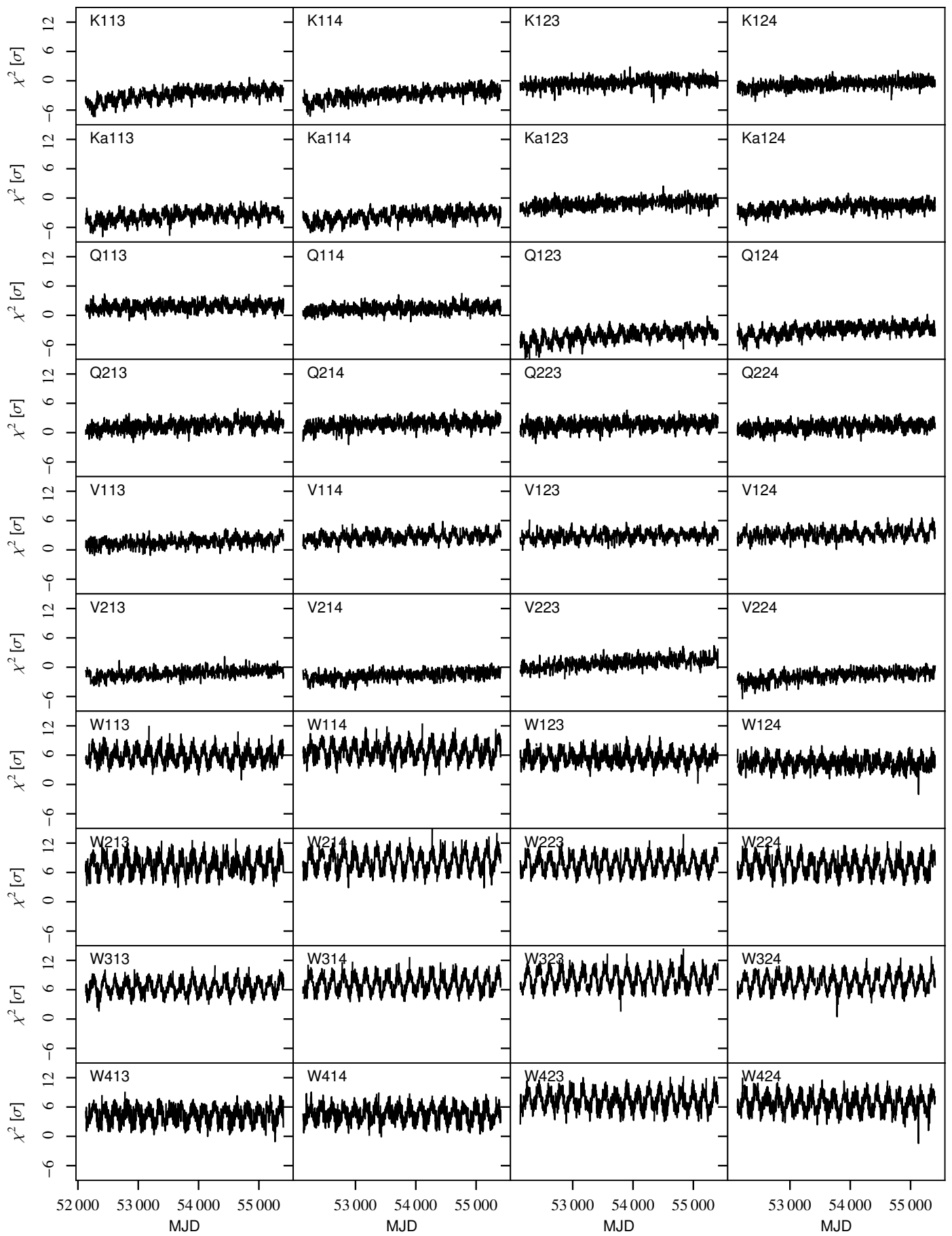


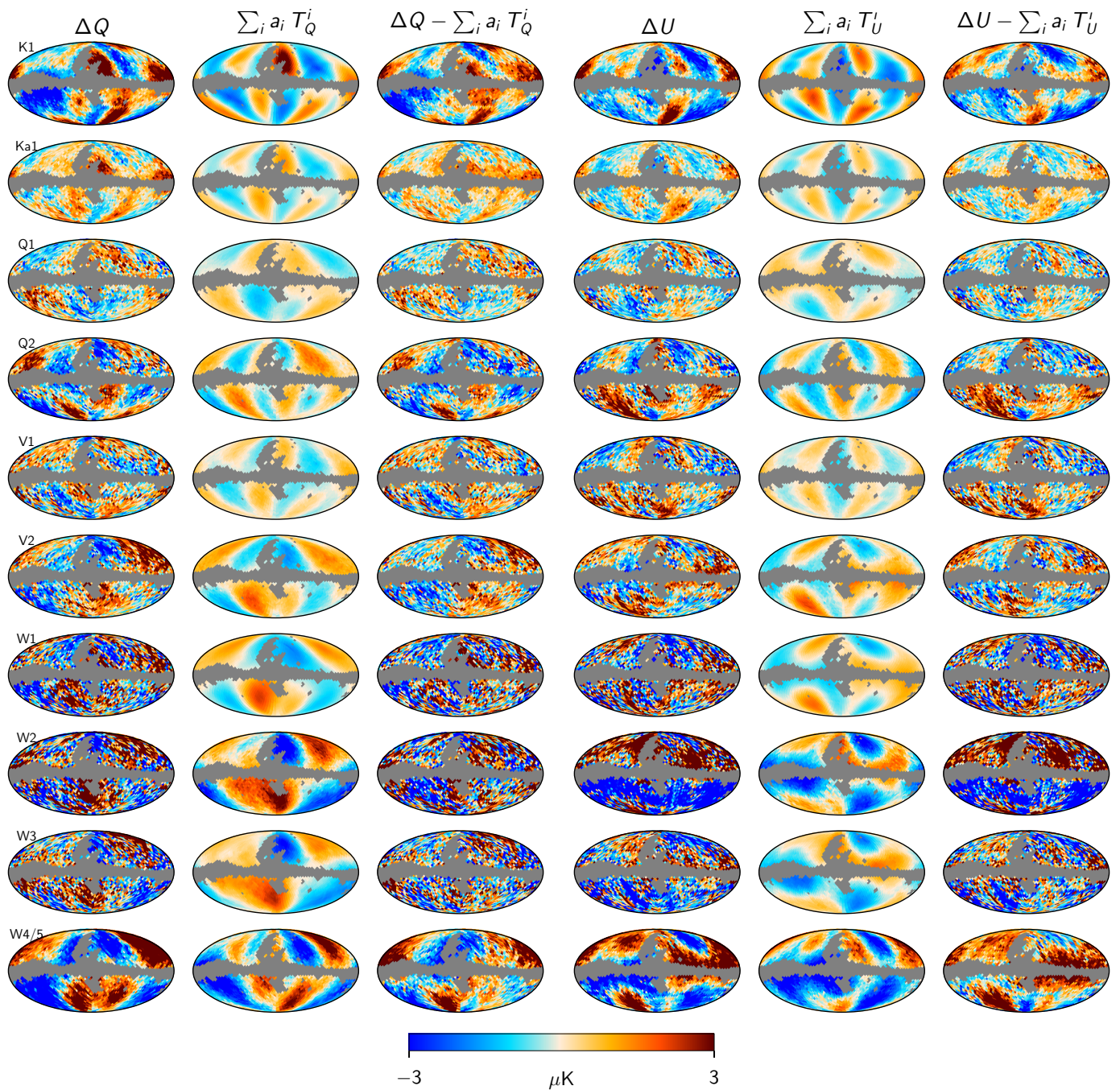
**Fig. A.4.** Relative difference in gain solutions,  $(g^{\text{CG}} - g^{\text{WMAP}})/g^{\text{WMAP}}$ .

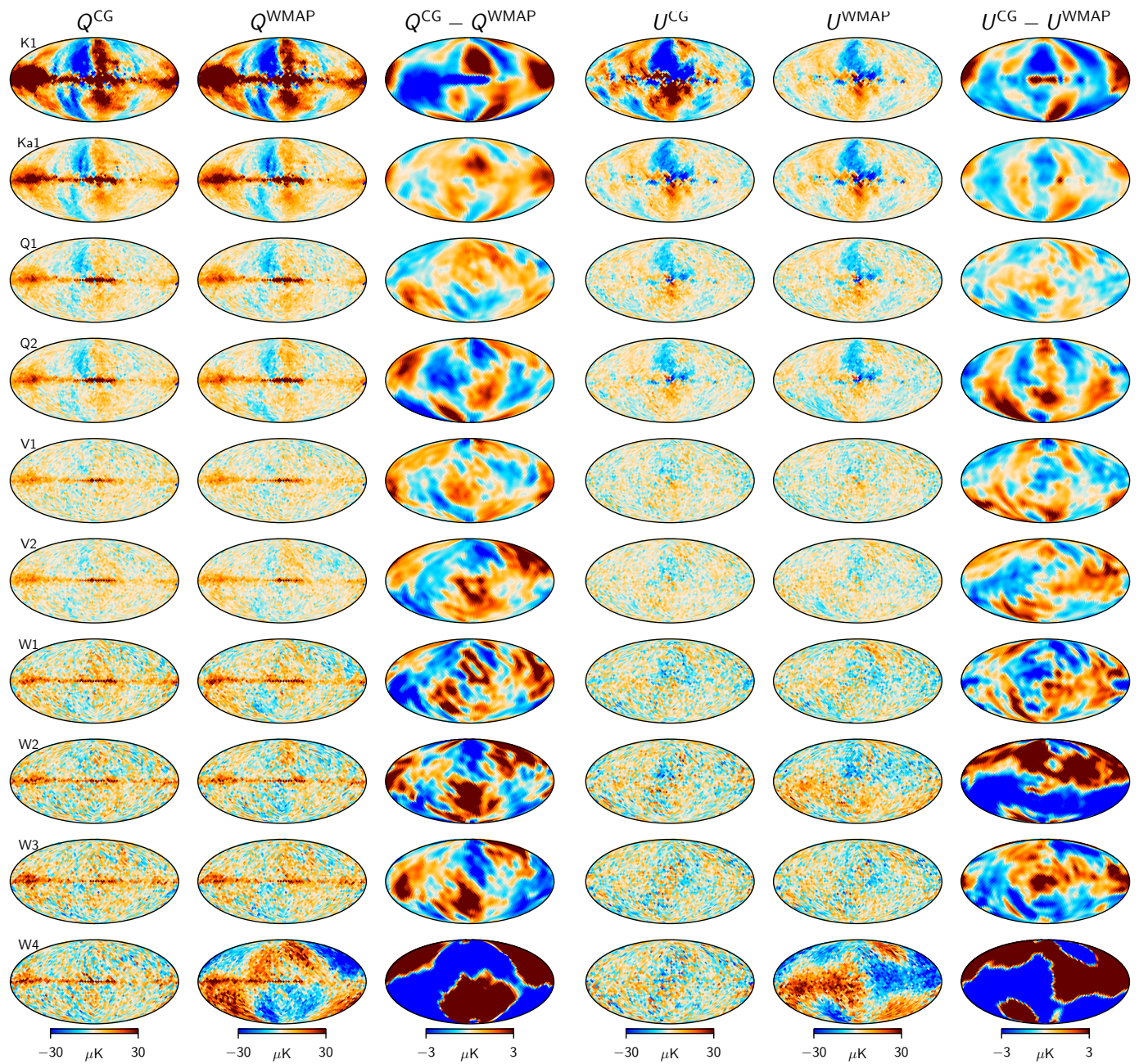
**Fig. A.5.**  $\sigma_0$ .

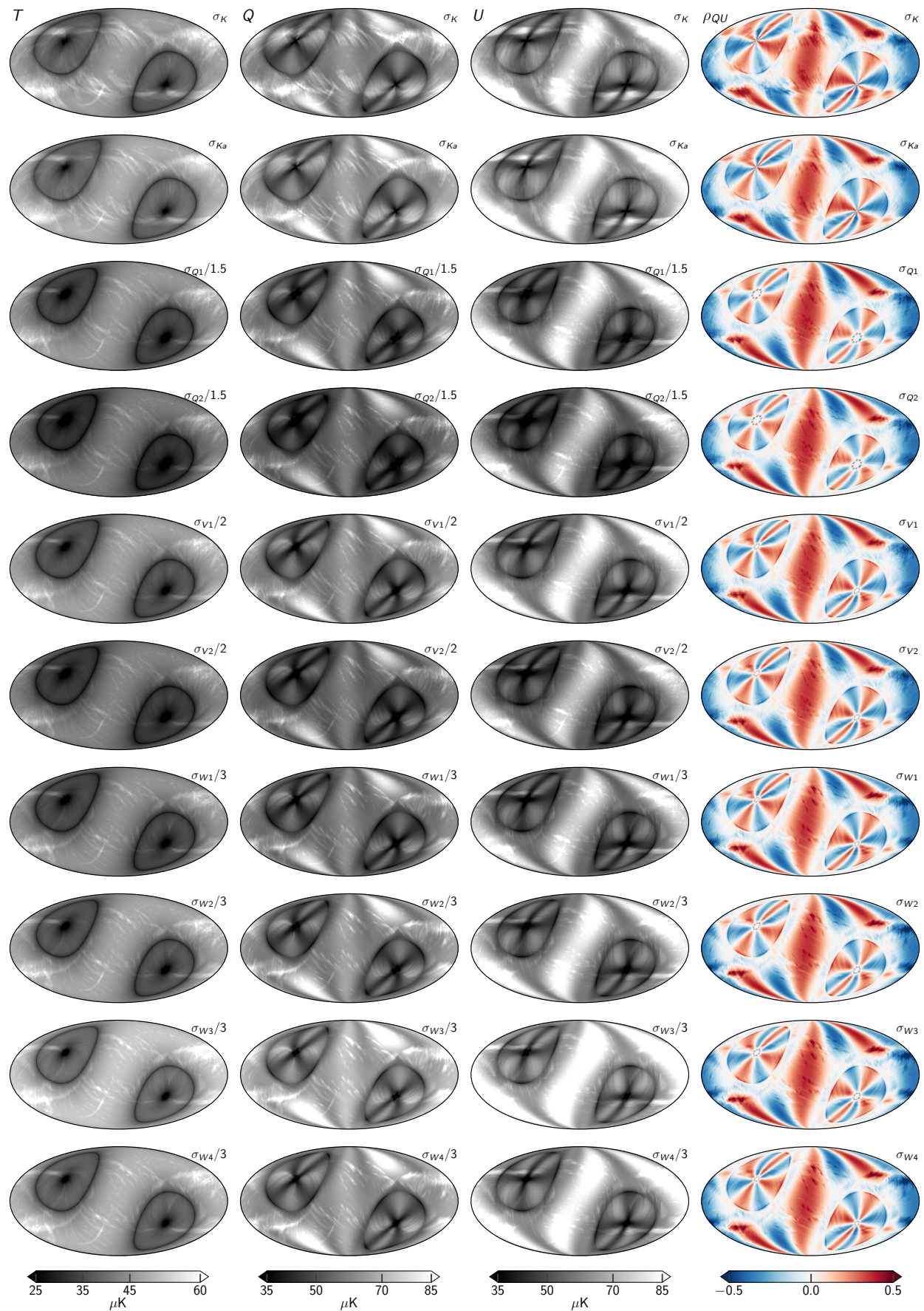
**Fig. A.6.** Fknee.

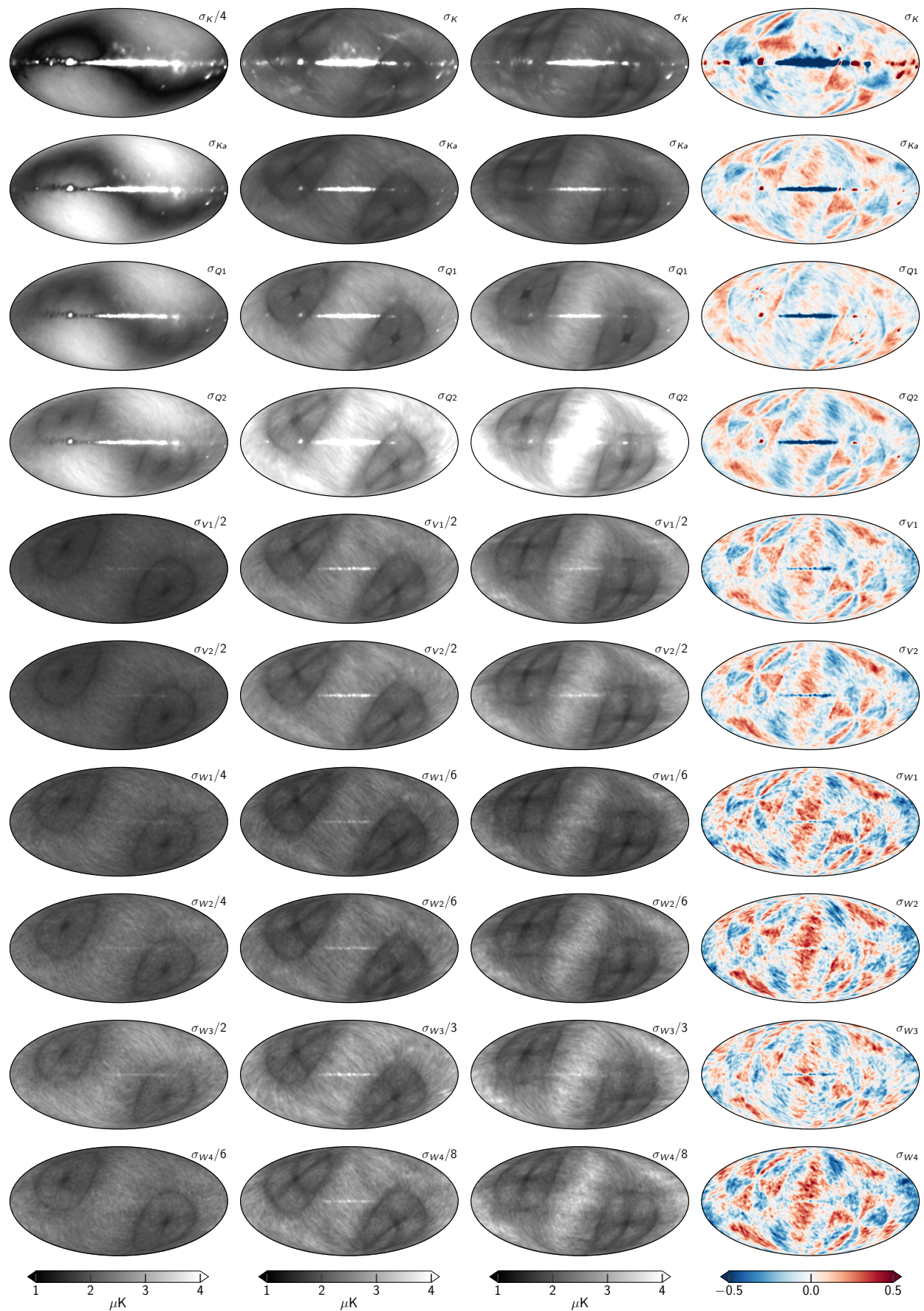
**Fig. A.7.**  $\alpha$ .

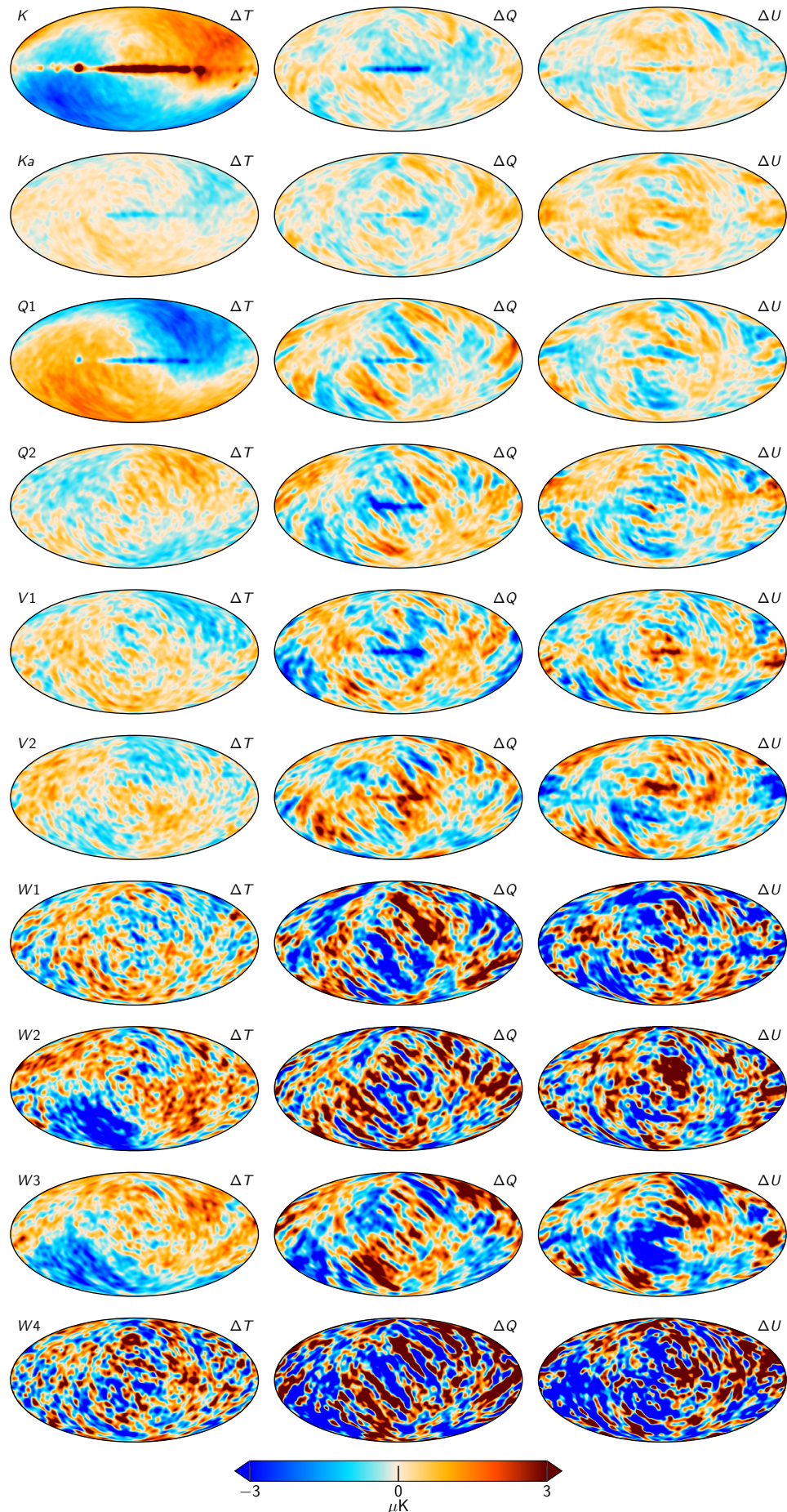
**Fig. A.8.** chisq.

**Fig. A.9.** Transmission imbalance templates

**Fig. B.1.** Sky maps

**Fig. B.2.** RMS maps

**Fig. B.3.** STD std

**Fig. B.4.** Differences between two samples

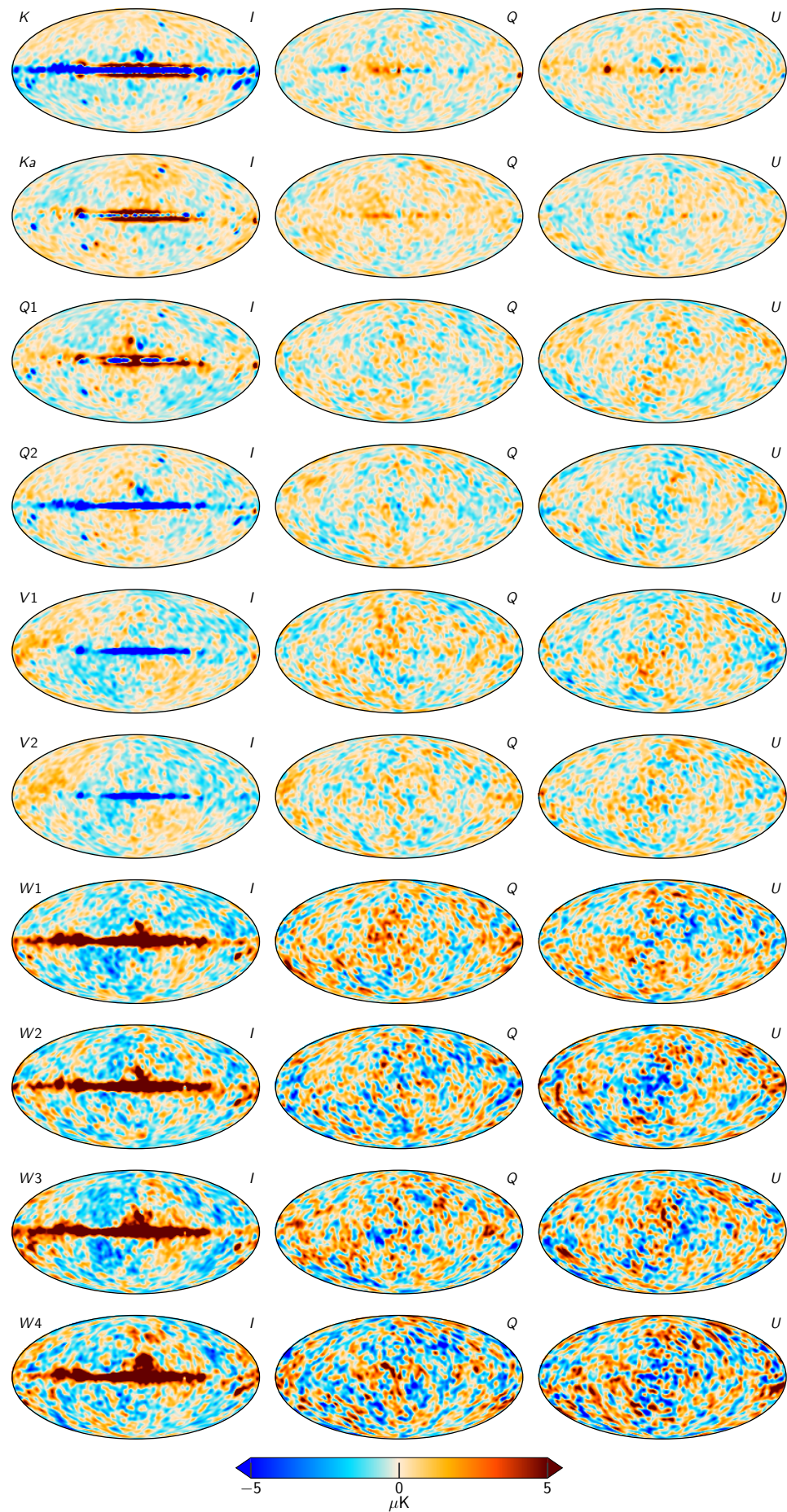


**Fig. B.5.** TOD Residuals for each of the WMAP channels, smoothed by  $5^\circ$ .  
Article number, page 52 of 53

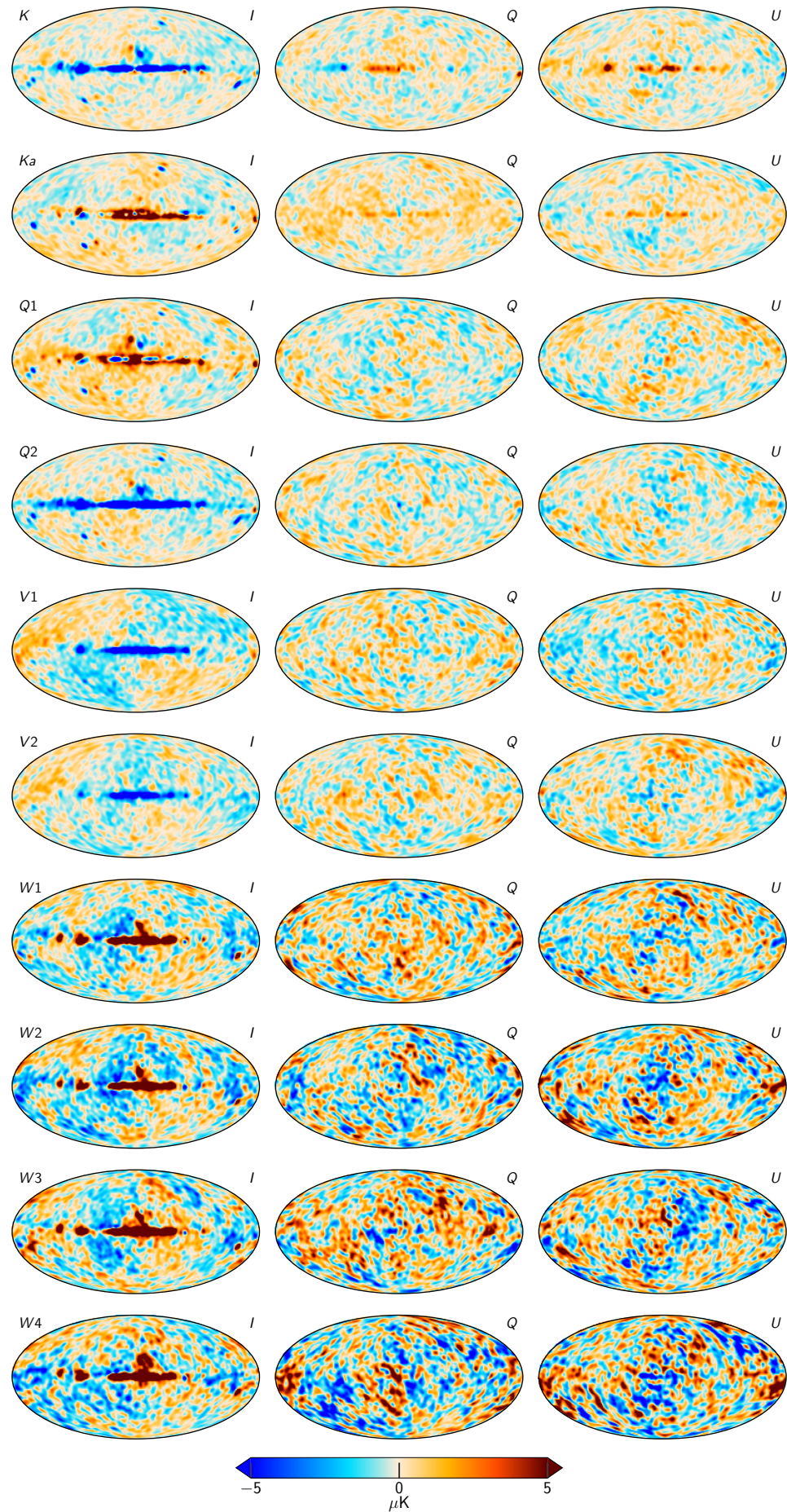


**Fig. B.6.** Component separation residuals for each of the WMAP channels, smoothed by  $5^\circ$ .